



Universitat Autònoma de Barcelona

ADVERTIMENT. L'accés als continguts d'aquesta tesi doctoral i la seva utilització ha de respectar els drets de la persona autora. Pot ser utilitzada per a consulta o estudi personal, així com en activitats o materials d'investigació i docència en els termes establerts a l'art. 32 del Text Refós de la Llei de Propietat Intel·lectual (RDL 1/1996). Per altres utilitzacions es requereix l'autorització prèvia i expressa de la persona autora. En qualsevol cas, en la utilització dels seus continguts caldrà indicar de forma clara el nom i cognoms de la persona autora i el títol de la tesi doctoral. No s'autoritza la seva reproducció o altres formes d'explotació efectuades amb finalitats de lucre ni la seva comunicació pública des d'un lloc aliè al servei TDX. Tampoc s'autoritza la presentació del seu contingut en una finestra o marc aliè a TDX (framing). Aquesta reserva de drets afecta tant als continguts de la tesi com als seus resums i índexs.

ADVERTENCIA. El acceso a los contenidos de esta tesis doctoral y su utilización debe respetar los derechos de la persona autora. Puede ser utilizada para consulta o estudio personal, así como en actividades o materiales de investigación y docencia en los términos establecidos en el art. 32 del Texto Refundido de la Ley de Propiedad Intelectual (RDL 1/1996). Para otros usos se requiere la autorización previa y expresa de la persona autora. En cualquier caso, en la utilización de sus contenidos se deberá indicar de forma clara el nombre y apellidos de la persona autora y el título de la tesis doctoral. No se autoriza su reproducción u otras formas de explotación efectuadas con fines lucrativos ni su comunicación pública desde un sitio ajeno al servicio TDR. Tampoco se autoriza la presentación de su contenido en una ventana o marco ajeno a TDR (framing). Esta reserva de derechos afecta tanto al contenido de la tesis como a sus resúmenes e índices.

WARNING. The access to the contents of this doctoral thesis and its use must respect the rights of the author. It can be used for reference or private study, as well as research and learning activities or materials in the terms established by the 32nd article of the Spanish Consolidated Copyright Act (RDL 1/1996). Express and previous authorization of the author is required for any other uses. In any case, when using its content, full name of the author and title of the thesis must be clearly indicated. Reproduction or other forms of for profit use or public communication from outside TDX service is not allowed. Presentation of its content in a window or frame external to TDX (framing) is not authorized either. These rights affect both the content of the thesis and its abstracts and indexes.

Computational schemes for defects energetics

Arsalan Akhtar

A Thesis submitted in fulfillment of the requirements
for the degree of Doctor of Philosophy in Material Science

Theory & Simulation Group
Catalan Institute of Nanoscience & Nanotechnology
Autonomous University of Barcelona

Supervisors

Dr. Pablo Ordejón

Institut Català de Nanociència i Nanotecnologia

Dr. Miguel Pruneda

Institut Català de Nanociència i Nanotecnologia

Tutor

Dr. Gemma Garcia Alonso

Autonomous University of Barcelona

2022

Supervisors

Dr. Pablo Ordejón

Institut Català de Nanociència i Nanotecnologia

Dr. Miguel Pruneda

Institut Català de Nanociència i Nanotecnologia

Abstract

Nothing is perfect! All crystalline structures have defects in them, even if their concentration might be small! These defects are responsible for different properties of materials and a good understanding of these requires to identify which defects are present, and in what concentrations for particular external conditions. Experimental access to this information is difficult, and computational materials simulations are a good complementary tool. In particular, first principles, or *ab initio* methods, that solve the quantum mechanical problem of the electronic structure of the system are at the forefront of the research on physical and chemical properties due to point defects, surfaces, grain boundaries, or heterostructures at the nanoscale. We have to take into account that modeling these defect structures is more demanding than simulations of pristine structures, because a larger number of particles in the simulation box are required. Furthermore, the amount of combinations of defects, structures, and configurations poses a tremendous challenge for these computational approaches. In recent years, the advent of *high-throughput computational (HTC)* schemes has triggered the development of automatized scripts that implement the complex workflows to attack this problem.

The objective of this *thesis*, is to advance on the computational study of defect properties from an *ab initio* perspective. We use the SIESTA package, a *Density Functional Theory (DFT)* code based on localized atomic orbitals, which has demonstrated to be a powerful tool to predict materials and their properties, specially when the number of atoms in the system is relatively large. In particular, we address three different problems which can be classified as (i) **Static Properties**, (ii) **Dynamic Properties**, and (iii) **Surface & Interface Properties**.

(i) Within **Static Properties**, I enhance and improve the approaches for calculating the defect formation energy, which can be linked to the probability of having a specific point defect under certain external conditions (temperature, chemical potentials, etc). I will discuss how charged point defects require special treatments when periodic boundary conditions are used in the simulations. I will present and validate a new approach for calculating the formation energy

of charged defects that leads to very good scaling convergence, and unlike other standardized approaches does not need any external parameters. The specific approaches required for the basis set in SIESTA calculations are also discussed, and general directives sketched.

(ii) Within **Dynamic Properties** we include the movements of defects, which is important for ionic conductivity in solids among many other processes (Li diffusion in batteries; electromigration; etc). Here, the energy barrier required for activation of the diffusion of the ions is the information that can be computed with DFT. I developed different flavors of the *nudged elastic band method (NEB)* to calculate the barrier within the *Born-Oppenheimer approximation*. Using SIESTA as an engine to run these computationally demanding *NEB* simulations, we could obtain the energy barriers in a matter of hours, not days, as in typical plane-wave codes. I developed all the required SIESTA machinery under a **Siesta Barriers Workflows** package for AiiDA, another powerful platform that enables high-throughput computational screening for all possible migration paths.

(iii) Finally, within the **Surface & Interface Properties** block, I took standard methodologies for generating the slabs and the know-how for defining SIESTA basis set for surfaces to develop a SIESTA workflow package (**siesta aiida surfaces**). Again having SIESTA engine behind it, the package reduces the computational cost with respect to expensive plane-waves approaches in the study and exploration of surfaces and heterointerfaces along different crystallographic orientations.

As an illustration of the combination of the different tools developed, we study the effect of vacancy defects at a HfO_2 /Graphene heterointerface, providing information that confirms experimental hypothesis for new hybrid nanostructures which are of interest for solar generation and storage of energy, and are based on the combination of carbon nanotubes with dielectric nanoparticles.

Acknowledgments

First and foremost, I would like to thank my dearest supervisors Prof. Pablo Ordejón and Prof. Miguel Pruneda, for allowing me the opportunity to have a Ph.D. journey in the first place. This journey was an incredible opportunity to learn a new way of thinking and redefine for me the one English word, "WHY?!", with a question and exclamation mark! I wish to express my appreciation to Miguel. He always remains patient with me despite my stubbornness and many missteps that I have made through these years. I will be forever indebted to him and Pablo.

Also, I want to give my gratitude to many friends and colleagues with that I had the opportunity to work, laugh and have discussions: Bogdan, Vladmir, Roberto, Ramón, Pol, Emanuele, Nils, Jose, Linda, Jiahui, He, Nick, Roberta, Federico, Ernane, Dilson, Zeila, Matthieu, Javier, Alberto, Pablo, Ainhoa, Clara, Bipen, Gopal, Namrita, Xavi, Mehdi, Mohammad, Fariba, Batoul, Moji, Azra, Javad.

I want to thank Pol, Emanuele, and Alberto immensely for all of their guidance for Sisl and AiiDA for this work. I also thank Nick for his exceptional inputs in sisl and flos.

Lastly, I want to thank my Family, Emtiaz, Zahra, Hadiyah, Atiyeh, who have always supported me in all my decisions and endeavors.

Contents

Abstract	iii
Acknowledgments	v
Contents	vii
I The Beginning of It All	1
1 Introduction & Motivation	3
1.1 Materials in Nature: Defects & Surfaces	3
1.2 Defects & electronic properties	6
1.3 Computational Material Science	9
1.3.1 The High-Throughput Computations Era!	9
1.3.2 Tools Available	10
1.4 Our case study systems: defects in Oxides	11
1.4.1 Magnesium Oxide MgO	11
1.4.2 Hafnium(IV) Oxide HfO ₂	12
1.5 Thesis Outline	12
2 Theoretical Background	15
2.1 Materials	15
2.2 Material Simulations	15
2.2.1 Fundamental Steps in the modeling	15
2.3 Ab-initio methods for Electronic Structure Calculations	17
2.3.1 The Adiabatic and Born-Oppenheimer Approximations	17
2.3.2 Density Functional Theory : The Hohenberg-Kohn Theorems	18
2.3.3 Density Functional Theory: Orbital-Free	20
2.3.4 Density Functional Theory: Kohn-Sham Theory	21
2.3.5 On Exchange–Correlation Functionals	22

2.3.6	Self-Consistency Field (SCF) Method	22
2.4	The SIESTA Method	24
2.4.1	Materials Properties	25
II	Defects Energies	29
3	Defects Formation Energies Methods	31
3.1	Defects	31
3.1.1	Point Defects Catalogue	33
3.2	Defects Formation	39
3.2.1	Calculating defect formation energies under Periodic Boundary Conditions (PBC)	42
3.2.2	Neutral Defect Formation	45
3.2.3	Charged Defect Formation	45
3.2.4	Finite-Size Corrections	48
3.2.5	Long Range Interactions in PBC & Finite-Size Corrections Terms for Charged Systems	48
3.2.6	Charge Defect Formation Phase Stability Diagram	59
3.3	Implementation of Sisl ToolBox Siesta Defects and AiiDA Siesta Defects	61
4	Defects Formation Energies: Applications	63
4.1	Defects and Charged Defects in Materials	63
4.1.1	Importance of <i>Ghost</i> (or floating) orbitals	64
4.2	Charged Defects: The case where the charge is <i>well-behaved</i> (localized & spherical)	73
4.2.1	Positively Charged Oxygen Vacancies ($V_O^\bullet, V_O^{\bullet\bullet}$) in MgO	73
4.2.2	The Gaussian Model (q_{model}) vs. The ρ correction scheme	74
4.3	Charged Defects: When things go wrong.	75
4.3.1	Carbon Vacancies in Diamond Structure	76
4.3.2	Negatively Charged Ga Vacancy ($V'_{Ga}, V''_{Ga}, V'''_{Ga}$) in GaAs	80
4.3.3	Oxygen Vacancies ($V_O, V_O^\bullet, V_O^{\bullet\bullet}$) in HfO_2	83
4.3.4	Comments on negatively charged oxygen vacancies	86
4.4	Charged Defect Formation Stability Diagram	88
4.5	Computational Details	89
4.6	Conclusions	90

III	Defects Barriers	91
5	Potential Energy Surface (PES) Methods	93
5.1	Introduction	93
5.2	Transition States	93
5.3	Methods for Calculating <i>TS</i>	95
5.3.1	Nudged Elastic Band (NEB)	95
5.3.2	Climbing Image Nudged Elastic Band	97
5.3.3	Doubly Climbing Image Nudged Elastic Band	98
5.3.4	Variable Cell Climbing Image Nudged Elastic Band	99
5.4	Image Generations	101
5.4.1	Linear Interpolation Method	101
5.4.2	Image Dependent Pair Potential Method	101
5.5	Defects Diffusion & Barriers	102
5.5.1	Defects Diffusion Types	102
5.6	Implementation of Sisl ToolBox Siesta Barriers and AiiDA Siesta Barriers	105
6	Siesta Barriers Applications	107
6.1	Vacancy Exchange & Importance of ghosts species	108
6.2	Comments on localized charge correction and <i>BSSE</i>	114
6.3	Computational Details	116
6.4	Conclusions	117
IV	Surfaces & Interfaces	119
7	Methods for Surfaces & Interfaces	121
7.1	Surfaces	121
7.1.1	Types of Surfaces	121
7.1.2	Surface Energy	123
7.1.3	The Workfunction	124
7.2	Surfaces Electrostatics	124
7.2.1	Issue (i): Isolated Boundary Conditions	125
7.2.2	Issue (ii): Periodic Boundary Conditions	126
7.3	Heterostructures	127

7.4	Implementation of Sisl ToolBox Siesta Surfaces and AiiDA Siesta Surfaces	128
7.4.1	The problem of localized basis set	129
8	Siesta Surfaces Applications	131
8.1	(100),(110),(111) surfaces in cubic HfO_2	132
8.2	Oxygen Vacancy in $\text{HfO}_2(111)$	133
8.3	Graphene on cubic $\text{HfO}_2(111)$ surface	135
8.4	Computational Details	140
8.5	Conclusions	140
9	Conclusions & Outlook	143
V	Appendix	147
A	LUA & Scripts	149
A.1	Introduction	149
A.1.1	LUA	149
A.2	Fortran LUA Hook (FLOOK) Library	150
A.2.1	Concepts & Implementations	150
A.3	Flook SIESTA (FLOS) Library	155
	Bibliography	161
	List of Publications	175

List of Figures

1.1	Ruby gem is crystalline Al_2O_3 that is red due to the presence of chromium impurities (The Figure is taken from Wikipedia). . . .	3
1.2	Lowering the critical temperature (T_c) of $(\text{La},\text{Sr},\text{Ca})_3\text{CuO}_{6+x}$ as a function of the number of interstitial oxygen defects between the CuO_2 layers, $n(\text{O}_3)$. Figure is taken from [Jor+94].	4
1.3	Creating a vacancy atom leaves dangling bonds in surrounding atoms (the dangling bond shown with cloud around neighbouring atoms and vacancy position is shown with \times). Creating impurities creates shallow donors (acceptors) hydrogenic levels.	7
1.4	Localized electron states of point defects impurities in metal oxides: M_i =interstitial metal, V_M = metal ion vacancy, V_O = oxide ion vacancy, A = Acceptor impurity, D =Donor impurity.	8
2.1	The mathematical framework for Four Domains of Dynamical Equations	16
2.2	self-consistent solution flow-chart for Kohn-Sham equations . .	23
3.1	Dimensional hierarchy of defects in crystals (a) $0D$ defects known as point defects (b) $1D$ defects known as linear defects, dislocation is an example of it (c) $2D$ defects known as planar defects and (d) $3D$ defects such as clusters of point defects, voids and precipitates	32
3.2	The diagram of point defect categorization	33
3.3	Type of Defects in Monoatomic crystal	35
3.4	Type of Defects in Monoatomic crystal	35
3.5	Type of Defects in Compound crystal	36

3.6	Illustration of the <i>Kröger-Vink</i> notation for Oxygen vacancies in MgO. Mg and O atoms are represented as blue and green spheres respectively. (a) neutral O atoms is removed from the lattice, leaving two electrons at the vacancy site. The surrounding Mg^{+2} charges compensate the vacancy charge, resulting in a neutral effective charge. (b) The oxygen anion (with the two electrons on the O) is removed. This leaves a positive effective charge due to the local environment around the vacancy	38
3.7	Change in Gibbs energy, ΔG , of a crystal as function of the number of point defect present. (Figure is taken from [Til08]). .	40
3.8	(a) Pristine vibrational entropy (b) defected vibrational entropy (c) Configurational entropy $S_1^{\text{Configurational}}$ (d) Configurational entropy $S_2^{\text{Configurational}}$. Since it was ordered, the (d) system has smaller configurational entropy than system (c) ($S_1^{\text{Configurational}} > S_2^{\text{Configurational}}$). (The figure is adapted from [SL20])	41
3.9	Neutral and Charge Defect in PBC (a) Total Neutral charge in PBC where $\rho_{\text{elec}}(\mathbf{r})$ and $\rho_{\text{ionic}}(\mathbf{r})$ cancel out each other in a cell. (b) The charged system where the net charge is shown in the cloud distribution and neutralizing uniform charge jellium $\langle n \rangle$ is shown as blue background in the cell.	43
3.10	The scaling rule for Finite-Size Corrections. The fading red circle represents the interaction on the N scaled system. Increasing the cell (N) will reduce this interaction and essentially be zero in E_∞	47

3.11	Illustration of the approach to converge the calculations for defects by increasing the simulation box. Top panel illustrates a localized defect charge within the box. Central panel is the actual supercell, which contains $N \times N \times N$ repetitions of the crystal unit cell and the point defect that gives the localized defect level. The scaling rule for charge defects convergence (lower panel) usually requires supercells with a large number of atoms, becoming prohibitively expensive computationally. For instance, crystals with a unit cell ($1 \times 1 \times 1$) containing eight atoms will become computationally challenging if the supercell required for converged defect energies becomes ($4 \times 4 \times 4$), which has a total of 512 atoms!. These cell sizes are not uncommon to have well converged results even with the best correction schemes available.	49
3.12	The Comparison of defect charges before and after screening for the V_c'' in diamond in a 64-atom supercell. The defect is located at $z = 0$ with a periodic image at $z = 13.3$ bohr. The limit of a homogeneously distributed screening charge is indicated by the black dash-dotted line. (Figure is taken from [FNV11]).	52
3.13	The long and short-range Coulomb potential profile where short-range fall very fast to zero with respect to the long-range. (Figure is taken and modified from [Hua+10]).	53
3.14	The schematic diagram for charge defect Model potential defect-defect interactions in PBC , q^{model} is the charge model for representing the localized defect charge, $V(r)$ is DFT potential, and V^{lr} represents the long-range interactions with periodic defect image after the screening of material. (Figure is taken and modified from [FNV11]).	54
3.15	The Alignment approach in the KO correction method where average $V_{NAP,q/p}$ is taken at the atomic positions in the region outside of the sphere that is in contact with the Wigner-Seiz cell with radius R_{WS} . [Adapted from “Electrostatics-based finite-size corrections for first-principles point defect calculations,” by Yu Kumagai et al. [KO14]]	55
3.16	The V_O^\bullet defect charge in MgO calculated from DFT as in Eq 3.35. The Mg and O ions denoted by blue and red dots, respectively. The black dot show the position of the oxygen vacancy.	56

3.17	The alignment approach in the DCCP correction method has four components. Each sketch in the figure denotes a <i>DFT</i> single calculation. A is the host material without any defects. D corresponds to the relaxed structure of a charged defect introduced in the host crystal. This charged defect can be a vacancy, impurity, or interstitial with a corresponding charge state. Two intermediate steps can be defined: In B, the same defect in its neutral state (no extra charges in the box) is introduced in the pristine system without any ionic relaxation. Similarly, C is also a neutral system but this time taking the relaxed geometry of D (also called <i>neutralized defect</i> . [Adapted from “Relation between image charge and potential alignment corrections for charged defects in periodic boundary conditions,” by T.R.Durrant et al. [Dur+18]]	58
3.19	The point defects formation vs. Electron chemical potential known as charged defect stability diagram. A positive slope corresponds to a positively charged defect, while a negative slope corresponds to a negatively charged defect configuration. Neutral defects are independent on the electronic chemical potential. Depending on what is the position of the Fermi level, different charge states for the defect can be stabilized. In the figure, a Fermi level close to the conduction band will stabilize negatively charge defects, while Fermi levels close to the valence band stabilize positively charged defects. The crossings between curves with different slopes are linked to the position of a defect level that can populated/depopulated.	60
3.20	Schematic diagram of different terms in formation energy of charged defects. $E_{tot}[X^q]$ is the <i>DFT</i> energy of the supercell containing a defect of X with a charge state of q , $E_{tot}[pristine]$ is the <i>DFT</i> energy of the pristine supercell, $\sum_i n_i \mu_i$ is the energy cost of introducing n_i species with chemical potential μ_i and can be used to take into account the chemical environment and the growth conditions, $q\mu_e$ is the electronic potential for the electron reservoir, the E_{corr}^q accounts for spurious localized charge defect interactions with <i>PBC</i> and finally $q\Delta V_{NAP}$ aligns the potential to have the same references for pristine and defective system. .	62

- 4.1 DFT calculated Defect charge distribution ρ_{defect} from difference of $\rho_q - \rho_{nd}$ as in Eq 3.35 for (a) V_O^\bullet in MgO the Mg and O ions denoted by blue and red dots, respectively and (b) V_{Ga}''' in GaAs, the Ga and As ions denoted by orange and gray dots, respectively. The black dots show the position of the respective vacancies in both cases. 63
- 4.2 The Spin polarised electronic band structure of Oxygen neutral and positively charge defects in MgO along a high symmetry path in the Brillouin Zone. The Fermi energy is shifted to zero for all bands; this is due to taking the reference of it from the valence band maximum of the pristine as we discussed in chapter 3. (a) The pristine MgO with a clear gap of ≈ 5 eV (experimental = 7.8 eV). (b) The V_O in MgO with a doubly generated state in the gap, which is populated by two electrons. (c) The V_O^\bullet in MgO with only one spin state populated (d) The $V_O^{\bullet\bullet}$ in MgO with completely depopulated state in the gap. 65
- 4.3 Contour plots with the charge redistribution around the neutral oxygen vacancy (V_O). Left panel shows $\rho_{pristine} - \rho_{defect}$ with *ghost* orbital in the basis and the unrelaxed structure. Central panel plots the difference between the densities obtained with *ghost* and without *ghost*, in the unrelaxed structure. Right panel is equivalent to central panel, but for the relaxed geometry obtained with the *ghost*. The Mg and O atoms positions are shown as blue and red circles, and the black dot corresponds to the position of the vacancy. Bottom panel shows an isosurface corresponding to a density of $0.005 \text{ e}/\text{\AA}^3$ 67
- 4.4 Electronic charge distribution after relaxation for different charge states (a) $V_O^{\bullet\bullet}$ (b) V_O^\bullet . Left panel shows results obtained with *ghost* orbitals, while right panels correspond to calculations run without *ghost*. Notice the hollow region (light grey) in the system without *ghost*. The charge density is defined as in Eq 3.35 (difference between the charged and the *neutralized* defect calculations) and plotted over the (100) plane that contains the vacancy site. Blue and red dots correspond respectively to the Mg and O atoms surrounding the oxygen vacancy. 68

4.5	Projected Density of States around the electronic gap showing the defect level due to V_O . Panels (a) and (b) correspond to the Ground State defect configuration. The valence and conduction bands are shown as striped grey areas, and the energy is aligned to the top of the valence band. Dashed horizontal lines are guidelines to the defect level position. The projection on bulk Mg and O orbitals (far from the defect) are black and dark grey shaded areas, respectively. Black thick line corresponds to oxygen atoms that are close to the defect (O_{nn}), while red line is used for Mg next neighbors to V_O . The projection onto the <i>ghost</i> orbitals is plotted as shaded cyan regions in panels (b).	70
4.6	The formation energy vs $1/L$ for oxygen vacancy (V_O) in $q = +1, +2$ states, using ρ_{defect} as in Eq 3.35. Dashed lines correspond to uncorrected data, while solid lines are the corrected energies. The dielectric constants used to compute the electrostatic energy are ϵ_0 for the <i>relaxed</i> structure (panel a), and ϵ_∞ for the <i>unrelaxed</i> structure (panel b).	73
4.7	Results obtained for the formation energies of oxygen vacancy (V_O) in $q = +1, +2$ using a Gaussian charge model. (a) dependence with supercell size L ; (b) and (c) show the dependence of the formation energies with the width of the Gaussian (σ) for the +1 and +2 charge states computed with a $2 \times 2 \times 2$ supercell. The value obtained with the DFT charge is shown with the red square for reference.	74
4.8	The carbon vacancy charge distribution ρ_{defect} as in Eq 3.35 for charge state $q = -4e$ in diamond structure shown from (100) lattice plane. Blue dots correspond to the C positions surrounding the vacancy, which is represented by the black dot. The left panel represents contour plots of the charge distribution, while the right panel plots a 3D isosurface corresponding to density of $0.1 \text{ e}/\text{\AA}^3$.	76

4.9	Spin polarised electronic band structure for carbon vacancy in Diamond along the high symmetry path in the Brillouin Zone, for different charge configurations. Bands for spin up and down are plotted as blue and red lines. The Fermi level is placed at 0 eV. (a) bands for the pristine system. (b) neutral vacancy, with two electrons populating the up spin triplet state. (c) an additional electron fills the triplet band with spin up. (d) to (f) correspond to adding additional electrons that populate the down spin triplet bands.	78
4.10	Spin polarised electronic band structure for positively charged carbon vacancy in Diamond. Bands for spin up and down are plotted as blue and red lines. The Fermi level is placed at 0 eV. (a) Positively charged V_C^\bullet , where only one electron populates the up spin triplet state. (b) $V_C^{\bullet\bullet}$ defect, where no electrons are placed at the triplet state.	79
4.11	The Formation Energies of V_C in different supercell of diamond vs. $1/L$ using ρ_{defect} as in Eq 3.35 for correction scheme with static dielectric $\epsilon_0 = 5.76$	79
4.12	Spin polarised electronic band structure of pristine (a) and V_{Ga} in GaAs along a typical high symmetry path in the Brillouin Zone. Different electrons are added to the system to populate the triplet defect state, from zero (neutral defect) to $-3e$ (V_{Ga}'''), panels b to e. The Fermi energy is shifted to Zero for all bands.	80
4.13	Band structure of V_{Ga}''' defect in GaAs using different supercells: (a) $2 \times 2 \times 2$; (b) $3 \times 3 \times 3$; (c) $4 \times 4 \times 4$; and (d) $5 \times 5 \times 5$. The dispersion of the triplet state reduces with the size of the cell.	81
4.14	The formation energy of $q = -1e, -2e, -3e$ charged gallium vacancy (V_{Ga}) as a function of the size of the supercell. The correction scheme (solid lines) uses ρ_{defect} as in Eq 3.35 and $\epsilon_0 = 12.9$ for <i>relaxed</i> and $\epsilon_\infty = 10.89$ for <i>unrelaxed</i> structures. The dashed lines correspond to the uncorrected energies.	82

4.15	Oxygen vacancy charge distribution ρ_{defect} as in Eq 3.35 shown from (011) lattice plan for charge state in $q = +1, +2$ in cubic HfO_2 structure. Green and red dots denote the Hf and O atoms surrounding the oxygen vacancy, respectively. The left panel represents 2D contour plots of the charge distribution, while the right panel plots a 3D isosurface corresponding to density of $0.015 \text{ e}/\text{\AA}^3$ and $0.005 \text{ e}/\text{\AA}^3$ for V_{O}^{\bullet} and $V_{\text{O}}^{\bullet\bullet}$ respectively.	84
4.16	Spin polarised electronic band structure of pristine (a), neutral (b) and positively charged (c-d) oxygen vacancy defect in HfO_2 along the high symmetry path in the Brillouin Zone. The Fermi energy is shifted to Zero for all bands. (a) Pristine system with a clear band gap (b) A defect state in the gap, which is partially filled with 2 electrons (c) The defect states in the gap, which is partially filled with 1 electrons. (d) Completely depopulated defect state falls in the conduction band and is not visible in the gap.	85
4.17	<i>Relaxed</i> structure obtained for “cubic HfO_2 with V_{O}' and V_{O}^{\bullet} defect. (a) The relaxation of V_{O}' defect induces a global structural distortion, and the final structure corresponds to the tetragonal phase of HfO_2 . (b) The relaxation of V_{O}^{\bullet} defect induces a local distortion, but the cubic phase remains far from the defect. . . .	86
4.18	Oxygen vacancy defect charge distribution ρ_{defect} as in Eq 3.35 shown from (011) lattice plan for $q = -1e, -2e$ in cubic HfO_2 structure (a) delocalized charge (b) delocalized charge with longer tail. Green and red dots denote the Hf and O atoms surrounding the oxygen vacancy, respectively. The left panel represents 2D contour plots of the charge distribution, while the right panel plots a 3D isosurface corresponding to density of $0.02 \text{ e}/\text{\AA}^3$ for both V_{O}' and V_{O}''	87
4.19	The Phase Diagram of MgO, Diamond, GaAs, HfO_2 , (a) For Cubic MgO the oxygen vacancies (V_{O}^{qe}) in $q_e = 0, +1, +2$ charge states phase diagram (b) Cubic Diamond V_{C} defect formation phase diagram (c) Cubic GaAs V_{Ga} defect formation stability diagram (d) Cubic HfO_2 oxygen vacancy (V_{O}) defect formation stability diagram	88

5.1	Different geometrical configurations (images) energies along the reaction path with the highest energy geometrical configuration known as <i>transition states</i>	93
5.2	Geometrical configuration of the different interstitial sites energies along the reaction path for a BCC crystal [adapted from Defects in Solids by Richard.J.D. Tilley, Wiley 2008 [Til08]] . . .	94
5.3	The geometrical configuration of the different image energies from reactant to product goes through a saddle point in <i>MEP</i> . . .	96
5.4	The Components of Forces in <i>PES</i> [Figure is taken from Optimization methods for finding minimum energy paths [STH08] ©	98
5.5	(a) DNEB different force components to keep band straight. the (b) is force on image perpendicular to the band [Figure is taken from Optimization methods for finding minimum energy paths [STH08] ©	99
5.6	vacancy & interstitial Diffusion scheme	102
5.7	kick-in/out scheme	103
5.8	exchange & vacancy exchange scheme	104
5.9	ring or <i>n</i> -exchange scheme	104
5.10	Structural Transition scheme	105
6.1	Scheme for the migration of a vacancy from the initial configuration (a) to the final (c). The Transition State (TS) is equivalent to an interstitial atom and two vacant sites placed at the initial and final positions.)	107
6.2	Possible approach of vacancy exchange barrier calculation (reds oxygen and gray <i>ghost</i> species)	109
6.3	<i>NEB</i> migration barriers for V_O using different basis set descriptions. Red filled (empty) circles correspond to type <i>i</i> (<i>ii</i>); empty blue squares to type <i>iii</i> basis, and filled blue squares to <i>iv</i> . The energy of the initial state for the <i>iv</i> is taken as the origin. Calculations without any ghost orbitals are also included for comparison.	111

6.4	Projected Density of States around the electronic gap showing the defect level due to V_O . Panels (a)-(c) correspond to the Transition State geometry obtained with the <i>NEB</i> method. The valence and conduction bands are shown as striped grey areas, and the energy is aligned to the top of the valence band. Dashed horizontal lines are guidelines to the defect level position (the position of the Fermi level would depend on the whether the defect state is populated or depopulated). The projection on bulk Mg and O orbitals (far from the defect) are black and dark grey shaded areas, respectively. Black thick line corresponds to oxygen atoms that are close to the defect (O_{nn}), while red line is used for Mg next neighbors to V_O . The projection onto the <i>ghost</i> orbitals is plotted as shaded cyan regions in panels (a)-(c) to facilitate visualization. Panel (c) has two <i>ghost</i> orbitals placed in the initial and final positions for the migrating oxygen, but only the projection over one of them is plotted (both give similar contribution). For the Transition State panels, the PDOS for the migrating oxygen atom (which resembles an interstitial oxygen, O_i) is plotted as shaded blue also on the left subpanel.	113
6.5	Scheme of the <i>BSSE</i> correction we consider for <i>NEB</i> barriers. The V_O and O species are represented by gray and red colors, respectively. The shadows with a gradient represent the basis of each species. (a) two <i>ghost</i> orbitals are included at the initial and final positions of the migration. At the transition state the moving oxygen is placed in-between the ghosts. (b) For calculating the <i>BSSE</i> the energy of the initial image is recomputed with an additional <i>ghost</i> orbital placed at the position that the moving oxygen occupies at TS.	115
6.6	V_O Migration Path in $\langle 110 110 \rangle$ MgO FCC Structure	116
7.1	The Type-I Non-Polar termination of the surface	122
7.2	Type-II Non-Polar termination of the surface	123
7.3	The Type-III Polar termination of the surface	123
7.4	Schematic illustration of the planar-averaged potential $\bar{V}(z)$ for an isolated slab with a dipole moment m perpendicular to the surface. (Figure is taken from [MV01b]).	125

7.5	Schematic illustration of the planar-averaged potential $\bar{V}(z)$ for repeated slab with a dipole moment m perpendicular to the surface. (Figure is taken from [MV01b]).	126
7.6	Schematic view of different Heterostructure. (Figure is adapted from [Das+18]).	128
7.7	Schematic view of different schemes for basis sets for the surface	129
8.1	classifying the low-index surfaces of cubic HfO_2	132
8.2	Surface Formation Energy of all low-index surfaces of cubic HfO_2 . The solid and dashed lines correspond to relaxed and unrelaxed structures.	133
8.3	The Band Structure of $\text{HfO}_2(111)$ with neutral oxygen vacancy in center and surface of the slab	134
8.4	The $p\text{DOS}$ of $\text{HfO}_2(111)$ with neutral oxygen vacancy in center and surface of the slab	135
8.5	The Structure of $\text{HfO}_2/\text{Graphene}$ from (a) side and (b) top view. The vacancy position is either on the surface of HfO_2 or in the center where the region is bulk-like. The carbon vacancy is located on top of oxygen, where we created the vacancy in the surface of HfO_2	136
8.6	The <i>fatBands</i> of hybrid $\text{HfO}_2(111)/\text{Graphene}$ heterostructures with different types of vacancies. The weights on the different chemical species on the character of each electronic state (band) is plotted with a color code, highlighting that graphenes bands (dark grey) are clearly distinguishable from HfO_2 's valence band (mostly Oxygen bands in red) and the conduction band (with more weight on Hfs $3d$ orbitals).	139
A.1	FLOOK Library Scheme can create main points in the Fortran program to communicate with particular variables.	151
A.2	FLOS Lib contains different schemes & functionality for SIESTA such as a new optimizer, nudged elastic band, grid convergence test algorithm etc.	156
A.3	Flos Library contains four main Class: i) Molecular Dynamic (MD) class, ii) Numerical (Num) Class, iii) Optimizer (Optima) Class and iv) Special Class	158

List of Tables

3.1	Kröger-Vink Notation for Defects in Crystals	37
4.1	Structural properties around the vacancy in different charge states, with <i>ghost</i> and without <i>ghost</i> in the orbital basis set. The interatomic distances between Mg atoms first-neighbors to V_O , and the next Mg-O bonds are shown. The percentage shows the variation with respect to the distances in the pristine system. . .	69
4.2	Calculated formation energies for the different charge states . .	71
4.3	The DFT exchange-correlation functional, basis sets, k -points, and the mesh cutoff that we used for each system	89
6.1	Calculated energy barriers (in eV) using different basis set representations and for different defect charge states. Note that two barriers are reported for case (i), which correspond to <i>forward</i> and <i>backward</i> migrations in the asymmetric path shown in figure 6.3. Ref. [MD11] uses VASP (PW) and PW91 xc-functional while Ref. [El-+18] uses CP2K (Gaussian + plane-waves) and PBE functional.	112
6.2	The Correction on calculated energy barriers (in eV) for different defect charge states using Two <i>ghost</i> basis system	115
8.1	Binding energy per carbon atom for (i) the oxygen defects on the center of the slab, (ii) the oxygen defects on the surface of the slab, (iii) the carbon defect in graphene and (iv) the oxygen defects on the surface of the slab and carbon defect in graphene.	137
A.1	Available variables for SIESTA and it corresponding dictionary name.	159

Nomenclature

ϵ_F	Fermi Energy
ϵ_{vbm}	Valence Band Maximum
$\langle n_0 \rangle$	Jellium
\mathbb{F}	Field
\mathbb{P}	Property
\mathbb{R}	Response
\mathbf{H}_e	Hamiltonian
\mathcal{G}	Gibbs Energy
\mathcal{H}	Enthalpy
\mathcal{S}	Entropy
μ_e	Electrochemical Potential of electrons
Ω	Crystal Cell Volume
$\phi_{lmn}(r)$	Numerical Pseudo-Atomic Orbitals (NAO or PAO)
$\Psi_{tot}(\mathbf{r}, \mathbf{R}, t)$	Wave function
ρ	Electron Density
$F(N)$	Scaling Function
$H^f[X^q]$	Charged Defect Formation
q_e	Effective Charge

Part I

The Beginning of It All

1.1 Materials in Nature: Defects & Surfaces



Figure 1.1: Ruby gem is crystalline Al_2O_3 that is red due to the presence of chromium impurities (The Figure is taken from Wikipedia).

Usually, in condensed matter or solid-state physics, crystals are taken as perfect, infinite repetitions of a single unit cell; nonetheless, this is far from reality. These perfect crystals exist solely in theory. In reality, crystalline materials come with defects in them! Furthermore, these defects are often responsible for physical properties that are quite different from the ones corresponding to perfect or defect-free structures. Defects can modify a range of properties of materials including optical, magnetic, and electronic. For instance, a Ruby is Al_2O_3 crystal with Cr impurities, which modify, the colorless pure material to a precious intense red color (Figure 1.1). Thus, these impurities, which are a particular type of defects in the perfect crystalline lattice change the color of the material, which is one of the many optical properties that can be modified. They can also change the electrical characteristics. For example, creating interstitial oxygen defects in $(\text{La,Sr,Ca})_3\text{CuO}_{6+x}$ with x between 0.08 and 0.12 can transform this insulating ceramic to metal and then superconductor. In the superconducting phase, the

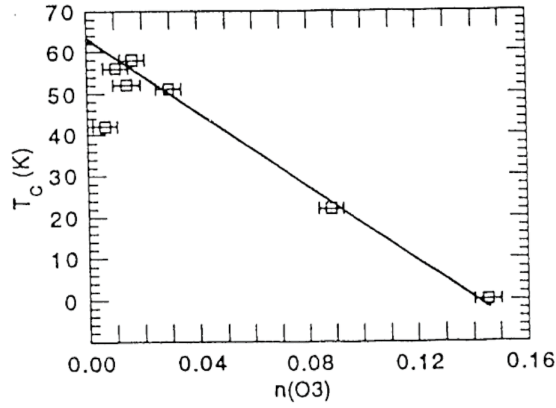


Figure 1.2: Lowering the critical temperature (T_c) of $(La,Sr,Ca)_3CuO_{6+x}$ as a function of the number of interstitial oxygen defects between the CuO_2 layers, $n(O_3)$. Figure is taken from [Jor+94].

critical temperature T_c continuously increases with decreasing concentration of oxygen defects inbetween the CuO_2 layers, $n(O_3)$, until it reaches 44 K, as shown in Figure 1.2 [Jor+94].

Addition of impurities in the host material in a controlled way is thus a powerful route to tune its electronic properties, which is sometimes called *defect engineering*. This is indeed an essential ingredient of modern technology, where doped semiconductors are the cornerstone of electronic components in devices. Because defects influence different properties of a material, many technologies take advantage of it. For instance, photocurrent generation can be enhanced in solar cell technology by introducing defect states. Magnetic impurities can be introduced in semiconductors to create new diluted semiconducting materials, defects can be used to reinforce the structural strength of materials for nuclear applications, they have been proposed as stable qubit candidates for quantum technologies, they are essential for enhancing the ionic mobilities in ceramic materials used for energy storage applications, etc. However, it is not only important to control how defects can be introduced in a material, but also identify which type of defects exist in order to relate the observed properties to the specific nature of the structure at the atomic level. Often, uncontrolled defects are present in the system, or certain defects can be detrimental to the

desired properties of the compound and mitigation strategies have to be used. For instance, the short lifetime of charge carriers is one of the limiting factors that have to be optimized for achieving high-efficiency solar cells. The creation of a deep-level due to antisite defect of Te, (Te_{Cd}) in CdTe solar cells has been identified as the dominant reason for low efficiency, thus these defects should be avoided [Ma+13; Yan+16].

Solely using experimental techniques to identify defects is challenging. Although there are techniques to characterize defects in bulk, their sensitivity depends on the defect concentration: for diluted defects measurements are difficult, and for large concentration, the nature of the defects can be substantially affected due to aggregation with other defects, or strong modification in the host material. Fortunately, theoretical modeling and simulations can be used to help. Theoretical tools allow to understand the properties due to different defects, for example something as critical as the probability of having a certain concentration of defects in a particular material depending on the synthesis conditions used. The aim of this *Thesis* is to develop different computational tools to calculate properties of *non-perfect solids*, systems where the translational symmetry of the crystal is broken, either because there are defects, or because the system is not infinite, and has surfaces or edges.

From the diverse classes of imperfections in the crystal, we will focus on the simplest, which are called *point defects*, examples of which are a single missing atom or a single atom impurity in the pristine crystal. Our objective is to compute the energetics of these defects, and in particular:

- **Formation Energies.** The energy required to create the defect is related to the probability of having a certain concentration of that defect in thermodynamic equilibrium. To some extent, investigation of general properties of the defect in its ground state configuration, such as optical and electronic properties can also be included into this category. We will see that charged defects need careful consideration due to their localized charge distribution and interaction with periodic images.
- **Migration Barrier Energies.** Once the defects are formed, they can also move, and hop into different sites in the crystal (either a vacant or an interstitial site) via diffusion through the crystal. Although this happens at a much slower rate than in gases or liquids, it remains essential since it makes the foundation for industrial applications such as electrochemical

cells and batteries, solid oxide fuel cells (SOFC), nanoionics, super-ionic conductors, corrosion. Besides that, altering the electronic structure transiently upon illumination and changes in light-driven catalytic reactions can also be included into the dynamic properties.

As we said before, real materials are not infinite, but have boundaries. This is the second type of imperfections in the solid that we consider in this work, and we include under the general label ***Surfaces & Interfaces***. In atomic simulations a boundary can be modeled as a cleaved surface of the material. The structure and properties arising from this symmetry breaking are entirely different from the ideal bulk material. Studying these effects is another step towards realizing real material. Furthermore, creating a functional device requires two or more materials surfaces to be in contact and create interfaces. Understanding the physics in interfaces needs to be considered carefully. The study of surfaces and slabs allows to define concepts and approximations that act as the bridge to creating and investigating heterostructures. Note that hybrid materials are also technologically interesting. These materials are composites consisting of two constituents that enhance desired properties by combining those of the individual components. Here, the influence of point defects can also be critical. For instance, the heterostructure of (CNT) and metal oxide nanoparticles such as ZnO, due to defects enhance the UV emission, and has wide range of applications from photocatalysis [Byr+08], charge separation [ZJY09], field electron emission [Ken+17], photoresponse [Cho+20], gas or electrochemical sensors [BS17], to other optoelectronic devices [SSN13].

1.2 Defects & electronic properties

Lattice defects and impurities are prone to introduce new localized electronic states in the host. For example, vacancy defects create a level in the band gap due to "dangling bonds" (Figure 1.3). This is because orbitals do not substantially overlap with other atomic orbitals in crystal, and with no overlap with a neighboring orbital, there will be no symmetric-antisymmetric energy splitting. Moreover, orbitals with little or no overlap will look very much like the original atomic orbitals [Sno20]. The presence of a defect level is dictated by the nature of chemical bonding and crystal structure. If we consider transition metal-oxides, the presence of *intrinsic* defects often creates a level inside the bandgap. For instance

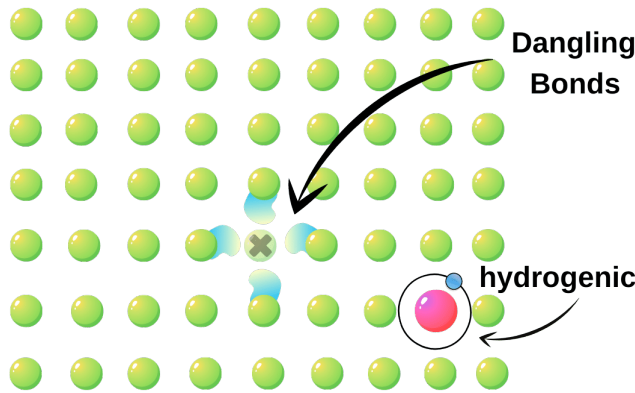


Figure 1.3: Creating a vacancy atom leaves dangling bonds in surrounding atoms (the dangling bond shown with cloud around neighbouring atoms and vacancy position is shown with \times). Creating impurities creates shallow donors (acceptors) hydrogenic levels.

interstitial metal ions introduce donor levels $M_i \rightarrow M_i^\bullet + e$, $M_i^\bullet \rightarrow M_i^{\bullet\bullet} + e$, ..., vacancies from the metal ion introduce acceptor levels $V_M \rightarrow V_M' + h$, $V_M' \rightarrow V_M'' + h$, ... On the other hand, oxygen vacancies give donor levels $V_O \rightarrow V_O^\bullet + e$, $V_O^\bullet \rightarrow V_O^{\bullet\bullet} + e$, ... as shown in Figure 1.4.

Thus, from the computational point of view it is not only interesting to determine the probability of having these defects (given by their formation energy), but also whether or not the defects give rise to new electronic levels, and thus can host different number of charges. In this case we say that the defect is *charged*, and these charged defects deserve special attention, as the long-range Coulomb interactions between periodic images of the defect introduces uncertainties in the definition of the formation energy, as we will discuss in the thesis. On the side, for some specific applications (for example in electronics or optoelectronics) it is important to find the accurate position of the defect level energy, and to distinguish whether it is a shallow or a deep level. There are thus two-aspects to consider here:

- (i) the accurate description of defect charge distribution.
- (ii) the accurate position of defect energy level in the gap

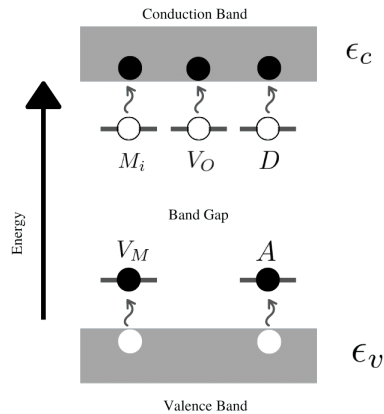


Figure 1.4: Localized electron states of point defects impurities in metal oxides: M_i =interstitial metal, V_M = metal ion vacancy, V_O = oxide ion vacancy, A = Acceptor impurity, D =Donor impurity.

The level of approximation of the theoretical description could affect these two components. Modern approaches to point defect calculations typically use *Density Functional Theory* and are based on the supercell approach, where the defect is introduced in a simulation box with up to a few hundred atoms of the perfect crystal hosting the defect. Periodic boundary conditions, needed to describe the crystal host, require the use of these large supercells to avoid artificial interactions between periodic images of the defect. Ab initio calculations are able to model defects more accurately than empirical potentials, but are limited by the larger computational demands which critically increase with the number of atoms in the system (typically as N^3 , where N is the number of atoms in the cell). In this sense, the so called *linear scaling* methods are advantageous as they allow to describe larger number of atoms at a reduced computational cost. These approaches normally exploit *localization*, and use some sort of localized basis as support functions to describe the electronic wavefunctions. Numerical atomic orbitals (NAO) which are products of spherical harmonics times radial functions, solution of the radial Schrödinger equation for an isolated pseudoatom, have demonstrated to give excellent performance both in terms of accuracy and computational cost relative to planewave calculations with equivalent pseudopotentials [Ang+02; Jun+01]. Transferability is generally

satisfied when using a few tens of orbitals per atom (versus hundreds of functions required for planewaves), which can be generated by optimization on a specific model crystal or molecule thanks to the variational principle. [Ang+02]

Here we use the robust SIESTA package under the framework of *Density Functional Theory (DFT)* along with a localized basis set (Numerical Atomic Orbitals) SIESTA allows us to work with big supercells and systems, which is an important requirement for defects calculations. One of our focus will be on the unfavorable side of NAO's in defect calculations, which is connected to the first issue highlighted above. By default, within localized basis set methods such as SIESTA, when creating a vacancy defect, one removes the corresponding atom along with its support basis orbitals. These could raise an important issue, whether the remaining basis set is good enough to describe the defective system or defect region. In particular, whether the basis set is good enough for describing the dangling bond state of the system where charges are localized in defect species' position. This problem also extends to study dynamic properties, such as diffusion barriers in which one wants to calculate the migration of the defect to a different crystal site.

1.3 Computational Material Science

1.3.1 The High-Throughput Computations Era!

The need to develop sophisticated and specialized materials is an unavoidable requirement for many aspects of our modern life. In the last decades it has become evident that computational tools play a significant role in these developments and research, as discussed in the case of point defects. Computational material science enables an accelerated progress in this process of materials discovery and optimization [SC03]. With the increasing power of the computer, not only could one accomplish a simulation at the atomic level, but do it for multiple or different cases exploring multiple conditions and computing several different properties simultaneously. Often, the calculation of particular properties requires more careful consideration or multiple steps. Also, occasionally one needs to explore thousands of materials to find the best candidate for particular properties or applications. Hence some software infrastructures are needed to automatize these procedures .

The different automatic infrastructures in the computational materials sci-

ence community that enable setting up and performing many simultaneous calculations and then collecting the data to analyze the results with minimal intervention by the user, have paved the road for rapid materials discovery and development [Joh+02; Mat+17; Xia+95]. These infrastructures have given birth to the High-Throughput Computations Era. A general requirement that any such platform should satisfy, is to provide the means to create, manage, analyze and share huge amounts of data from the computational simulations. There are multiple developments in the market, and many options in the public academic community. Among them, here we pay special attention to AiiDA, developed at EPFL. [Hub+20; Piz+16; Uhr+21]. The ADES model with four pillars for the Automation, Data, Environment, and Sharing was established to satisfy the essential requirements, and the AiiDA framework is implemented as an automated interactive infrastructure, and a database for computational science. One of the many significant advantages of AiiDA is its dynamic workflows. Besides controlling multiple steps in a simulation, these workflows can automatically store the data required to be stored, which need to be used later as they run. Hence, it will be ideal for calculating properties requiring multiple steps, such as defect formation and defect migration barriers.

1.3.2 Tools Available

Recently, various tools have become available in different ecosystems for extracting different properties, from the fundamental equation of state [Hub+21] to more advanced properties such as workfunction of slabs [And+21]. In this thesis, I have developed workflows for SIESTA code, which require some distinct features for their integration on the AiiDA materials informatics platform implemented by Pizzi *et al.* [Piz+16]. In particular, we will describe the developments of three different workflows that facilitate our practical interests:

- **defects workflow** to automate the calculation and analysis of the *formation energies* of point defects.
- **barriers workflow** to automate the generation, calculation and analysis of the *energy barrier* for migration of defect along different paths.
- **surfaces workflow** to automate the generation, calculation, and analysis of different slabs, surfaces and interfaces.

In the following chapters, we will demonstrate the theory and application of those tools.

1.4 Our case study systems: defects in Oxides

The family of oxide materials is among the most abundant in nature. They have astonishingly diverse structures, especially in comparison with simple metals or elemental semiconductors. For instance, the binary oxides in bulk can have the simplest rock-salt structure, or more complex ones such as spinel or antiferroite structures. Understanding the structures and properties of oxides is crucial for many modern technologies, from the application of dielectric oxides in microelectronic devices, or as transparent layers in optical coatings and solar energy harvesting devices, or even as protective corrosion layers on metals. Through the thesis, we focus on two relatively simple but interesting examples: MgO and HfO₂. We have chosen these two systems due to their being very well studied in the literature (thus we can validate our methods and results), and for their potential interest for applications which still raises questions regarding the properties of their defects (in particular oxygen vacancies). In the following we give a brief introduction to these defects.

1.4.1 Magnesium Oxide MgO

Magnesium oxide MgO is a prototypical binary oxide, highly symmetric, ionic, and with a broad electronic gap (experimental value 7.8 eV [WW69]). The oxygen vacancy defect gives rise to a well-localized s-like defect state that can be filled by 2 (F^0), 1 (F^+), or 0 (F^{2+}) electrons. This defect is an ideal system to study the methods developed to treat charge corrections needed to estimate the formation energies. In this case, the electronic state localized around the defect has a nice spherical symmetry so that simple standard models can be correctly applied and can be compared with more advanced methods described below. Furthermore, the limits of the strictly localized basis set can be tested under controlled conditions. On the other hand, this is a well-studied material and it is easy to find references in the literature with which we can compare our results, both for formation energies and migration barriers.

1.4.2 Hafnium(IV) Oxide HfO_2

Another system of interest from the large spectrum of oxides is HfO_2 (and also its cousin ZrO_2), which attracted much attention years ago due to their high dielectric constant κ , and its potential use for replacing silicon dioxide as the gate dielectric material in metal-oxide-semiconductor (MOS) transistors. Besides that, HfO_2 (and ZrO_2) is also used for thermal barrier coating and is one of the most common electrolyte materials in SOFCs. Notably it has been shown recently that HfO_2 also shows ferroelectricity [Mül+12] and its compatibility with silicon technology has renewed interest in ferroelectric memory devices, which make them an excellent candidate for ultrathin ferroelectric random-access memory (FE-RAM) ($< 10\text{nm}$) for the next commercial use [Mar+13]. In all these applications, the performance of HfO_2 can be potentially affected by the presence of defects. Hence it is interesting to use theoretical modeling to determine the formation of the most stable forms of oxygen vacancies. Moreover, we have chosen another interesting problem in the study of a hybrid HfO_2 /Graphene heterostructure, which has recently been synthesized and characterized as a promising candidate for energy harvesting applications. Theoretical modeling support has been asked from our collaborators to understand the experimental observations and determine the role of defects and the properties of the interface in this new hybrid nanomaterials.

1.5 Thesis Outline

The *Thesis* has four parts. In this first Part (i) **The Beginning of It All**, we have reviewed the power of first-principles, or *ab-initio* electronic structure methods, and the need for using these modeling tools to tackle the problem of defects in materials for technology. In Part (ii), **Defects Energies**, we will tackle the static properties of defects, particularly the formation energy of charged defects, by describing the problem and developing tools to solve the issue and its applications. Then, in Part (iii) **Defects Barriers**, we will move to dynamical properties, mainly defect migration. Finally, in Part (iv) **Surfaces & Interfaces**, we will discuss the surfaces and the application of defects on interfaces. Each Part contains two chapters (except the last Part, which has three chapters) focusing on the theoretical concepts and the application of the developed tools to the

issues at hand for that Part. The Last chapter will give the conclusive outlook of the Thesis. The organization of each chapter is as the following:

- **Chapter 2 - Theoretical Background** We begin the pilgrimage with a review of general steps in modeling and then describe the *ab-initio* approach. Next, we review the theory behind the power of *DFT* to extract the properties we need, which we will use throughout this *thesis*.
- **Chapter 3 - Defects Formation Energies Methods** I review the problem of the charged defect formation, which arises from periodic image interactions of localized charges, and the approaches to tackle this problem.
- **Chapter 4 - Defects Formation Energies Applications** I use the developed tools for different materials' charged defect formation energies. We start with MgO and conclude the chapter with HfO₂ oxide due to their peculiar behavior for the properties of the defect.
- **Chapter 5 - Potential Energy Surface (PES) Methods** I introduce the potential surface energy and its relation with barriers and diffusion concepts and methods, together with the tools developed here for energy barrier calculation. Finally, we conclude the chapter by introducing a catalogue of different types of paths for diffusion barriers in crystals.
- **Chapter 6 - Siesta Barriers Applications** I use the developed tools for barrier calculation and discuss the problem and solution for the method and the basis-set issue for calculating the diffusion barrier in MgO model system.
- **Chapter 7 - Methods for Surfaces & Interfaces** discusses different surfaces in materials and revisits the basis-set issue at the surface. Next, I review the *ab-initio* issues dealing with surfaces and solutions for those problems.
- **Chapter 8 - Siesta Surfaces Applications** Illustrates the developed tools to study HfO₂/Graphene Heterostructure and the effects of defects on its electronic properties and its possible application in photocurrent production.
- **Chapter 9 - Conclusions & Outlook** I give an outlook and conclusion to the study of defects, barriers, and surfaces issues.

2

Theoretical Background

2.1 Materials

In the interdisciplinary field of materials science, the aim is to design and discover new materials. In this thesis, we will work at the theoretical level, which is the subfield of materials science where mathematical tools are combined with fundamental laws of physics to study and engineer processes of chemical and physical relevance. In this chapter, I start outlining the different stages of materials modeling while emphasizing the level of complexity. Then, later in this same chapter, I will show how *DFT* provides an excellent solution to these problems, making it a powerful tool for calculating material properties.

2.2 Material Simulations

Materials simulation or modeling is the development and use of mathematical models for describing and predicting specific properties of materials. The initial effort is to describe the steps needed to set the theoretical framework for the modeling.

2.2.1 Fundamental Steps in the modeling

There are four fundamental steps in modeling:

- **System description** First, we have to define our system and the fundamental units or “particles” along with the number of those that are present there. This comes down to choosing what things we want to describe. If we want to describe atoms and molecules but not the internal structure of the atomic nucleus, we choose atomic nuclei and electrons as our building blocks. If we want to describe molecular structures but not the details of the electron distribution, we choose atoms as the building blocks. Larger building blocks can also be considered, such as molecules, nanocrystalites, etc.

- **Interaction** The next step describes the interaction between particles that constitute the system. In our case, we deal with arranged order of nuclei and electrons (building blocks) in crystalline systems. The interaction here will be the Coulomb interactions between nuclei and electrons, and any other possible external electromagnetic field.
- **Dynamical equation** The mathematical dynamical equation form for evolving the system in time could be different, and solving this equation might need different recipes. However, after solving those equations, one can predict the system information at any time (later or earlier) relative to the starting conditions, which is the Final GOAL!
- **Starting condition** The final step is to define the initial conditions. In the classical realm, this is basically, to define the particles' initial positions and their velocities. This is because the position and velocity of particles make the entire phase space, and all the dynamics occur in this configuration space. Depending on the number of particles of the system that we deal with, we could only be able to describe a small part of it. So the initial condition will allow us to focus on relevant parts of this space. So the initial condition will allow us to focus on relevant parts of this space.

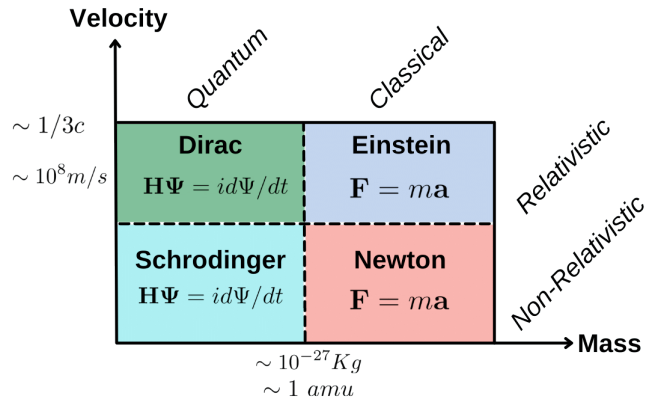


Figure 2.1: The mathematical framework for Four Domains of Dynamical Equations

The mathematical framework for the dynamical equation depends on the mass and velocity of the particles and can be divided into four regimes Figure 2.1.

- **Classical Non-Relativistic** When you deal with large and slow (slower than the speed of light) particles.
- **Classical Relativistic** When you deal with large and fast (near speed of light) particles.
- **Quantum Non-Relativistic** When you deal with very small particles (order of atoms) which move slowly (slower than the speed of light).
- **Quantum Relativistic** When you deal with very small (order of atoms) and fast (near speed of light) particles.

The atomic nucleus are heavy enough to be described at the classical non-relativistic regime, while electrons are light particles and require quantum mechanic treatment. In this thesis, our main mathematical framework is in the Quantum Non-Relativistic domain (although some relativistic effects might be included).

2.3 Ab-initio methods for Electronic Structure Calculations

2.3.1 The Adiabatic and Born–Oppenheimer Approximations

If we are interested in describing the electron distribution in detail, we have to rely to the Schrödinger equation (Quantum Non-Relativistic domain Figure 2.1). Solving the Schrödinger equation still requires approximations. We start with the *Born–Oppenheimer approximation*, where we decouple the nuclei and electronic motion, since the nuclei are orders of magnitude heavier than electrons. This allows the electronic part to be solved with the nuclear positions as parameters, and then use the resulting *Potential Energy Surface (PES)* as basis for solving the atomic nucleus dynamics. In this approximation, the total wave function can be written as:

$$\Psi_{tot}(\mathbf{r}, \mathbf{R}, t) = \Phi_n(\mathbf{R}, t) \Psi_e(\mathbf{r}; \mathbf{R}(t)) \quad (2.1)$$

where Φ_n are the nuclear wavefunctions (which can be taken as Dirac functions), and Ψ_e are the electronic wavefunctions which depend parametrically on the instantaneous atomic positions $\mathbf{R}(t)$. In the semiclassical approximation the

nuclear motion can be described with Newton's equation following the *PES* defined by the electrons, and the electronic wavefunctions can be obtained from the solution of the time-independent Schrödinger equation:

$$\mathbf{H}_e \Psi_e = E_e \Psi_e \quad (2.2)$$

with the electronic hamiltonian given by

$$\mathbf{H}_e = \left[\mathbf{T}_e + \mathbf{V}_{ee}(\mathbf{r}) + \mathbf{V}_{en}(\mathbf{r}; \mathbf{R}) \right] \quad (2.3)$$

where \mathbf{T}_e , \mathbf{V}_{ee} , and \mathbf{V}_{en} are the electronic kinetic energy, the electron-electron and the electron-nuclear interactions respectively.

2.3.2 Density Functional Theory : The Hohenberg-Kohn Theorems

Within *Born–Oppenheimer approximation* solving quantum N -body problem requires to work with wavefunction which for an N electron system contains $4N$ variables: three spatial ($r = x, y, z$) and one spin coordinate (α)

$$\Psi_e(r; \mathbf{R}) \longrightarrow \Psi_\alpha(r_1, r_2, \dots, r_N; \mathbf{R}) \quad (2.4)$$

There are different methods where the N -particle electronic wave function is the fundamental object. The *Hartree-Fock (HF)* model [Har28; HH35] can be considered as the branching points for more methods and approximations based on wave function, such as *Configuration Interaction (CI)* [Sha77] *Coupled Cluster* and *Semi-empirical methods* [Thi88].

Considering the fact that the electron density $\rho(\mathbf{r})$ is the square of the wave function integrated over $N - 1$ electron coordinates

$$\rho_\alpha(\mathbf{r}) = \int |\Psi(r, r_2, \dots, r_N; \mathbf{R})|^2 d\mathbf{r}_2 d\mathbf{r}_3 \cdots d\mathbf{r}_N \quad (2.5)$$

each spin density only depends on three spatial coordinates independent of the number of electrons. *Density Functional Theory (DFT)* uses this charge density $\rho(\mathbf{r})$, which depends only on three variables, as the fundamental object that contains all the relevant information for the quantum system. The pillar of *DFT* is based on the *Hohenberg-Kohn theorem* [HK64], which states that the lowest

energy of the system (in the ground state) E is a functional ¹ of the electron density $\rho(r)$ only.

$$E = F[\rho] \quad (2.6)$$

The proof of *Hohenberg-Kohn theorem* is based on the following three premises:

- (I) In the ground state the electron density $\rho(\mathbf{r})$ determines, within an additive constant, the external potential acting on the electrons, V_{ext} :

$$\rho(r) \rightarrow V_{ext} \quad (2.7)$$

- (II) The external potential V_{ext} determines uniquely the many-electron wave function Ψ of the system:

$$V_{ext} \rightarrow \Psi. \quad (2.8)$$

- (III) The total energy E of the system, is a functional of the many-body wave function through Eq 2.2:

$$\Psi \rightarrow E \quad (2.9)$$

combining all premises indicate that, in the ground state, the density determines the total energy:

$$\rho \rightarrow V_{ext} \rightarrow \Psi \rightarrow E \quad (2.10)$$

we can conclude that the total energy is a functional of the density $E = F[\rho]$. This energy that can be calculated from the charge density of the system from the framework of *DFT* will allow us to derive desired properties of materials.

1 a function is a prescription for producing a number from a set of variables (coordinates), while a functional is a prescription for producing a number from a function, which in turn depends on variables. A wave function and the electron density are thus functions, while the energy depending on a wave function or an electron density is a functional. We will denote a function depending on a set of variables with parenthesis, $f(x)$, while a functional depending on a function is denoted with square brackets, $F[f]$.

2.3.3 Density Functional Theory: Orbital-Free

Hohenberg and Kohn constructed the foundation for *Density Functional Theory (DFT)* by proving that the electron density ρ determines the ground state electronic energy. The energy functional could be divided into three parts, kinetic energy $T[\rho]$, attraction between the nuclei and electrons $E_{ne}[\rho]$, and electron–electron repulsion $E_{ee}[\rho]$ (the nuclear–nuclear repulsion is a constant within the *Born–Oppenheimer approximation*). The interaction between nuclei and electrons is Coulomb like:

$$E_{ne}[\rho] = - \sum_a^{N_{nuclei}} \int \frac{Z_a(\mathbf{R}_a)\rho(\mathbf{r})}{|\mathbf{R}_a - \mathbf{r}|} d\mathbf{r} \quad (2.11)$$

On the other hand, the $E_{ee}[\rho]$ term may be divided into a simple Coulomb term, $J[\rho]$, and “other stuff which shall include the exchange $K[\rho]$, and correlations terms.

$$J[\rho] = \frac{1}{2} \iint \frac{\rho(\mathbf{r})\rho(\mathbf{r}')}{|\mathbf{r} - \mathbf{r}'|} d\mathbf{r}d\mathbf{r}' \quad (2.12)$$

First definition of a functional for the kinetic energy was derived from a simple model of a uniform electron gas, and is known as the Thomas-Fermi model (TF) [Blo29].

$$T_{TF} = C_F \int \rho^{5/3}(\mathbf{r}) d\mathbf{r} \quad \text{with} \quad C_F = \frac{3}{10} (3\pi^2)^{2/3} \quad (2.13)$$

The functional $E_{TF}[\rho] = T_{TF}[\rho] + E_{ne}[\rho] + J[\rho]$ is known as the *Thomas-Fermi (TF)* model. The exchange term for this simple electron gas, derived by Bloch but commonly associated with the name of Dirac, can be expressed as

$$K_D[\rho] = -C_x \int \rho^{4/3}(\mathbf{r}) d\mathbf{r} \quad \text{with} \quad C_x = \frac{3}{4} \left(\frac{3}{\pi} \right)^{1/3} \quad (2.14)$$

Addition of the $K_D[\rho]$ exchange part to the TF model gives the *Thomas–Fermi–Dirac (TFD)* model [Dir30]. Note that no correlation functionals are included in these simple models.

2.3.4 Density Functional Theory: Kohn-Sham Theory

The main problem in orbital-free models is the inadequate representation of the kinetic energy. In Kohn-Sham (KS) approach, we map the actual density of N particle system to that of a fictitious system of independent (non-interacting) electrons with one electron wavefunctions ϕ_i . The density of this one-electron wavefunctions is used to represent the exact density of the N electron system. Now, in the Kohn-Sham (KS) formalism the kinetic energy functional is split into two parts, one that can be exactly calculated and another that can be added as a small correction term. The KS model is formally related to the HF method, sharing identical formulas for the kinetic, electron-nuclear, and Coulomb electron-electron energies. The non-interacting kinetic energy could be written by

$$T_S = \sum_{i=1}^{N_{elec}} \langle \phi_i | -\frac{1}{2} \nabla^2 | \phi_i \rangle \quad (2.15)$$

The exact density of the interacting electrons system is not known, but it can be represented by the density of the equivalent system made of auxiliary non-interacting electrons

$$\rho = \sum_{i=1}^{N_{elec}} |\phi_i|^2 \quad (2.16)$$

The remaining part of total kinetic energy $T[\rho]$ now is in exchange-correlation term, and the total $E_{DFT}[\rho]$ can be written as

$$E_{DFT}[\rho] = T_S[\rho] + E_{ne}[\rho] + J[\rho] + E_{xc}[\rho] \quad (2.17)$$

By setting the E_{DFT} to the exact Ground State energy $E_{GS}[\rho]$, we can define E_{xc} from the difference between the kinetic energy terms and the electronic interactions

$$E_{xc}[\rho] = (T[\rho] - T_S[\rho]) + (E_{ee}[\rho] - J[\rho]) \quad (2.18)$$

2.3.5 On Exchange–Correlation Functionals

Now we have to approximate the V_{xc} or $E_{xc}[\rho]$, which has a direct relation with it. Beginning with the assumption that this electron density varies slowly at each point in the solid. One could regard it as a *homogenous electron gas (HEG)*. This approximation is called *Local Density Approximation (LDA)* [Dir30; KDT18; Raj78]. Consequently, we write

$$E_{xc}[\rho] \approx E_{xc}^{LDA}[\rho] = \int d^3\mathbf{r} \rho(\mathbf{r}) \epsilon_{xc}^{HEG}[\rho(\mathbf{r})] \quad (2.19)$$

If a semi-local generalized gradient of electron density is added to the approximation, it improves the approximation and is called *generalized gradient approximation (GGA)* [PBE96]. Therefore for $E_{xc}[\rho]$ we have

$$E_{xc}[\rho] \approx E_{xc}^{GGA}[\rho, \nabla\rho] = \int d^3\mathbf{r} \rho(\mathbf{r}) \epsilon_{xc}^{GGA}[\rho(\mathbf{r}), \nabla\rho(\mathbf{r})] \quad (2.20)$$

These two approximations are widely used in the electronic structure community and are the workhorse for most of the calculations in the literature. There are different functional forms for LDA and GGA, and in the technical details of our calculations we will comment on which ones were used in this thesis.

2.3.6 Self-Consistency Field (SCF) Method

We can rewrite the Kohn-Sham equations as following

$$\left[-\frac{1}{2}\nabla^2 + V_{tot}(\mathbf{r}) \right] \phi_i(\mathbf{r}) = \epsilon_i \phi_i(\mathbf{r}) \quad (2.21)$$

$$V_{tot}(\mathbf{r}) = V_{ne}(\mathbf{r}) + V_H(\mathbf{r}) + V_{xc}(\mathbf{r}) \quad (2.22)$$

$$V_{ne}(\mathbf{r}) = - \sum_I \frac{Z_I}{|\mathbf{r} - \mathbf{R}_I|} \quad (2.23)$$

$$\nabla^2 V_H(\mathbf{r}) = -4\pi\rho(\mathbf{r}) \quad (2.24)$$

$$V_{xc} = \frac{\delta E_{xc}[\rho]}{\delta\rho}(\mathbf{r}) \quad (2.25)$$

$$\rho(\mathbf{r}) = \sum_i |\phi_i(\mathbf{r})| \quad (2.26)$$

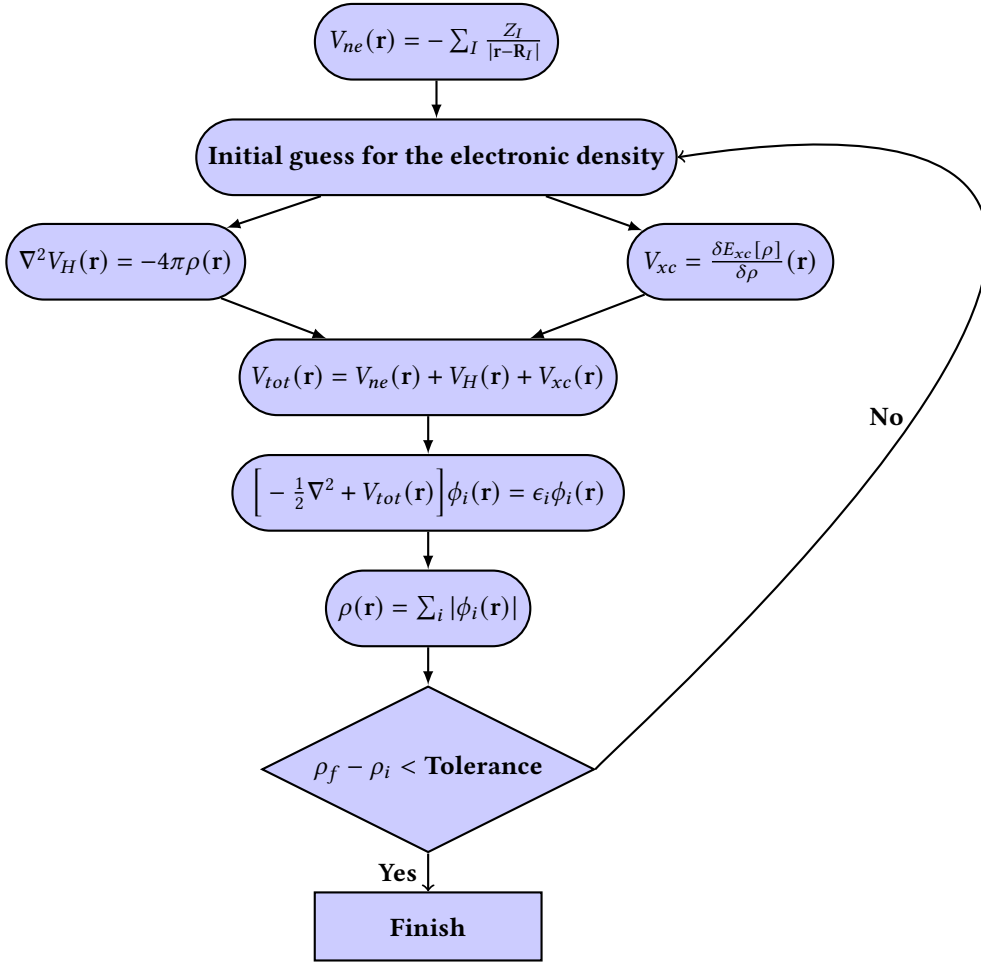


Figure 2.2: self-consistent solution flow-chart for Kohn-Sham equations

Since the solution depends on the electron density, as in the Hartree-Fock approach, we have to use a self-consistent procedure to solve the Kohn-Sham equation as shown in Figure 2.2. Typically, we need an initial guess for the electronic density, which can be taken as the sum of the densities of isolated atoms placed at the atomic positions of the new structure. The V_{tot} is then computed from that initial density, and the Kohn-Sham equations are solved to obtain $\phi_i(\mathbf{r})$. These Kohn-Sham orbitals are then used to define a new electronic

density following Eq 2.26. This procedure continues until the changes in the density between SCF steps are smaller than the tolerance parameter defined at the beginning of the cycle.

2.4 The SIESTA Method

The implementation of the self-consistent Kohn-Sham density functional theory is available in the SIESTA package. SIESTA (Spanish Initiative for Electronic Simulations with Thousands of Atoms) is a DFT method based on a flexible linear combination of atomic orbitals (LCAO) basis set. The implementation of the method in a computational code allows extremely fast simulations using minimal basis sets and very accurate calculations with complete multiple-zeta and polarized bases, depending on the required accuracy and available computational power. The SIESTA method applies two important approximations (i) use of Pseudopotentials that allows to keep frozen the wavefunctions of the core electrons in the atom, and thus take into account only on the valence electrons, that feel a screened electrostatic potential from the nuclei; and (ii) use of strictly localized Numerical Pseudo-Atomic Orbitals as the basis functions to expand the electronic wavefunctions. These two approximations require to define two critical aspects of any SIESTA calculation: defining the specific "input" variables:

- **Pseudopotential:** the replacement of the core electrons by an effective potential that acts on the valence electrons and provides an explicit description only for the valence electrons ² This approximation comes in very handy and presents several advantages as it not only reduces the number of electrons, but also the complexity of the wavefunctions. This helps in the reduction of the basis size since we are dealing with states involving only the valence electrons. Furthermore, this allows to use a uniform spatial grid instead of a logarithmically dense grid closer to the center of the atom that could have been needed due to the acute localization of the core electrons. Moreover, it allows the replacement of the atomic wavefunction that contains nodes with a smooth function without nodes. The replacing of the all-electron with pseudo electron function gives an exact match to the all-electron (true) wavefunction beyond the

² which is common to many other approaches including the most widely used ones based on plane-waves such as quantum-espresso, vasp and abinit.

pseudopotential cut-off radii r_c . This radii can be fine-tuned for each angular channel independently.

- **Numerical Pseudo-Atomic Orbitals (NAO or PAO):** The NAOs ($\phi_{Ilmn}(\mathbf{r})$) are orbitals centered on atoms and made up of an spherical harmonic $Y_{lm}(\mathbf{r})$ and a numerical radial function $\phi_{Il n}(\mathbf{r})$, which is zero beyond a certain radius, as follows:

$$\phi_{Ilmn}(\mathbf{r}) = \phi_{Il n}(\mathbf{r}_I) Y_{lm}(\hat{\mathbf{r}}_I) \quad (2.27)$$

where I is the atoms' index, n is the principal quantum number, l is the angular quantum number, m is the magnetic quantum number and $\mathbf{r}_I = \mathbf{r} - \mathbf{R}_I$ is the vector position relative to the center of the atom \mathbf{R}_I . The radial function $\phi_{Il n}(\mathbf{r}_I)$ can actually be made from just one function, or a linear combination of several radial functions (zeta) ζ for each angular momentum channel, which corresponds to single- ζ or multiple- ζ basis orbitals.

Throughout this *Thesis*, we have used the implementation of the self-consistent Kohn-Sham density functional theory available in the SIESTA package. We'll try to formulate a theory that allows us to describe our system (matter) and extract the relevant properties. The following section will define the meaning of property and shortly review a couple of different properties of matter.

2.4.1 Materials Properties

We choose materials to perform well in certain applications. When we use a material in a certain application, we know that it will be subjected to particular external conditions, e.g., a constant load, or a high temperature, or perhaps an electrical current running through the material. In all these cases, we must make sure that the material responds in the desired way. In general, we want a material to have a particular response to a given external influence. We will represent the external influence by the symbol \mathbb{F} , which stands for Field. This could be an electrical or magnetic field, a temperature field, the Earth's gravitational field, etc. The material will respond to this field, and its Response is described by the symbol \mathbb{R} . For instance, the response of a steel beam to an external load (e.g., a weight at the end of the beam) will be a deflection of the beam. In the most

general sense, the relation between field and response is described by

$$\mathbb{R} = \mathbb{R}(\mathbb{F}) \quad (2.28)$$

If the Response function is a "well behaved" function we could expand the function with aid of Taylor expansion

$$\mathbb{R} = \mathbb{R}_0 + \frac{1}{1!} \frac{\partial \mathbb{R}}{\partial \mathbb{F}} \Big|_{\mathbb{F}=0} \mathbb{F} + \frac{1}{2!} \frac{\partial^2 \mathbb{R}}{\partial \mathbb{F}^2} \Big|_{\mathbb{F}=0} \mathbb{F}^2 + \dots + \frac{1}{n!} \frac{\partial^n \mathbb{R}}{\partial \mathbb{F}^n} \Big|_{\mathbb{F}=0} \mathbb{F}^n \quad (2.29)$$

where \mathbb{R}_0 describes the "state" of the material at zero field. If we truncate the series after the second term (i.e., we ignore all derivatives of \mathbb{R} except for the first one), then the expression for \mathbb{R} is simplified dramatically

$$\mathbb{R} = \mathbb{R}_0 + \mathbb{P}\mathbb{F} \quad \text{with} \quad \mathbb{P} = \frac{1}{1!} \frac{\partial \mathbb{R}^{Response}}{\partial \mathbb{F}} \Big|_{\mathbb{F}=0} \quad (2.30)$$

This is a linear equation between the applied field and the response. The quantity \mathbb{P} is known as a material property. There are many material properties, and the most important ones are linear properties, meaning that there is a direct proportionality between the field and the response. Other properties are quadratic in the field or even higher order. Out of many different types of material properties, here we list a couple of them:

- Mechanical Properties
- Magnetic Properties
- Electric Polarization Properties
- Electric Conductivity Properties
- Thermodynamics Properties
- Thermoelectric Properties
- Optical Properties
- Ionic Conductivity Properties

Depending on the desired property, it could be evaluated with linear or higher order terms. In the first approximation, the properties are considered with linear

dependency. *DFT* is a theory that allows to obtain the ground state energy, and thus can be conveniently used to extract, from first principles, properties that derive from changes in the total energy over external perturbations on the conditions that allow to define the ground state, such as the atomic structure, the atomic positions, the external electromagnetic fields, etc. For example, if we consider deformation of the crystal structure, by application of an external strain deformation ϵ , we can obtain mechanical properties, such as the stress:

$$\sigma_{i,j} = \frac{1}{\Omega} \frac{\partial E_{DFT}}{\partial \epsilon_{i,j}} \quad (2.31)$$

Where the σ is a linear order property tensor which depends on the change of the atomic coordinates from equilibrium with

$$R'_{Ii} = \sum_j (\delta_{i,j} + \epsilon_{i,j}) R_{I,j} \quad (2.32)$$

Besides symmetric ideas, the stress property depends on the bonding, hence the charge density concentration in particular directions in the crystal atoms neighborhood. In this *Thesis* we focus on general *defect properties*, mostly energetics. These include formation energies but also migration energies linked to *ionic conductivity*. We also address the effects of *surfaces* on the defect properties in the material. These properties will be estimated from total energy computed at the *DFT* level, and/or derivatives of the energy with respect to the atomic positions, which are the forces:

$$\mathbf{F}_I = - \frac{\partial E_{DFT}}{\partial \mathbf{R}_I} \quad (2.33)$$

where I is index of atom. Hence we could call them the linear response of energy to the atomic distortion.

Part II

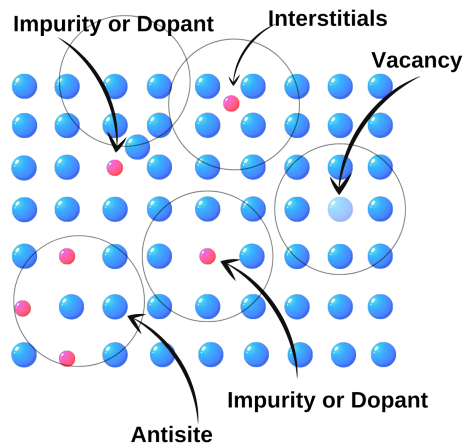
Defects Energies

3.1 Defects

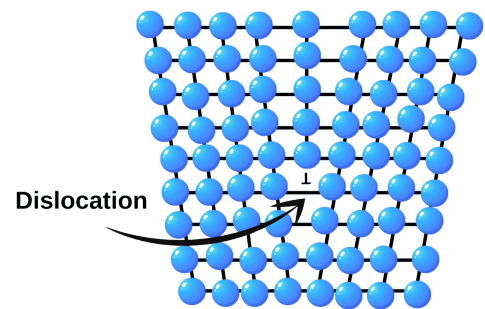
Defects play an essential part in both the chemical and physical behavior of solids. An important part of modern science and technology is closely related to an effort to exploit or suppress the properties that defects confer upon a solid. Batteries, fuel cells, sensors, displays, or computer memories all directly utilize, or have evolved from, an understanding and manipulation of defects in materials [Li+19; Qi+20; SH17]. This technology developed over 80–100 years and started with the most simple ideas [Kre81]. The simplest concept of a defect is a point defect, which is an imperfection in the crystal site, such as a missing atom or an impurity. Not long after recognizing point defects, the concept of more complex structural defects, such as linear defects, termed dislocations, was invoked to explain the mechanical properties of metals [Fre65; RAC84; Wol89]. In the same period, it became apparent that planar defects, including surfaces and grain boundaries, and volume defects play essential roles in influencing a solid's physical and chemical properties [Sak+95]. Moreover, as the defects influence on the properties of the solid gradually became realized, the concept of a defect underwent considerable evolution [Han+19; Rho+19; Sun+18]. Nowadays, we can organize defects in a dimensional hierarchy, as shown in Figure 3.1:

- (i) Zero-Dimensional defects (point) defects—vacancies [FGC05]
- (ii) One-Dimensional (linear) defects—dislocations [Wal+04]
- (iii) Two-Dimensional (planar) defects—external and internal surfaces [Li+21]
- (iv) Three-Dimensional (volume) defects—point defect clusters [Li+15], voids [Bag+21], precipitates [Bou+20]

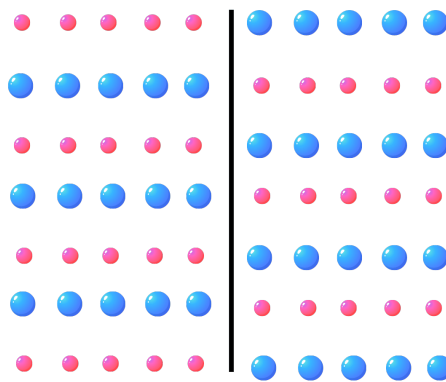
From the different types of defects, point defects influence many aspects of semiconductor behavior. For example, they can be electrically charged in bulk or on the surface. This charge state of defects can also affect defect properties such as structure, thermal diffusion rates, trapping and recombination rates for



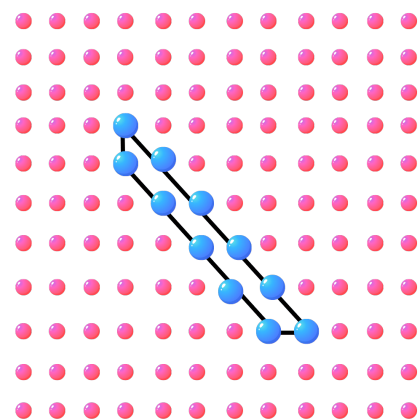
(a) Zero-dimensional defects—point defects



(b) One-dimensional (linear) defects—dislocations



(c) Two-dimensional (planar) defects—external and internal surfaces



(d) Three-dimensional (volume) defects—point defect clusters, voids, precipitates.

Figure 3.1: Dimensional hierarchy of defects in crystals (a) 0D defects known as point defects (b) 1D defects known as linear defects, dislocation is an example of it (c) 2D defects known as planar defects and (d) 3D defects such as clusters of point defects, voids and precipitates

electrons and holes, and luminescence quenching rates [Kre81]. This part of the *Thesis* is concerned with "isolated" point defects, that is low concentration of the defect in almost pure stoichiometric solids. Therefore, it is a good idea to identify which are these point defects at this moment.

3.1.1 Point Defects Catalogue

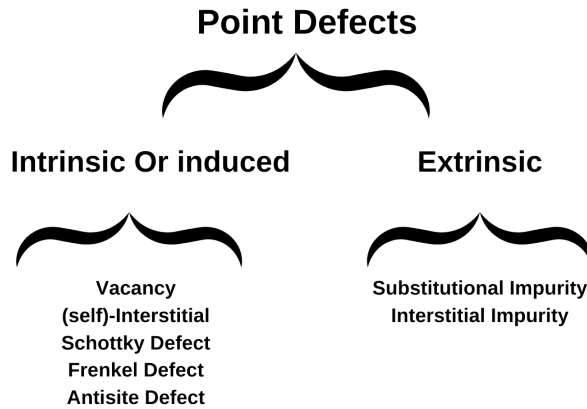


Figure 3.2: The diagram of point defect categorization

The starting point for categorizing the defect will be the thermodynamic stability. If defects form during the crystal growth they are called *native* defects. Ultimately, the *induced* class of defects form after the growth [PFL00], subject to external influence such as irradiation by high-energy particles (ion implantation) or other forms of radiation. Under thermodynamic equilibrium, some defects cannot be eliminated from the solid; these defects also fall into the class of *intrinsic* point defects [Wat96]. An external chemical specie not belonging to the host material but present in a crystal for any reason is called an extrinsic defect.

Now we can make further subcategories for these intrinsic, induced, and extrinsic defects. However, to accomplish this, first we go one step ahead to classify the defects by distinguishing the number of constituting elements in the crystal. For example, if a crystal is made from just one single atomic specie M , we call it monoatomic crystal. If it is built from more than one type of atom such as M, X, Y, Z, \dots we have a compound crystalline system. The binary compound MX would be the simplest one of these. Different defect types could be identified, depending on the nature of the crystal, either monoatomic or compound. Figure

3.2 shows all the categorization of these defects, and we explain the mentioned definitions in the following sections.

Point Defects in Monoatomic Crystals

The monoatomic crystal's defects are the first we consider. Let us imagine the M as the crystal element. The simplest point defect is an atom's absence at the crystal's lattice site; this is called *vacancy* of M and given the Symbol of V_M Figure 3.4-(d). Suppose the atom M does not occupy the usual site of the crystal during the crystallization. In that case, we call it *interstitial* and given the Symbol of M_i Figure 3.4-(a). Finally, we can consider an impurity of a different chemical specie C which is forced into the crystal by an exterior influence. If C occupies an interstitial site in the crystal, then it is called *interstitial impurity*, and is given the symbol of C_i Figure 3.4-(b). If it occupies a crystal site, and replaces a M atom from its site, then it is called *substitutional impurity* given the symbol of C_M Figure 3.4-(c). Finally, we could have a Frenkel defect, which is nothing but an atom M leaving its original site and occupying an interstitial site, that is a pair of an interstitial and a vacancy.

Point Defects in Compound Crystals

These compounds are crystals made from more than one chemical element. The easiest way to categorize is to consider the most straightforward case of a MX compound, which is made of an equal number of cations M and anions X. A *Schottky* defect is defined by a pair of vacancies, one for a cation and one for an anion, Figure 3.5-(a). If either an anion or a cation moves away from the sublattice site to an interstitial site we have a *Frenkel* defect, Figure 3.5-(b), which is thus formed by an interstitial and a vacancy as in the monoatomic crystal. *Antisites* are formed when one chemical specie occupies the site of the other, Figure 3.5-(c). For example, M placed at a X site forms the M_X antisite, and X placed at the M sites for the X_M antisite. The definition of *Interstitial impurity* Figure 3.5-(d) and *Substitutional impurity* Figure 3.5-(e) is similar to monoatomic ones which we discuss in following section.

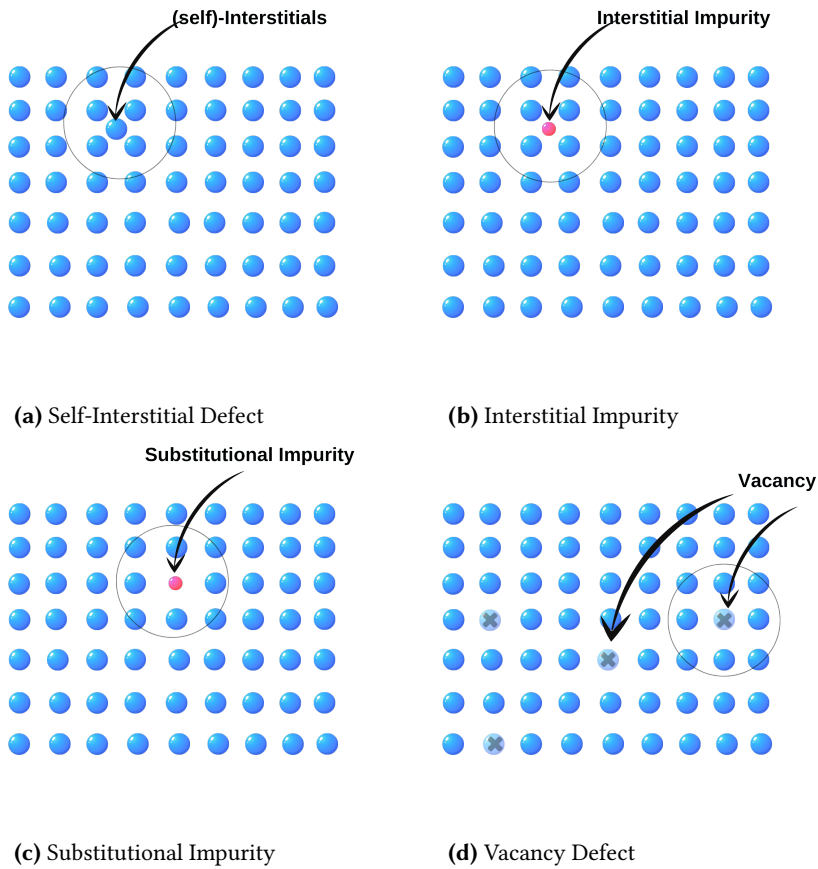


Figure 3.3: Type of Defects in Monoatomic crystal

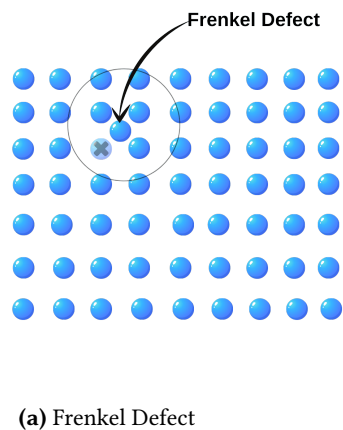


Figure 3.4: Type of Defects in Monoatomic crystal

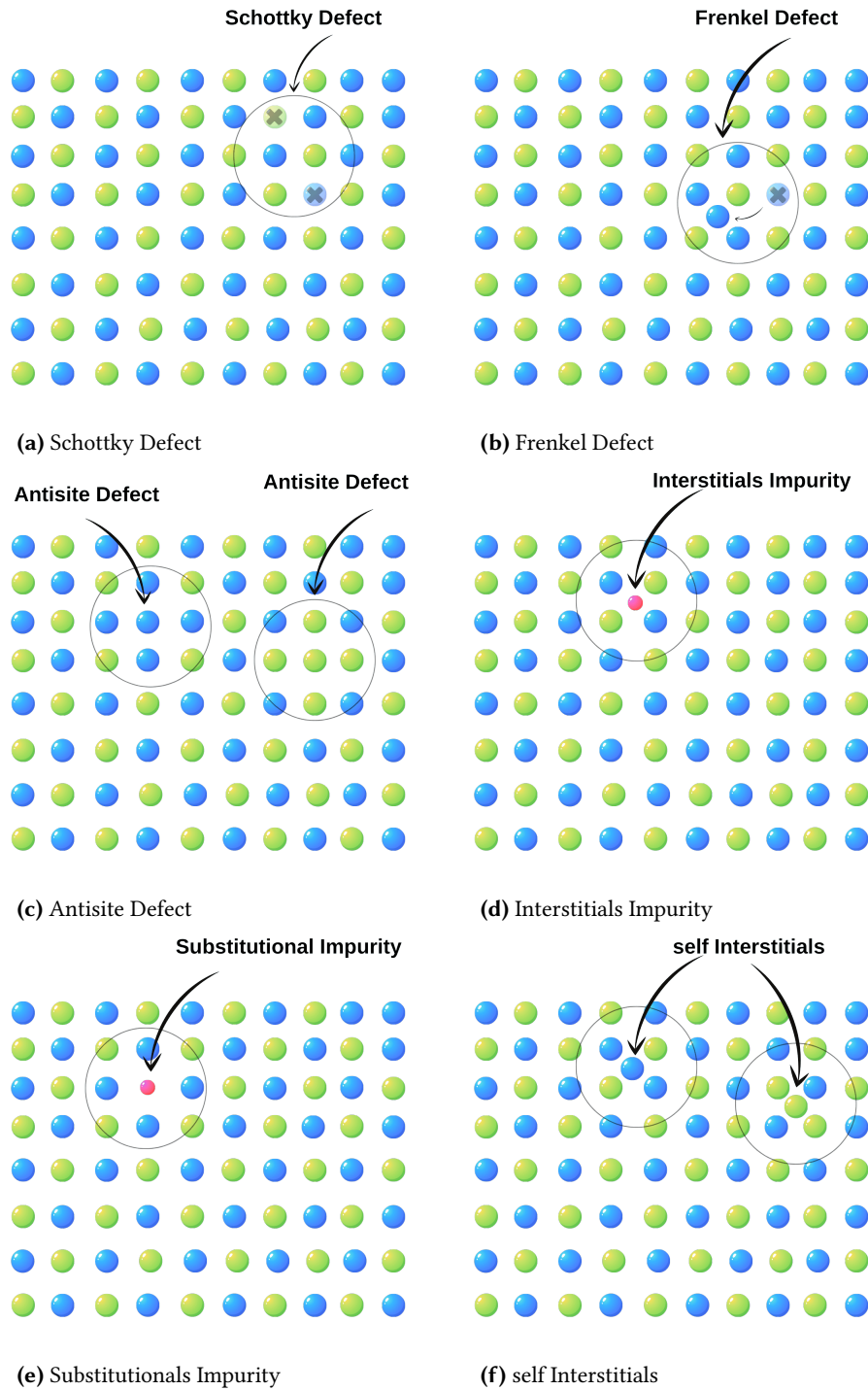


Figure 3.5: Type of Defects in Compound crystal

Charges on Defects and Kröger-Vink Notation

Defect Type	Notation
M Vacancy at M site	V_M
X Vacancy at X site	V_X
Interstitial at M site	M_i
Interstitial at X site	X_i
Interstitial Impurity C	C_i
M Vacancy with negative effective charge	V'_M
X Vacancy with positive effective charge	V^\bullet_X
Impurity C at M site	C_M

Table 3.1: Kröger-Vink Notation for Defects in Crystals

In general, the absence of a positive ion will leave a vacancy with an effective negative charge, thus it is called a negatively charged vacancy. Conversely, the absence of a negative ion will leave a site with an effective positive charge, and is called positively charged vacancy. Placing back the charges in those vacancies make them neutral. To describe the different charge states of vacancy, or any defect for the matter, could be intuitively tricky. To bypass the problem of notations and define the charge states of defects, we follow the notation of *Kröger-Vink*, where they considered the effective charge on defects [KV56].

The effective charge on a defect is the charge that the defect has, relative to the charge present at the same site in a perfect crystal. For ionic species, this is equal to the difference between the actual charges on the defect species, z_d , minus the actual charge at the site occupied in a perfect crystal, z_s :

$$q_e = z_d - z_s \quad (3.1)$$

To distinguish effective charges from real charges, the superscript $'$ is used for each unit of effective negative charge and the superscript \bullet is used for each unit of effective positive charge. The real charges of the species are still given the superscript symbols $-$ and $+$. Now the *Kröger-Vink* notation can be written as $A_l^{q_e}$, where A is the species, l is the lattice site and q_e is the effective charge. As an example, let us focus on the oxygen vacancy in ionic crystals such as MgO (Figure 3.6). In this material, Mg^{+2} ions carry two positive charges, and O^{-2}

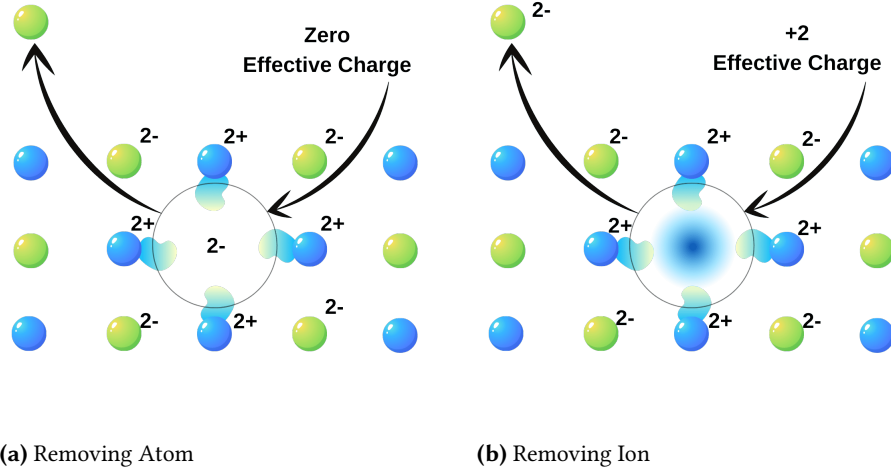


Figure 3.6: Illustration of the *Kröger-Vink* notation for Oxygen vacancies in MgO. Mg and O atoms are represented as blue and green spheres respectively. (a) neutral O atoms is removed from the lattice, leaving two electrons at the vacancy site. The surrounding Mg^{+2} charges compensate the vacancy charge, resulting in a neutral effective charge. (b) The oxygen anion (with the two electrons on the O) is removed. This leaves a positive effective charge due to the local environment around the vacancy

carry two negative charges. If we remove one neutral atom, O, the two extra electrons that were linked to the anion will remain in the system (donated by the surrounding Mg^{+2} ions), and result on a vacancy site with $-2e$ (panel a). This gives an effective charge

$$q_e = (-2 - (-2)) = 0 \quad (3.2)$$

and we call this a *neutral defect*. Thus, the vacancy appears to take an effective positive charge equivalent to $q_e = 0$ and is denoted as V_O .

On the other hand, when we remove the anion O^{-2} , we remove the neutral O atom with the two electrons that were linked to the site, which now gives $z_d=0$, and the effective charge becomes:

$$q_e = (0 - (-2)) = +2 \quad (3.3)$$

Thus, the vacancy appears to take an effective positive charge equivalent to

$q_e = +2$ and is denoted as $V_O^{\bullet\bullet}$. Throughout the *thesis*, we will follow *Kröger-Vink* notation. Hence, in a crystal containing defects, some charge fraction may be free to move through the matrix unless we remove that extra charge/s and make the defects in charged states. As a crucial remark, we return to it in Part II & III.

3.2 Defects Formation

The energy and entropy of materials depend on the types of atoms and their mutual arrangements, parameterized as “*state variables*”. Thermodynamics controls the states of matter. In our case, we are interested in finding out the likelihood or concentration of defects present in a crystal. In this section we will focus on this aspect.

When the system is in equilibrium, a Thermodynamics study gives information about its possible states. We know that the *Gibbs free energy* is the thermodynamical potential which describes the amount of energy required to add or remove species in the system. We can approximate the Gibbs energy of a crystal as

$$\mathcal{G} = \sum_i \mu_i N_i \quad (3.4)$$

$$\mathcal{G} = \mathcal{H} - TS \quad (3.5)$$

where μ_i and N_i are chemical potential and number of particle i respectively, \mathcal{H} is the *enthalpy*, S is the *entropy*, and T is the crystal’s *temperature* in K . Under equilibrium, if defects such as vacancies form spontaneously in the crystal³, the change in Gibbs energy with respect to the pristine crystal must be negative. However, the introduction of more and more defects must cause the Gibbs energy to increase until at some point it becomes positive (otherwise the crystal will not be stable and it won’t exist). This behaviour of Gibbs energy implies that, if defects are to be present at equilibrium, the form of the Gibbs energy curve as a function of the number of defects must go through a minimum, Figure 3.7.

The change in the Gibbs energy of the crystal by an amount $\Delta\mathcal{G}_{vacancy}$, due to the introduction of $n_{vacancy}$ vacancies distributed over N_{Sites} possible atom sites

- 3 Vacancies are easier to analyze since we remove the complexity of interstitial and another type of defects which have more degrees of freedom. However, all of the concepts from this analysis can be easily extended to any defects.

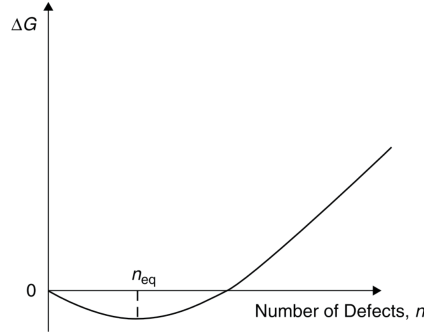


Figure 3.7: Change in Gibbs energy, $\Delta\mathcal{G}$, of a crystal as function of the number of point defect present. (Figure is taken from [Til08]).

is given by

$$\Delta\mathcal{G}_{vacancy} = \Delta\mathcal{H}_{vacancy} - T\Delta\mathcal{S}_{vacancy} \quad (3.6)$$

where $\Delta\mathcal{H}_{vacancy}$ is the associated change in enthalpy and $\Delta\mathcal{S}_{vacancy}$ the change in the entropy of the crystal. The $\Delta\mathcal{H}_{vacancy}$ term is approximately equivalent to the bond energy spent in forming the defects. The $\Delta\mathcal{S}_{vacancy}$ term is equivalent to the additional randomness in the crystal due to the defects Figure 3.8. To find $\Delta\mathcal{G}_{vacancy}$, it is necessary to determine the change in the enthalpy $\Delta\mathcal{H}_{vacancy}$ and the change in entropy $\Delta\mathcal{S}_{vacancy}$. Because the enthalpy tends to be associated more with the bonding energy between nearest neighbors, this term can be regarded as constant as a first approximation (independent of temperature). The entropy change consists of two terms: (i) vibrational entropies of the atoms around the defects (which will be an important factor at high temperatures) Figure 3.8-(b) and (ii) the arrangements of the defects in the crystal Figure 3.8-(c) and (d). This latter quantity, called the *configurational entropy*, is relatively easy to assess using well-established methods of statistical mechanics. For defects, we have a number of vacant sites $n_{vacancy}$, and the probability of having them randomly distributed among N_{Sites} is given by

$$\frac{n_{vacancy}}{N_{Sites}} = \exp\left(\frac{-\Delta\mathcal{G}_{vacancy}}{RT}\right) \quad (3.7)$$

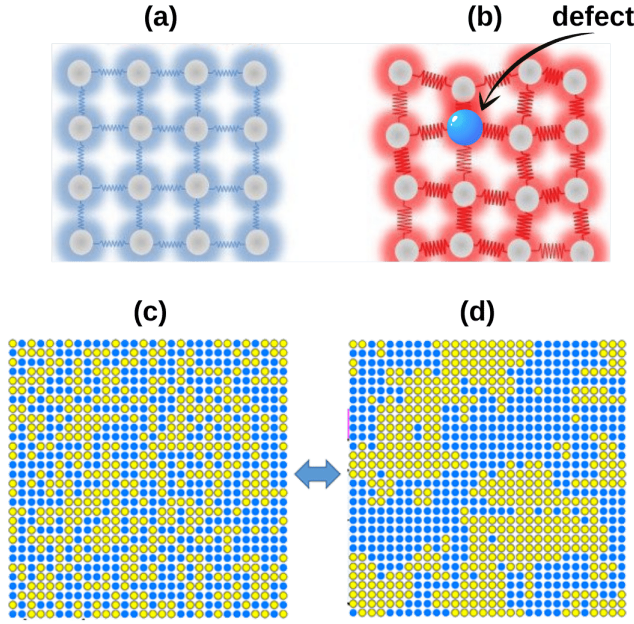


Figure 3.8: (a) Pristine vibrational entropy (b) defected vibrational entropy (c) Configurational entropy $S_1^{Configurational}$ (d) Configurational entropy $S_2^{Configurational}$. Since it was ordered, the (d) system has smaller configurational entropy than system (c) ($S_1^{Configurational} > S_2^{Configurational}$). (The figure is adapted from [SL20])

Where N_{Sites} is total number of normally occupied atom sites, R is the gas constant and T temperature in K. Using Eq 3.4 we get

$$\frac{n_{vacancy}}{N_{Sites}} = \exp\left(\frac{-\Delta\mathcal{H}_{vacancy}}{RT}\right) \times \exp\left(\frac{\Delta S_{vacancy}}{R}\right) \quad (3.8)$$

The quantities $\Delta\mathcal{H}$ and ΔS are often assumed to be temperature independent. This is a reasonable approximation, although the vibrational component of the entropy, which has been neglected altogether, becomes increasingly important at high temperatures. The effects of these factors can cause changes in the expected defect concentrations as the temperature increases. Thus, neglecting entropic

contributions, valid for relatively low temperatures, we have

$$\frac{n_V}{N} = \exp\left(\frac{-\Delta\mathcal{H}_V}{RT}\right) \quad (3.9)$$

For the rest of this chapter we focus on the formation energy (enthalpy energy) of (point) defects, mostly vacancies, and neglect the entropic part. The enthalpy \mathcal{H} is given by

$$\mathcal{H} = E + PV \quad (3.10)$$

and the change on enthalpy given by

$$\Delta\mathcal{H}_{vacancy} = \Delta E_{vacancy} + \Delta(P_{vacancy}V_{vacancy}) \xrightarrow{0} \quad (3.11)$$

At $T = 0$, the condition for stable structure at constant pressure P is to have a minimum enthalpy. Assuming the volume and pressure of cell in a defective system is not changing, the second term becomes zero. Finally, the thermodynamically relevant quantity becomes the Gibbs energy of formation \mathcal{G}

$$\Delta\mathcal{G}_{vacancy} = \Delta E_{vacancy} \quad (3.12)$$

where E can be calculated within the framework provided by *DFT* using Eq 2.17. The following section discusses how we can calculate this energy in crystalline systems.

3.2.1 Calculating defect formation energies under Periodic Boundary Conditions (PBC)

Dealing with perfect crystalline material means dealing with copies of some repeating unit (the unit cell [Blo28; Blo29]) in an orderly fashion, as shown in Figure 3.9-(a). However, a defect in the crystal breaks the translational symmetry of the host. Periodic Boundary Conditions, which are commonly used in electronic structure codes, imply that the defect is also periodically repeated. Thus, to model an isolated defect, we need to use a *supercell approach*, which places the point defect within a number of repetitions of the host crystal (the *supercell*), which is itself repeated (although with a different periodicity) and should be large enough for the interactions between the periodic images of the defect to

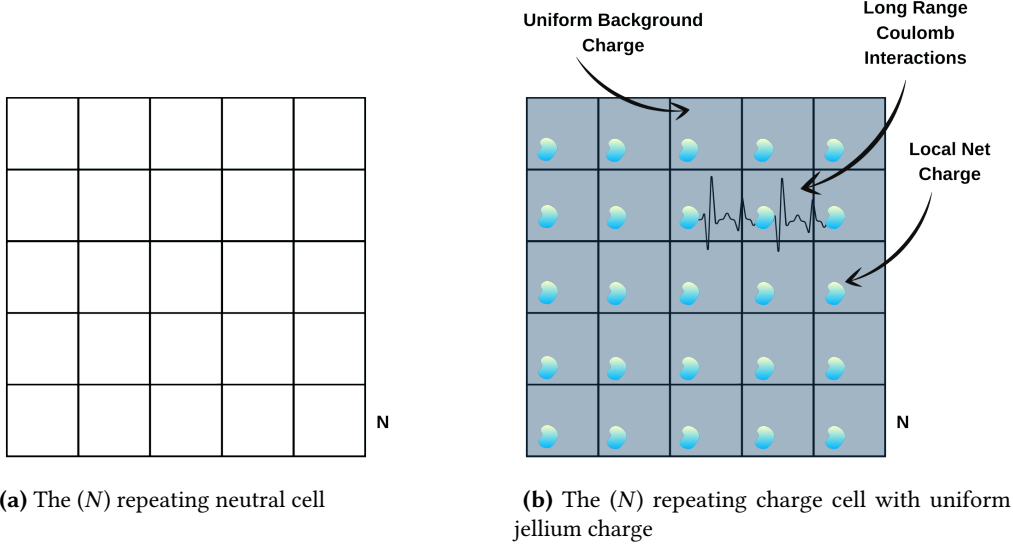


Figure 3.9: Neutral and Charge Defect in PBC (a) Total Neutral charge in *PBC* where $\rho_{elec}(\mathbf{r})$ and $\rho_{ionic}(\mathbf{r})$ cancel out each other in a cell. (b) The charged system where the net charge is shown in the cloud distribution and neutralizing uniform charge jellium $\langle n \rangle$ is shown as blue background in the cell.

be small and safely neglected. Otherwise, electronic states induced by the defect can hybridize with their periodic images, giving rise to dispersive bands and blurring the estimation of the *isolated* defect's energy. In the case of a charged defect, the situation is even more delicate. Introducing an excess of charge adds extra long range Coulomb interactions with the periodic images. This requires a very large supercell to have a good screening, making the calculations extremely expensive. In the following we will revisit the electrostatics under periodic boundary conditions and sketch the solution for these problems.

To calculate the formation enthalpy (energy) of defects, we take the difference between the energies of the pristine crystal and the system with the defect. So now, we focus on calculating these energies from *DFT* and, in particular, in *Periodic Boundary Conditions (PBC)*. The electrostatic potential, $V(\mathbf{r})$, resulting from a given charge density, $\rho(\mathbf{r})$, is obtained by solving the Poisson equation:

$$\nabla^2 V(\mathbf{r}) = -4\pi\rho(\mathbf{r}) \quad (3.13)$$

The solution of this equation is relevant in the context of electronic structure

calculations, where the potentials due to electronic and ionic densities, $\rho_{elec}(\mathbf{r})$ and $\rho_{ionic}(\mathbf{r})$, are required. Basically, from the charge density of the system, we calculate the potential and solve the Kohn-Sham equations. Solving Poisson's equation we obtain the Coulomb potential:

$$V(\mathbf{r}) = \int d\mathbf{r}' \frac{\rho(\mathbf{r}')}{|\mathbf{r} - \mathbf{r}'|} \quad (3.14)$$

where the integration is over all space. Under *periodic boundary conditions (PBCs)*, used for crystals, the potential corresponding to a given periodic charge density can be obtained by solving the equation in reciprocal space

$$\tilde{V}(\mathbf{G}) = 4\pi \frac{\tilde{\rho}(\mathbf{G})}{|\mathbf{G}|^2} \quad (3.15)$$

where $\tilde{V}(\mathbf{G})$ is the Fourier component of the potential in reciprocal-space and $\tilde{\rho}(\mathbf{G})$ is the corresponding Fourier transform of the charge density. This simple expression is of significant utility in electronic structure calculations for periodic system, where *Fast Fourier Transform (FFTs)* transform the quantities between real and reciprocal space efficiently. Just looking at the mathematical expression of Eq 3.15, we notice that there is a divergence for $\mathbf{G}_0 = 0$ which can only be avoided by setting the numerator to zero. For neutral systems, this condition is satisfied because $\rho_{elec}(\mathbf{r})$ and $\rho_{nuclei}(\mathbf{r})$ cancel each other. However, in the case of charged systems, as in the case where defects have an excess of charge, this is not the case. In practice, to avoid this problem, one introduces a compensating homogeneous background charge (jellium) $\langle n_0 \rangle$ Figure 3.9-(b) which is opposite in sign to the extra charge in the system, which guarantees that the overall charge in the periodic unit cell is neutral. The electrostatics requires thus to solve

$$\nabla^2 V(\mathbf{r}) = -4\pi \{\rho(\mathbf{r}) - \langle n_0 \rangle\} \quad (3.16)$$

where $\langle n_0 \rangle$ is the average charge density over the volume of the unit cell, Ω :

$$\langle n_0 \rangle = \frac{1}{\Omega} \int_{\Omega} d\mathbf{r} \rho(\mathbf{r}) \quad (3.17)$$

$$= q/\Omega \quad (3.18)$$

The subtraction of $\langle n_0 \rangle$ from the real-space charge density, $\rho(\mathbf{r})$, in Eq 3.16 is equivalent to setting $\tilde{\rho}(\mathbf{G}_0) = 0$, thus avoiding singularities in Eq 3.15. The elimination of the divergence at $\mathbf{G}_0 = 0$ by introduction of this new term, is equivalent to a change in the zero reference for the electrostatic potential. We will look back to this effect in the following sections. Now that it is clear how the electrostatic energies are calculated in *PBC*, we move on to describe how to define the formation of defects in two different scenarios: (i) neutral defects and (ii) charged defects.

3.2.2 Neutral Defect Formation

The calculation of defect formation energy, in the case of neutral defects can be written as [Dur+18]

$$E^f[X^{q=0}] = E_{tot}[X^{q=0}] - E_{tot}[pristine] - \sum_i n_i \mu_i \quad (3.19)$$

where $E_{tot}[X^{q=0}]$ is the total energy of the supercell with the neutral defect specie X and $E_{tot}[pristine]$ is the total energy of the perfect crystal supercell. The μ_i and n_i are the chemical potential and the number of atoms of the corresponding specie introduced (or removed) in the system. The μ_i allows us to define a reference to an external reservoir which can be used to estimate the stability of the defect under different chemical conditions. Essentially, atoms will find some more favorable regions energetically, with lower chemical potential during the growth. Therefore, the (negative) chemical potential gradient acts as a driving force for atoms to move into these regions. Also since the chemical potential is equivalent for all defects, the bulk and the environment are in equilibrium; this parameter gives a major advantage in building a theoretical understanding of the phase diagram.

3.2.3 Charged Defect Formation

As we mentioned before, when dealing with charged defects, the problem is more complex. Now, The formation energy is expressed as

$$E^f[X^q] = E_{tot}[X^q] - E_{tot}[pristine] - \sum_i n_i \mu_i + \underbrace{q\mu_e}_I + \underbrace{q\Delta V_{NAP}}_{II} + \underbrace{E_{corr}^q}_{III} \quad (3.20)$$

there are new terms in the second line that we describe one by one:

- (I) As the charge of the defect system no longer matches that of the neutral reference systems due to excess of charge, the formation energy requires to define the chemical potential for the electrons known as electrochemical potential μ_e as reference. This electrochemical potential holds the same concept as chemical potential, which means the energy cost for adding (or removing) species, in this case, an electrically charged particle. For "electrons" in metals this is nothing but the *Fermi level*, μ_F . In general, it is convenient to introduce a reference for the Fermi level, even when the system has a gap $\mu_e = \mu_F - \Delta\mu_F$. For slabs and clusters, μ_e is often set to the vacuum level. More frequently, the top of the valence band (VBM) or the minimum of the conduction band (CBM) in the bulk of the pristine crystal is used as a reference [Kah16]. Therefore, care must be taken to identify an appropriate reference for the electronic chemical potential when using periodic models to calculate formation energies for isolated charged defects. This brings the additional first term to the formation energy $q\mu_e$, where q is the defect charge state, and μ_e is the electron reservoir energy as mentioned. Here we choose to define the electronic chemical potential with respect to the top of the valence band, $\mu_e = [\mu_F + \epsilon_{VBM}]$.
- (II) As we discussed in Section 3.2.2, the $G_0 = 0$ Fourier component of the electrostatic potential (i.e. the average of the potential) is commonly taken to define the zero, thus avoiding the divergence coming from the interactions between periodic charges. [IZC79] For neutral defects both $E_{tot}[X^0]$ and $E_{tot}[pristine]$ in Eq 3.19 have thus the same common reference. However, for charged defects we have to use a homogeneous neutralizing background charge (jellium) to avoid the divergence. This changes the zero reference point for the potential, and thus the energies $E_{tot}[X^q]$ and $E_{tot}[pristine]$ are defined with respect to different references. When dealing with charged defect system, *neglecting the average potential (NAP)* introduces a numerical error in the formation energy of the charged defect. A potential alignment correction term $q\Delta V_{NAP}$ is often applied to account for this problem and recover the bulk-like reference also for the defective supercell.
- (III) The interaction between localized charges with the neutralizing back-

ground and periodic images is long-ranged and slowly converges for the supercell size L . The interaction energy coming from this Coulomb potential can be sizable, even in fairly large supercells. Thus, we have to add a correction term to Eq 3.19, E_{corr}^q , which will be defined soon E_{corr}^q .

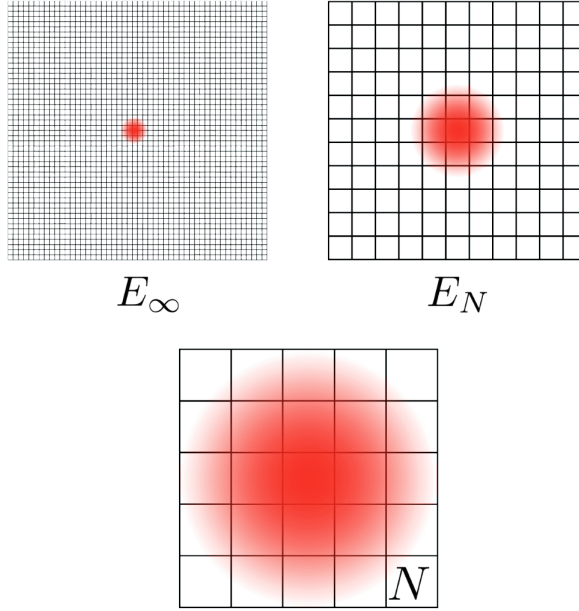


Figure 3.10: The scaling rule for Finite-Size Corrections. The fading red circle represents the interaction on the N scaled system. Increasing the cell (N) will reduce this interaction and essentially be zero in E_∞ .

The two terms E_{corr}^q and ΔV_{NAP} tend to zero as the size of the DFT simulation supercell increases. Several approaches have been proposed to avoid calculations with very large supercells. Most of these approaches are based on finite-size corrections. So if we consider N as the order of increasing the cell, we want to know how far we need to go to get those terms to be converged. What will be the remaining interaction in E_N if infinitely large supercell is used, $E_\infty \approx 0$? Basically, the E_N represents the energy required to remove these artificial interactions Figure 3.10. We will focus explicitly on calculating these two terms for the rest of

this chapter, but first, we describe the idea behind the finite-size scale corrections method in the next section.

3.2.4 Finite-Size Corrections

Assuming N is a parameter that defines the size of the simulation box (for example the number of unit cell repetitions that generate the supercell) we write the infinite system energy as

$$E_{\infty} = E_N + (E_{\infty} - E_N) \quad (3.21)$$

$$E_{\infty} \simeq E_N + (E_{\infty}^{\approx} - E_N^{\approx}) + F(N) \quad (3.22)$$

where E_{∞} and E_N are the energy of infinite and N -cell system. The essential idea behind finite-size correction formulae is to write the energy of the infinite system Eq 3.21 as an approximation ($E_{\infty}^{\approx} - E_N^{\approx}$) and extrapolation $F(N)$ with a much less expensive scheme Eq 3.22.

A series of calculations are performed for a range of system sizes to obtain E_N . The correction term in parenthesis is approximated using a much less expensive scheme, for example from a simple point charge model (Madelung), or using some localized model charges. Then the results are fitted to a chosen functional form that has the correct scaling with N , thus enabling an estimation of E_N . Typically, $(1/L + 1/L^3)$ is used for the scaling function $F(N)$. Basically, the $(E_{\infty}^{\approx} - E_N^{\approx})$ term is defined by one of the *a posteriori* approaches we will discuss in the following, which is also linked to a specific scaling behaviour.

3.2.5 Long Range Interactions in PBC & Finite-Size Corrections Terms for Charged Systems

As we mentioned earlier, the cell size must be sufficiently large to neglect the artificial interactions for neutral defects. The long-range Coulomb interaction between the localized charge distributions in periodic images converges slowly for charged defects. Consequently, the supercell sizes required to produce converged energies become prohibitively large, Figure 3.11. However, introducing corrections schemes we can improve the scaling laws with the system size, enabling a better extrapolation for moderate simulation boxes.

There are different *a posteriori* correction schemes,⁴ which are based on a

4 Recently (2021) Self-consistent potential correction for charged periodic systems has been

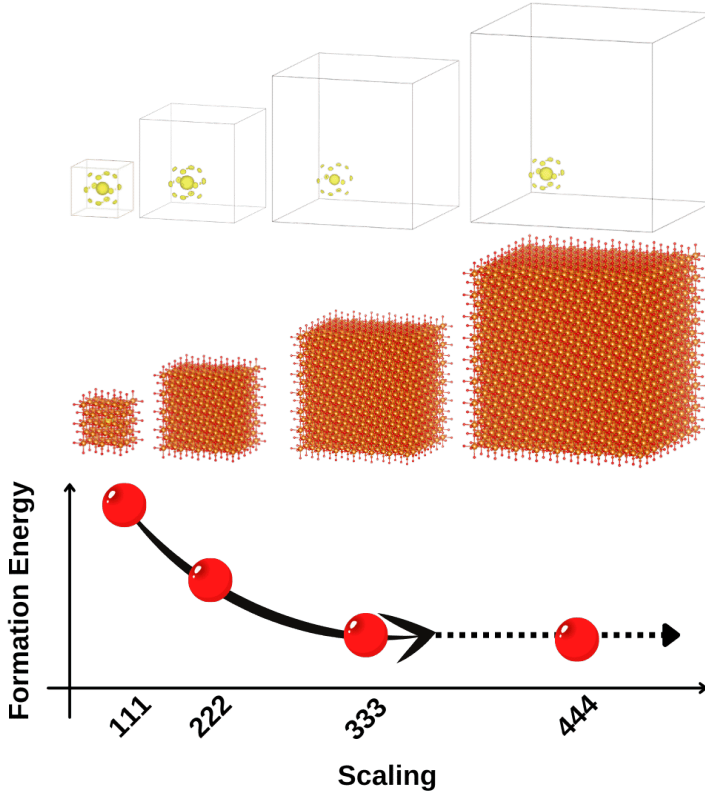


Figure 3.11: Illustration of the approach to converge the calculations for defects by increasing the simulation box. Top panel illustrates a localized defect charge within the box. Central panel is the actual supercell, which contains $N \times N \times N$ repetitions of the crystal unit cell and the point defect that gives the localized defect level. The scaling rule for charge defects convergence (lower panel) usually requires supercells with a large number of atoms, becoming prohibitively expensive computationally. For instance, crystals with a unit cell ($1 \times 1 \times 1$) containing eight atoms will become computationally challenging if the supercell required for converged defect energies becomes ($4 \times 4 \times 4$), which has a total of 512 atoms!. These cell sizes are not uncommon to have well converged results even with the best correction schemes available.

finite-size correction. Among the different corrections methods proposed in the literature we can mention:

introduced [Cha+21]. However, in this thesis, we aimed to focus exclusively on *a posteriori* methods

- 1995 Makov and Payne (MP) [MP94]
- 2008 Lany and Zunger (LZ) [LZ08]
- 2009 Freysoldt, Neugebauer, and Van de Walle (FNV) [FNW09]
- 2014 Kumagai-Oba (KO) [KO14]
- 2018 The Density Countercharge a Posteriori (DCCP) [Dur+18]

Makov and Payne (MP) Correction Method

The Markov-Payne (MP) Correction method uses the simplest electrostatic model that can be defined for this problem, which approximates the defect as a point charge (PC). The first-order Makov-Payne (MP) correction for a periodic array of charges is:

$$E_{corr} = \underbrace{\frac{q^2 \alpha_M}{2L\epsilon}}_{MP_I} \quad (3.23)$$

Where ϵ is the dielectric constant of the material containing the defect, L is the supercell size, which is equivalent to the separation between periodic images of the defect point charge, and α_M is the *Madelung constant*, which depends only on the shape of the supercell containing the defect and can be calculated for any Bravais lattice through the use of the Ewald method [Dab+08; WN04]. For example, for *Simple Cubic (SC)*, *Body-centered cubic (BCC)*, and *Face-centered cubic (FCC)* lattices, α_M assumes the value of 2.8373, 3.6392, and 4.5848, respectively [LG85]. The MP method provides the exact interaction energy of an array of point charges immersed in neutralizing jellium. The appropriate dielectric constant is the static dielectric constant ϵ_0 when ionic relaxation of the defect is considered or the high-frequency dielectric constant ϵ_∞ when the ionic structure is kept fixed to the pristine crystal structure. This simple method has been extended to general supercell shapes and anisotropic dielectrics [MH13]. However, the charge distribution of a charged point defect such as a vacancy cannot really be considered as a point charge, as it extends over a certain spatial region, which is dependent on the characteristics of the defect, due to dangling bonds and their interactions with neighboring ions. The model correction based on a point charge is a highly idealized model, which is known to overestimate the strength

of the image interactions [FNW09]. Makov and Payne also suggested using multipole expansion to generate higher-order terms to take care of interactions between the point charge and possible quadrupoles Q created by the defect charge:

$$E_{corr} = \underbrace{\frac{q^2 \alpha_M}{2L\epsilon}}_{MP_I} + \underbrace{\frac{2\pi q Q}{3L^3 \epsilon}}_{MP_{II}} + O(L^{-5}) \quad (3.24)$$

Here Q is the Quadrupole (second radial) moment of the defect charge model

$$Q = \int r^2 \rho_c(\mathbf{r}) d\mathbf{r} \quad (3.25)$$

However, the MP method does not provide any systematic way of calculating Q , so this quadrupole term is rarely considered within the MP method. Obviously, when the defect charge distribution cannot be considered as a point charge, the MP expansion Eq 3.24 is no longer valid. In fact, in the limit of an entirely delocalized charge, the interaction between image charges is completely canceled because of the compensation due to the background charge. There is no need to emphasize that another concern of this method is the dependence of the Madelung parameter α_M to the shape of the crystal cell.

Lany and Zunger (LZ) Correction Method

The Lany-Zunger (LZ) correction method [LZ08; LZ09], focuses directly on the problem of calculating the second term on MP (Eq 3.24), by making a practical approximation to Q . When defects are introduced in solids the defect-induced charge density is defined as

$$\Delta\rho_{\text{defect}} = \rho_q - \rho_p \quad (3.26)$$

Here ρ_q is the charge density of the system with the defect, and ρ_p is the charge density of the crystal host without any defect. This $\Delta\rho_{\text{defect}}$ should be replaced in Eq 3.25 instead of ρ_c . With this model the two terms for the total energy correction in Eq 3.24 can be computed. LZ demonstrated that Q is actually dominated by contribution to $\Delta\rho_{\text{defect}}$ emerging from the screening response upon introducing a charged defect into the host Figure 3.12. After including the

interaction energy between screened point-charge into the screened potential, the point-quadrupole interactions, which accounts for $1/L^3$ scaling, can be neglected and the potential alignment correction does the scaling of $1/L^3$.

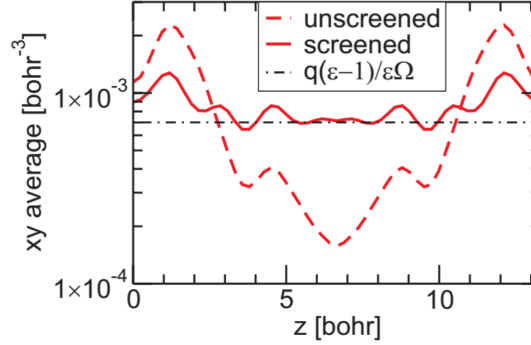


Figure 3.12: The Comparison of defect charges before and after screening for the V_c'' in diamond in a 64-atom supercell. The defect is located at $z = 0$ with a periodic image at $z = 13.3$ bohr. The limit of a homogeneously distributed screening charge is indicated by the black dash-dotted line. (Figure is taken from [FNV11]).

Using the charge difference obtained directly from the total charge densities between the charged defect supercell $\rho_q(\mathbf{r})$ and pristine (host) $\rho_p(\mathbf{r})$ *DFT* calculations $\rho_c(\mathbf{r}) = \rho_q(\mathbf{r}) - \rho_p(\mathbf{r})$ in the Eq 3.25, they calculated the second radial moment MP_{II} in Eq 3.24. They found a proportionality between both MP_I and MP_{II} :

$$E_{MP_{II}} = c_{sh} E_{MP_I} \quad (3.27)$$

where c_{sh} depends only on the shape of the supercell again [LZ09]. For a cubic cell, $\pi/3\alpha \approx -0.369$. Combining with the MP_I term

$$E_{corr}^{LZ} = \left[1 + c_{sh} \left(1 - \frac{1}{\epsilon} \right) \right] \frac{q^2 \alpha_M}{2\epsilon L} \quad (3.28)$$

Of course, more accurate evaluations require the calculation of c_{sh} for the adopted cell shape [LZ09]. Ultimately, using the *DFT* charge density difference leads to some difficulties where we need to use shape-dependent parameter c_{sh} . The correction formulation relies only on $1/L^{-1}$, not $1/L^{-3}$, and it is not clear how

to treat the higher-order terms in the expansion. Furthermore, defect charge distribution must be well localized for this approximation to be valid.

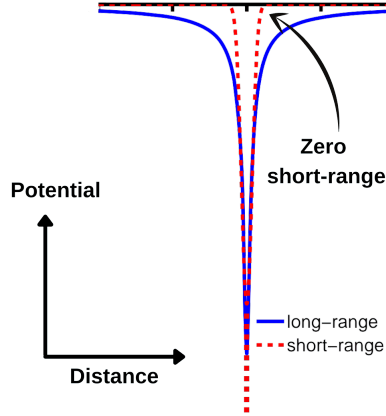


Figure 3.13: The long and short-range Coulomb potential profile where short-range fall very fast to zero with respect to the long-range . (Figure is taken and modified from [Hua+10]).

Freysoldt, Neugebauer, and Van de Walle (FNV) Correction Method

The approach by Freysoldt, Neugebauer, and Van de Walle [FNW09] combines a Gaussian charge distribution to model the charge, along with the *DFT* potential to obtain explicitly an improved model of the electrostatics. They divided the single defect interactions with its periodic images into two parts, one to account for long range interactions, and one for the short-range contribution Figure 3.13

$$V_{\text{defect}}(\mathbf{r}) = V^{\text{long-range}}(\mathbf{r}) + V^{\text{short-range}}(\mathbf{r}) \quad (3.29)$$

The long-range contribution is given by a Gaussian distribution charge model $q^{\text{model}}(\mathbf{r}')$,

$$V^{\text{long-range}}(\mathbf{r}) \simeq V^{\text{model}}(\mathbf{r}) = \int d^3\mathbf{r}' \frac{q^{\text{model}}(\mathbf{r}')}{\epsilon|\mathbf{r} - \mathbf{r}'|} \quad (3.30)$$

and the short-range will fall to zero much faster then long-range.

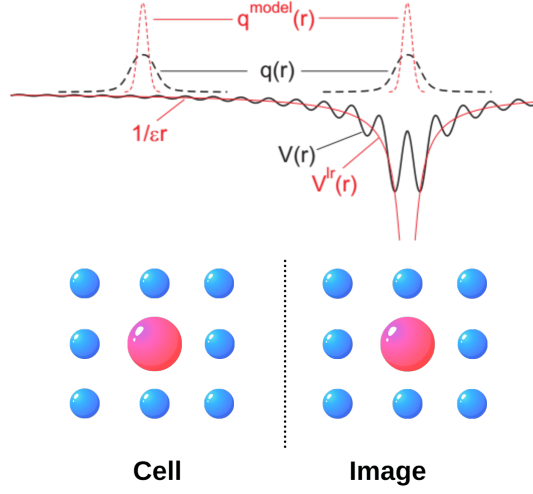


Figure 3.14: The schematic diagram for charge defect Model potential defect-defect interactions in *PBC*, q^{model} is the charge model for representing the localized defect charge, $V(r)$ is *DFT* potential, and V^{lr} represents the long-range interactions with periodic defect image after the screening of material. (Figure is taken and modified from [FNV11]).

The the periodic repetition of the long-range interaction, results in a “lattice energy”, E_{lat} which can be estimated from the screened lattice energy (Madelung energy) or solving Poisson in *PBC* with the *FFT* (Eq 3.15) of the model charge. They assume the short-range potential is essentially zero outside big enough supercell and the interaction comes from long-range as shown in Figure 3.14. Finally, the correction is given as the sum of interaction energy of the defect charge model used, and the alignment term:

$$E_{\text{corr}}^{\text{FNV}} = E_{\text{lat}} - q\Delta V_{\text{NAP}} \quad (3.31)$$

The potential alignment term ΔV_{NAP} is obtained by comparing the potential from the model charge to the difference of the *DFT* potentials between the pristine crystal, $V_{\text{p}}^{\text{DFT}}$, and the charged defect system $V_{\text{q}}^{\text{DFT}}$:

$$\Delta V_{\text{NAP}} \approx \Delta V_{\text{q/p}} = \left(V_{\text{q}}^{\text{DFT}} - V_{\text{p}}^{\text{DFT}} \right) \Big|_{\text{far}} - V^{\text{model}} \Big|_{\text{far}} \quad (3.32)$$

The alignment of these potentials has to be done sufficiently far from the defect position. In this method, different shapes of charge models give different E_{lat} . Nevertheless, the FNV scheme yields corrected formation energies independent of the adopted charge model due to scaling. However, it requires the defect charge to be well localized within the simulation cell so that it represents correct long and short-range interactions.

The FNV scheme defines a general framework for calculating energy corrections for defects in supercells. The method has also been extended to treat surfaces and interfaces [KP13]. However, there are two main limitations for this

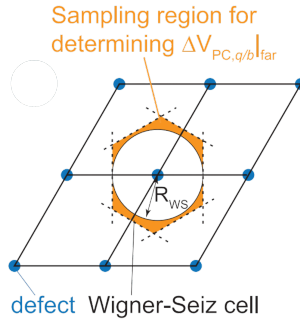


Figure 3.15: The Alignment approach in the KO correction method where average $V_{NAP,q/p}$ is taken at the atomic positions in the region outside of the sphere that is in contact with the Wigner-Seiz cell with radius R_{WS} . [Adapted from “Electrostatics-based finite-size corrections for first-principles point defect calculations,” by Yu Kumagai et al. [KO14]]

method, (i) the alignment term can be problematic when the atomic relaxations are included in the potential because it can be difficult to define a region far from the defect that resembles the potential in the pristine system, and (ii) defining the model charge becomes problematic when the defect charge distribution is spread throughout the whole simulation cell. Furthermore, the atomic relaxations can give charge distributions that cannot be described with a simple Gaussian shape.

Kumagai-Oba (KO) Correction Method

In the cases where atomic relaxations are considered, the displacement of the ions can introduce long-range interactions that decay slowly. This can be understood by considering that the atomic relaxation can modify the characteristics of

charged defects and give dipole and higher-order terms for electrostatic interactions that have different decay lengths at long distances. The Kumagai-Oba (KO) method addresses this issue [KO14]. They include the long-range interaction inside the alignment term. They propose to take the average potential $V_{NAP,q/p}$ around the vicinity of atomic positions in the region outside of the sphere that is in contact with the Wigner-Seiz cell with radius R_{WS} instead of $\Delta V_{NAP,q/p}|_{far}$ as illustrated in Figure 3.15.

The Density Countercharge a posteriori (DCCP) Correction Method

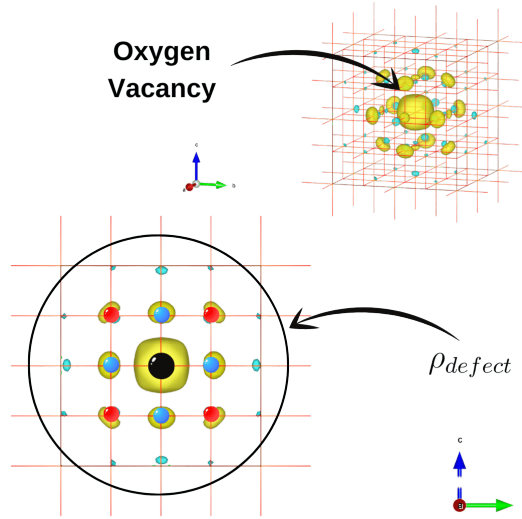


Figure 3.16: The V_O^\bullet defect charge in MgO calculated from *DFT* as in Eq 3.35. The Mg and O ions denoted by blue and red dots, respectively. The black dot show the position of the oxygen vacancy.

The DCCP is similar to the density countercharge (DCC) method of Dabo et al. [Dab+08], where an explicit charge distribution model of the charge due to the defect and a complete electrostatic model system correction is defined. The correction is applied to each *SCF* step within the *DFT* calculation. However in the DCCP method, the correction is applied only at the end of the calculation. So it is considered a *a posteriori* application of the DCC method. In the DCCP, the

spurious interaction with images is defined as

$$E_{corr} = \frac{1}{2} \int \rho(\mathbf{r}) V_{corr}(\mathbf{r}) \quad (3.33)$$

where this correction potential contains two contributions

$$V_{corr}(\mathbf{r}) = V_{isolated}(\mathbf{r}) - V_{PBC}(\mathbf{r}) \quad (3.34)$$

$V_{isolated}(\mathbf{r})$ comes from the isolated system in the absence of other image charges, and $V_{PBC}(\mathbf{r})$ is the interaction of the charge surrounded by its periodic images. The charge distribution of Eq 3.33 comes directly from the *DFT* calculation

$$\rho_{defect}(\mathbf{r}) = \rho_q(\mathbf{r}) - \rho_{nd}(\mathbf{r}) \quad (3.35)$$

Where the $\rho_q(\mathbf{r})$ is the *DFT* charge in a relaxed structure of charge defect and $\rho_{nd}(\mathbf{r})$ is the *DFT* charge distribution obtained for a neutral defect system computed with the structure of the relaxed charged defect (we call this the *neutralized defect*). For the alignment potential term we can decompose the contribution in three intermediate steps, as shown in Figure 3.17:

$$\Delta_{q/p}(\mathbf{r}) = \Delta_{AB}(\mathbf{r}) + \Delta_{BC}(\mathbf{r}) + \Delta_{CD}(\mathbf{r}) \quad (3.36)$$

Where $\Delta_{AB}(\mathbf{r})$ is the difference of potential going from pristine to the defect crystal without any atomic relaxation, $\Delta_{BC}(\mathbf{r})$ is the potential difference in defected crystal going from unrelaxed to the relaxed structure. Finally, the $\Delta_{CD}(\mathbf{r})$ is the potential difference from the relaxed charged defect structure to the neutral defect keeping the relaxed structure fixed (neutralized case as discussed earlier). In principle, far from the defect, the potential should be aligned to the bulk potential. Durrant *et al.* discuss each different component of alignment in Eq 3.36, and they claim that the most important contribution is usually coming from the AB part. [Dur+18]

Our Approach

In FNV, the essential idea is to capture defect-induced long-range interactions with a simplified charge model and to correct for the short-range interactions consistently. However, different charge models give different long-range interac-

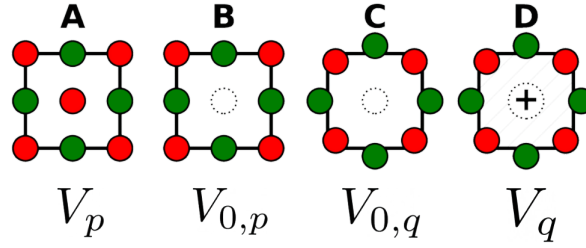


Figure 3.17: The alignment approach in the DCCP correction method has four components. Each sketch in the figure denotes a *DFT* single calculation. A is the host material without any defects. D corresponds to the relaxed structure of a charged defect introduced in the host crystal. This charged defect can be a vacancy, impurity, or interstitial with a corresponding charge state. Two intermediate steps can be defined: In B, the same defect in its neutral state (no extra charges in the box) is introduced in the pristine system without any ionic relaxation. Similarly, C is also a neutral system but this time taking the relaxed geometry of D (also called *neutralized defect*). [Adapted from “Relation between image charge and potential alignment corrections for charged defects in periodic boundary conditions,” by T.R.Durrant et al. [Dur+18]]

tions. Nevertheless, the FNV scheme can correct formation energies independent of the adopted charge model as long as the long-range term can capture the periodic image interactions and the short-range interactions decay to zero within the supercell. In the DCCP method, one uses the DFT charge density ρ_{defect} to calculate the interactions between defect images and the alignment is achieved by decomposing potentials in different parts, and there is no systematic way to find which component gives the converged value. Here, we calculate ρ_{defect} as the DCCP method. Then, we calculate the long-range (periodic) interaction $V^{\text{long-range}}$ coming from this charge model. This is done solving the Poisson equation with the dielectric constant of the material, ϵ , to include screening effects. We use finite scaling with $1/L$ dependence to find the E_{corr} . These steps allow having a general method which does not depend on any external parameter such as c_{sh} , or the Madelung constant, or the broadening parameter for the Gaussian model. Finally, for the alignment term, we use a value of the planar average of the potentials far from defect as follows:

$$\Delta V_{NAP} \approx \Delta V_{q/p}|_{\text{far}} = (V_q - V_p)|_{\text{far}} \quad (3.37)$$

$$(3.38)$$

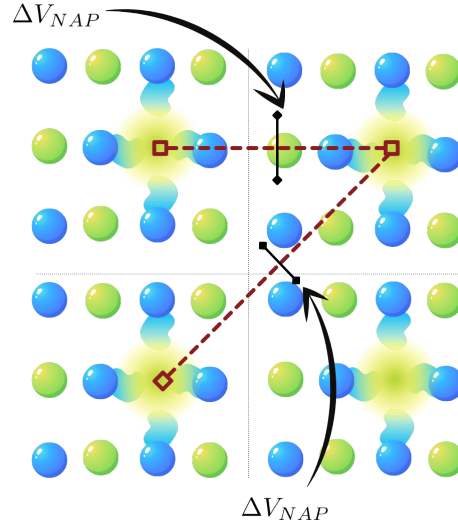


Figure 3.18: In our approach, potential alignment is done with $\Delta V_{p/q}$ defined from the difference between the planar averaged potentials for the pristine and relaxed charge defects. Dashed lines represent different directions between periodic defect images that define the normal to the plane where the average of the potential is computed, and the perpendicular solid black line represents the mid point regions which are taken to define $|_{\text{far}}$.

where $\Delta V_{q/p}$ is the difference between the potentials for the pristine crystal (V_p) and the charged defect in its relaxed geometry (V_q). Here, the " $|_{\text{far}}$ " is defined as the intermediate distance between periodic images of the defect, and the user can choose which planes (or directions) are taken for computing the average potentials as shown in Figure 3.2.5.

3.2.6 Charge Defect Formation Phase Stability Diagram

Here our interest is on point defects, and their charge states, which depend on the chemical potential of the constituent species (atoms and electrons), as discussed in Eq 3.20. When studying defect formation energies it is common to represent the energy as a function of these chemical potentials, μ_i as it allows to correlate the stability of defects on the chemical environment. The electron chemical potential (or the Fermi energy) can also be taken as a free parameter

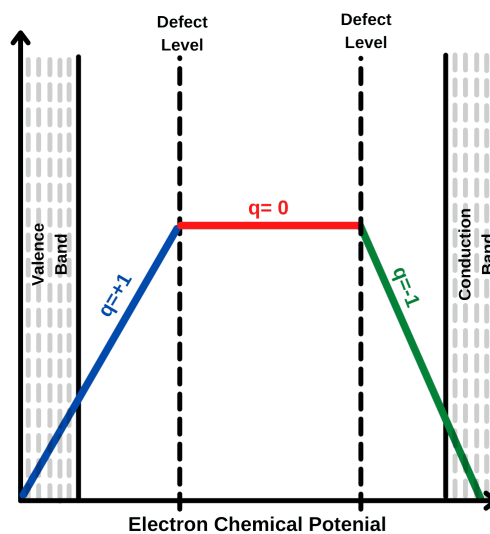


Figure 3.19: The point defects formation vs. Electron chemical potential known as charged defect stability diagram. A positive slope corresponds to a positively charged defect, while a negative slope corresponds to a negatively charged defect configuration. Neutral defects are independent on the electronic chemical potential. Depending on what is the position of the Fermi level, different charge states for the defect can be stabilized. In the figure, a Fermi level close to the conduction band will stabilize negatively charge defects, while Fermi levels close to the valence band stabilize positively charged defects. The crossings between curves with different slopes are linked to the position of a defect level that can be populated/depopulated.

that could be used to define which charge state configuration is more stable. If a large number of extra electrons are available in a semiconductor, the Fermi level would be closer to the conduction band and the possible defect levels within the gap would be populated. If, however, electrons are removed or scarce, the Fermi level will be closer to the top of the valence band, and defect levels in the gap will be depopulated. Here we call *Charged Defect Stability Diagram* to the plots of the defect formation energies as a function of the electronic chemical potential, as shown in Figure 3.19. These plots contain information of the stability of the different charge states of the defect and the energy of defect levels within the gap.

3.3 Implementation of Sisl ToolBox Siesta Defects and AiiDA Siesta Defects

As we witnessed from the discussion of the charge defect formation, its calculation required some automation and has different terms as shown in Figure 3.20. I developed two separate packages to take care of defect correction methods and their calculation automation:

- **Sisl ToolBox Siesta defects:** is a python package tool inside the Sisl toolbox to correct charge defect formation energy. To see the manual one could access to web page :

<http://zerothi.github.io/sisl/docs/latest/index.html>

- **AiiDA Siesta Defects :** is a python package to automate calculations of defective system with siesta through the AiiDA platform. To have access to the workflows and manual one could reach to web page :

<https://github.com/arsalan-akhtar/aiida-defects/tree/siesta-dev>

The motivation behind two separate packages is that we want to keep the freedom of choice for the users since some of them don't want to do high-throughput calculations so we provide them a standalone python package in sisl to allow them to correct their desired method for formation energy correction.

In the following chapter, we will use the implemented package to calculate and test the corrections for vacancy point defects on MgO, GaAs, HfO₂, and Diamond.

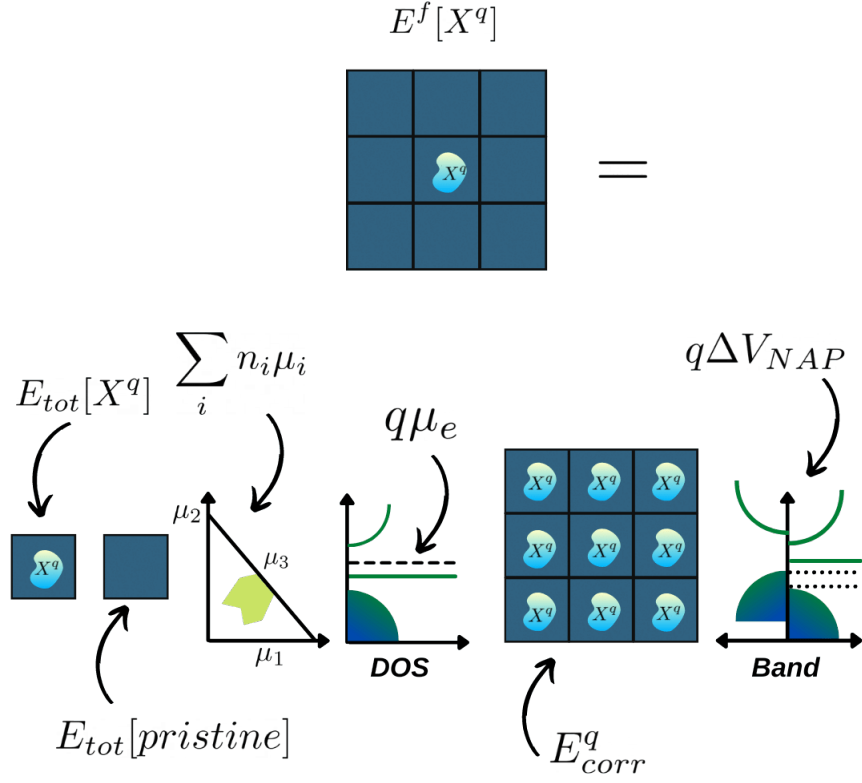


Figure 3.20: Schematic diagram of different terms in formation energy of charged defects. $E_{tot}[X^q]$ is the DFT energy of the supercell containing a defect of X with a charge state of q , $E_{tot}[pristine]$ is the DFT energy of the pristine supercell, $\sum_i n_i \mu_i$ is the energy cost of introducing n_i species with chemical potential μ_i and can be used to take into account the chemical environment and the growth conditions, $q\mu_e$ is the electronic potential for the electron reservoir, the E_{corr}^q accounts for spurious localized charge defect interactions with PBC and finally $q\Delta V_{NAP}$ aligns the potential to have the same references for pristine and defective system.

4

Defects Formation Energies: Applications

4.1 Defects and Charged Defects in Materials

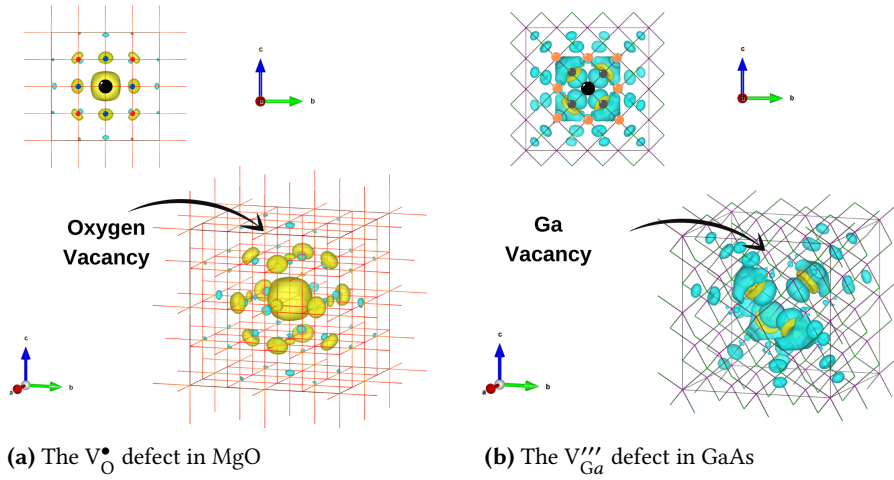


Figure 4.1: DFT calculated Defect charge distribution ρ_{defect} from difference of $\rho_q - \rho_{nd}$ as in Eq 3.35 for (a) V_O^\bullet in MgO the Mg and O ions denoted by blue and red dots, respectively and (b) $V_{Ga}^{''''}$ in GaAs, the Ga and As ions denoted by orange and gray dots, respectively. The black dots show the position of the respective vacancies in both cases.

Removing species from a crystal leaves a vacancy, and depending on the number of electrons in the system and the nature of the species, the vacancy site can host charges (charged defect) or not (neutral defect). Let us suppose the defect is charged. Usually, this extra charge is localized around the vacancy. However, as discussed in the previous chapter, this extra charge interacts with the periodic images, giving an artificial contribution to the computed electronic properties. We can use different approaches to correct these spurious interactions and calculate the formation energy of this kind of defects. In this chapter we

show how our tools can be used to calculate the formation energies of different charged vacancy types in different systems.

The degree of localization of the defect's charge distribution depends on two things: (i) the type of defected species and (ii) amount of charge around the defect in the particular host crystal. For example, in MgO, the oxygen vacancy has a well-localized s-like electronic defect state, as shown in Figure 4.1-(a). Due to oxygen's oxidation state of -2 in this material, the vacancy can be filled by 2, 1 or 0 electrons, leading respectively to V_O , V_O^\bullet , or $V_O^{\bullet\bullet}$ defect configurations, which are also known as color centers and labeled as F^0 , F^+ , and F^{2+} . On the other hand, the Ga vacancy (V_{Ga}) in GaAs has a localized defect state with extended tails which have sp^3 orbital shape. In contrast with the V_O defect in MgO, the V_{Ga} defect gives a charge cloud distribution that cannot be correctly described with a Gaussian charge model. In this chapter, we will show "how" the use of DFT charge ρ_{defect} from Eq 3.35 to calculate the E_{corr} , converges the formation energy correctly. We will study four different scenarios, starting from the simple ionic system (MgO) with a well localized defect level at V_O , and continuing with more delocalized vacancies in GaAs and diamond (which is as an example of a covalent system). Finally, we will focus on oxygen vacancies in HfO_2 as a system that stresses the importance of structural relaxations induced by defect.

One important technicality of the SIESTA code is that when we create a vacancy by removing the atom from the system, we also remove its atomic orbitals from the basis set. Thus, the basis set of the defective system is different to the basis set of the pristine system and this can affect the energetics under investigation. Conceptually this is similar to the problem of absorption energies of molecules on surfaces, which is typically known as the *Basis Set Superposition Error (BSSE)*. But the problem now is not just restricted to the comparison of the energies of the pristine versus defective system with different basis. It goes beyond, to the fundamental description of the electronic states of the vacancy, i.e. whether or not the standard basis set is enough to describe the localized electronic levels when the orbitals are removed from the vacant site. This will be addressed in the next subsection.

4.1.1 Importance of *Ghost* (or floating) orbitals

Although strictly localized atomic orbitals are advantageous for computational efficiency, they come with an unfavorable side which is that they might fail to describe electronic states that extend into regions where there are no sup-

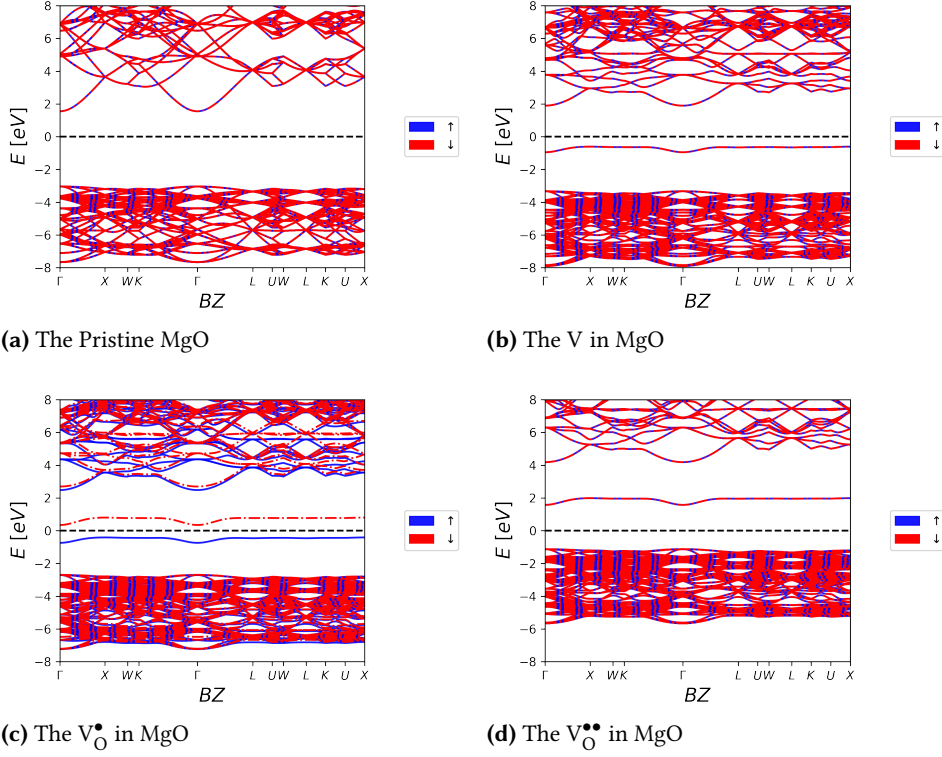


Figure 4.2: The Spin polarised electronic band structure of Oxygen neutral and positively charge defects in MgO along a high symmetry path in the Brillouin Zone. The Fermi energy is shifted to zero for all bands; this is due to taking the reference of it from the valence band maximum of the pristine as we discussed in chapter 3. (a) The pristine MgO with a clear gap of ≈ 5 eV (experimental = 7.8 eV). (b) The V_O in MgO with a doubly generated state in the gap, which is populated by two electrons. (c) The V_O^\bullet in MgO with only one spin state populated (d) The $V_O^{\bullet\bullet}$ in MgO with completely depopulated state in the gap.

port orbitals. Known examples are the surfaces of noble metals, [Gar+09b] or low-dimensional systems such as graphene or carbon nanotubes, where the image-potential states extend well into vacuum. [Sil+09] Another example is the formation of vacancies, where atoms (and their corresponding orbitals) are removed from the lattice, reducing the quality of the basis set. The description of

possible localized electronic states linked to the defect is then completely relying on the surrounding orbitals, which should be long enough to extend into the vacant site. Hence, a compromise between long cutoff radii, able to give a proper description of the electronic states, and short orbitals for optimal computation is required.

This section aims to provide a general framework to extract formation energies for vacancies using strictly localized basis sets that can accurately describe the electronic properties of these point defects. Our model system is the widely studied oxygen vacancy defect (V_O) in MgO, also known as the F center, which gives rise to a well-localized electronic level in the gap and can hold up to two electrons [MD11]. In the neutral system F^0 , formed by removing the O nucleus with its 8 electrons, the defect level is fully occupied Figure 4.2-(b). Removing one or two electrons from the system (F^+ -center Figure 4.2-(c) and F^{2+} -center Figure 4.2-(d) respectively), results in charged simulation cells, which require a compensating jellium [MP94] and corresponding energy correction schemes as discussed in previous chapter 3. Obviously, the three defects have different electronic (and structural) properties, and the description of the electronic defect state is critical. To describe the electronic structure around the vacancy we consider three different approximations:

- i) when the atom is removed to form the vacancy we also remove its orbitals from the basis set (this is referred as "no *ghost*" basis in the following);
- ii) the orbitals of the removed atom are kept as *ghost* orbitals in the basis.
- iii) the orbitals of the atom that is removed are also removed, but the cutoff radii for the orbitals surrounding the vacancy is increased so that the basis has a better coverage of the empty site;

The effect of *ghost* orbitals on the Charge distribution of Defect

First, we compare the total energy and defect charge distribution ρ_{defect} of a neutral system using different basis types. Using the *ghost*, and without any relaxation, the energy is 0.56 eV lower with respect to no *ghost*, which is due to a better description of the system. Lowering the energy by improving the quality of the basis set (i.e. adding the *ghost* orbitals) is in line with the expected behaviour behind the variational principle method. In Figure 4.3 we plot the charge distribution ρ_{defect} around the vacancy to illustrate the effect of the *ghost*

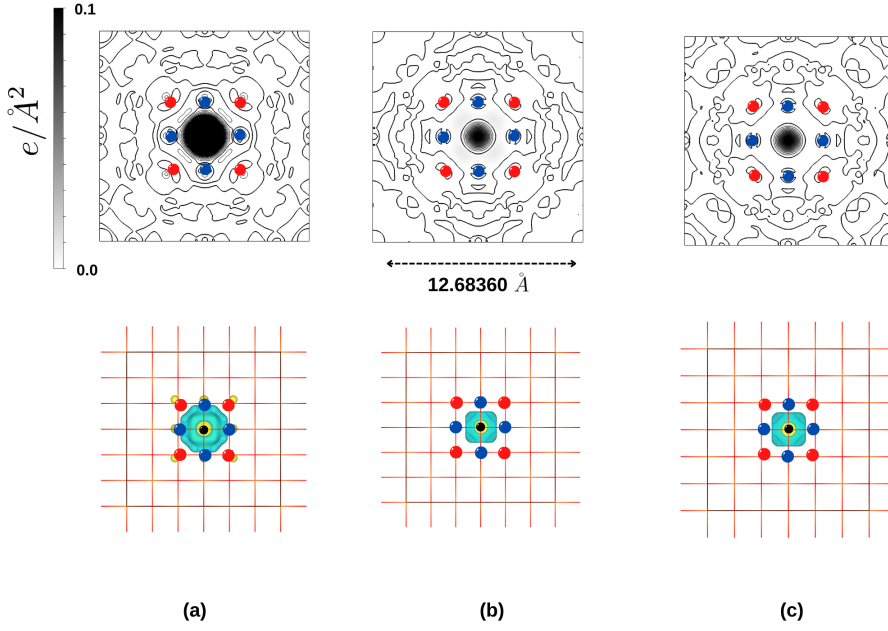


Figure 4.3: Contour plots with the charge redistribution around the neutral oxygen vacancy (V_O). Left panel shows $\rho_{\text{pristine}} - \rho_{\text{defect}}$ with *ghost* orbital in the basis and the unrelaxed structure. Central panel plots the difference between the densities obtained with *ghost* and without *ghost*, in the unrelaxed structure. Right panel is equivalent to central panel, but for the relaxed geometry obtained with the *ghost*. The Mg and O atoms positions are shown as blue and red circles, and the black dot corresponds to the position of the vacancy. Bottom panel shows an isosurface corresponding to a density of $0.005 e/\text{\AA}^3$.

orbitals. We show (i) the difference between the *DFT* charge distribution in the pristine system, ρ_{pristine} , and the charge for the system with the defect ρ_0 , but also (ii) the difference of the defect with *ghost* and the same defect without *ghost* in the unrelaxed geometry, and (iii) in the relaxed structure obtained with the *ghost*. The former gives an idea of where is the defect charge, while the later (central and right panels) illustrate the effect of the *ghost* itself. In the unrelaxed structure (left panel) we see that the charge is well localized around the vacancy. The difference between *ghost* and “no *ghost*” calculations shows that a much better localization of the charge around the defect position is obtained when

the *ghost* orbitals are included (dark sphere in the center of the image). The effect of lattice relaxation is minor in this particular case, and indeed the energy gain in the optimized geometry is below 10 meV. As we will see later, structural relaxation is significantly stronger for the charged vacancies.

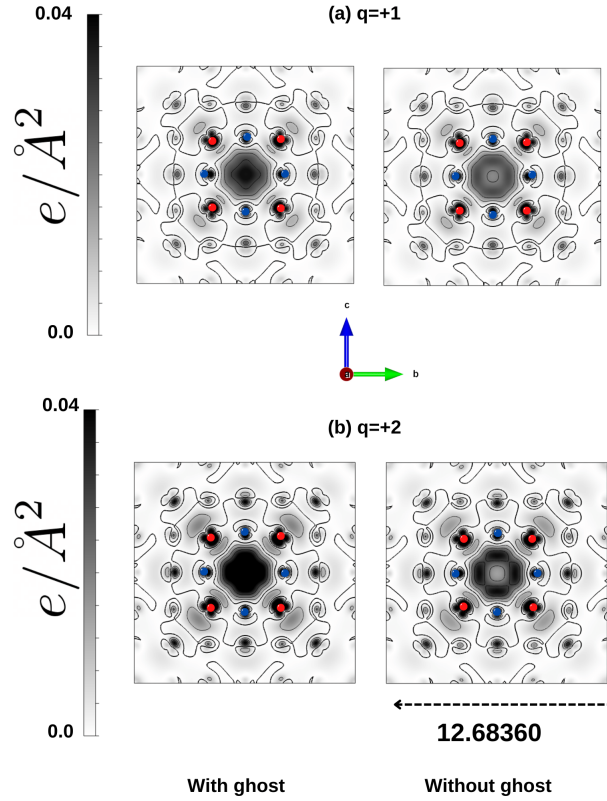


Figure 4.4: Electronic charge distribution after relaxation for different charge states (a) $V_O^{\bullet\bullet}$ (b) V_O^\bullet . Left panel shows results obtained with *ghost* orbitals, while right panels correspond to calculations run without *ghost*. Notice the hollow region (light grey) in the system without *ghost*. The charge density is defined as in Eq 3.35 (difference between the charged and the *neutralized* defect calculations) and plotted over the (100) plane that contains the vacancy site. Blue and red dots correspond respectively to the Mg and O atoms surrounding the oxygen vacancy.

It is important to remark that for charged defects, V_O^\bullet and $V_O^{\bullet\bullet}$, the energy correction scheme relies on a defect charge density calculated from Eq 3.35. In this case, the *ghost* orbitals are required to properly describe the charge distribution around the defect, as can be seen in Figure 4.4 where a hollow region is clearly visible in the position of the vacancy when the *ghost* is not included (light gray area in the center of the images). Critically, the different charge distributions obtained with different basis give rise to slightly different atomic relaxations (Table 4.1), which has consequences on the computed energy of the defect, and on the different corrections to the formation energy of the charged defects, as we will discuss later.

Table 4.1: Structural properties around the vacancy in different charge states, with *ghost* and without *ghost* in the orbital basis set. The interatomic distances between Mg atoms first-neighbors to V_O , and the next Mg-O bonds are shown. The percentage shows the variation with respect to the distances in the pristine system.

Distance (Å)	V_O		V_O^\bullet		$V_O^{\bullet\bullet}$	
	<i>ghost</i>	w/o	<i>ghost</i>	w/o	<i>ghost</i>	w/o
Mg–Mg	4.24	4.20	4.41	4.37	4.59	4.60
	0.2%	-0.7%	4.2%	3.4%	8.6%	8.7%
Mg–O	2.11	2.13	2.04	2.05	1.97	1.97
	-0.2%	0.6%	-3.7%	-3.2%	-6.7%	-6.8%

The effect of *ghost* orbitals on the electronic structure

The Projected Density of States (PDOS) over the basis orbitals of interest are plotted in Figure 4.5 for the V_O (neutral) defect configuration. The presence of the defect level in the gap (occupied for the neutral defect state) is reproduced whether the *ghost* orbitals are included or not, as long as the cutoff radii of the surrounding orbitals around the vacancy are large enough. However, as we saw above, the localization of the charge is slightly different, resulting in slightly different structural features, as we discussed. The next neighbor Mg 3s orbitals, and to less extend the 2p orbitals pointing towards the vacancy site, contribute to describe the defect level with a bonding character which tends to decrease the surrounding Mg-Mg interatomic distances. However, when the *ghost* orbitals are included, the defect level is mostly described with their *s* character, resulting in a more localized defect state and slightly increased Mg-Mg distances. The

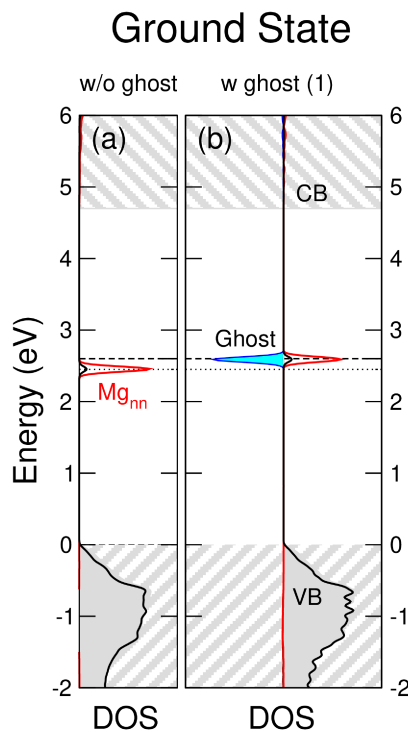


Figure 4.5: Projected Density of States around the electronic gap showing the defect level due to V_O . Panels (a) and (b) correspond to the Ground State defect configuration. The valence and conduction bands are shown as striped grey areas, and the energy is aligned to the top of the valence band. Dashed horizontal lines are guidelines to the defect level position. The projection on bulk Mg and O orbitals (far from the defect) are black and dark grey shaded areas, respectively. Black thick line corresponds to oxygen atoms that are close to the defect (O_{nn}), while red line is used for Mg next neighbors to V_O . The projection onto the *ghost* orbitals is plotted as shaded cyan regions in panels (b).

different localization of the defect level is evident in any charge partitioning scheme, such as Mulliken, Voronoi, or Hirshfeld populations, with larger charges spread over the first neighbors shells around the vacancy when *ghost* orbitals are not included in the basis set, and more charge localized on the *ghosts* when

they are added to the basis. Interestingly, when the defect is depopulated, there is an expansion of the vacancy region which can be measured from the Mg-Mg interatomic distances (Table 4.1). This can be rationalized from the bonding character of the defect level, which favors a decrease in the Mg-Mg distance of surrounding atoms when occupied, and the consequent expansion when depopulated.

The effect of *ghost* orbitals on the Energetics

Table 4.2: Calculated formation energies for the different charge states

V_O^q	V_O	V_O^\bullet	$V_O^{\bullet\bullet}$
	$E_f^{q=0}$ [eV]	$E_f^{q=+1}$ [eV]	$E_f^{q=+2}$ [eV]
With Ghost	9.59	6.92	5.03
Without Ghost	10.19	7.58	5.25
Longer Mg Basis	9.07	6.56	5.05
Others (PW) PBEsol [Dur+18]	10.27	7.78	6.19
Others (NAO) GGA [Ric13]	7.09	-	-

We calculate the formation energy for the different basis sets and present the results in Table 4.2. As expected, the formation energy is sensitive to the basis set used. We expect overestimated formation energy when we do not use the *ghost*. As we saw, the use of the *ghost* orbital improves the description of the defect state and decreases the defect formation energy by ~ 0.5 eV in better agreement with the experimental value (9.29 eV) reported by Kappers *et al.* [KKH70] for the neutral vacancy. Comparison with other calculations is tricky, as it has been shown that the formation energies are very sensitive to the exchange-correlation used, with variations of up to a 0.5 eV depending on the numerical method used even with the same functional. [Ric13] Nevertheless, in the table we show the results from Durrant and collaborators [Dur+18] as reference. For the positively charged defects (V_O^\bullet and $V_O^{\bullet\bullet}$), the electronic defect level is either partially or fully depopulated, and its localization determines the model charge density

(typically a gaussian) required to account for the long-range electrostatic energy correction as we discussed previously in chapter 3. For $V_O^{\bullet\bullet}$ the energetics, and the structural properties obtained with *ghost* and without *ghost* orbitals in the basis are essentially equivalent (as there is no charge localized at the defect, the need for *ghost* is not critical).

Having discussed the need for a good basis set to have an accurate description of the defect level, we move on to analyze the correction schemes used to compute $E_f[X^q]$ (Eq 3.20).

4.2 Charged Defects: The case where the charge is *well-behaved* (localized & spherical)

As a first case to illustrate the methods developed in chapter 3, we will continue with oxygen vacancies in MgO, where the defect level is well localized, and can it be reasonably described with s-type orbitals, as we have just discussed. We will compute the formation energies for the vacancy in +1 and +2 charge states.

4.2.1 Positively Charged Oxygen Vacancies ($V_O^\bullet, V_O^{\bullet\bullet}$) in MgO

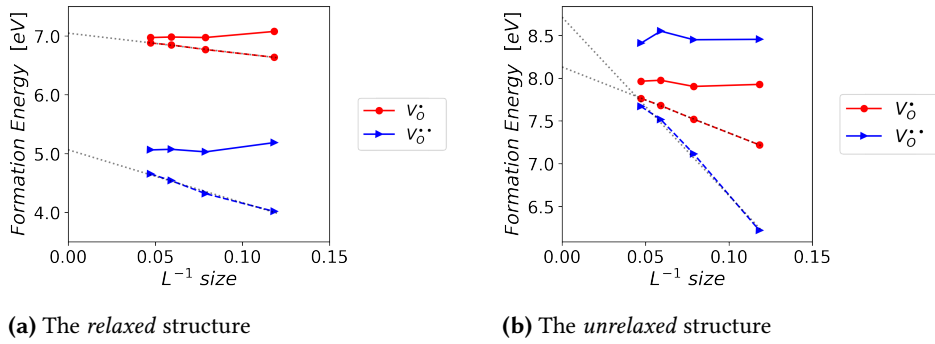


Figure 4.6: The formation energy vs $1/L$ for oxygen vacancy (V_O) in $q = +1, +2$ states, using ρ_{defect} as in Eq 3.35. Dashed lines correspond to uncorrected data, while solid lines are the corrected energies. The dielectric constants used to compute the electrostatic energy are ϵ_0 for the *relaxed* structure (panel a), and ϵ_∞ for the *unrelaxed* structure (panel b).

To check the validity of the correction approach, we check the convergence of formation energy as a function of supercell size for the two different charge states. To examine the convergence, we plot the charge-corrected formation energy vs. $1/L$. Figure 4.6 shows the results for the relaxed and unrelaxed structures with static (ϵ_0) and high-frequency dielectric constant (ϵ_∞), respectively. Note that in MgO the static dielectric constant $\epsilon_0 = 9.41$ is three times larger than the dynamic $\epsilon_\infty = 3.19$, and that the former has to be used for relaxed structures. For the unrelaxed case, on the contrary, the electrostatic screening is coming from the fast frequency response of the electrons and ϵ_∞ is needed. As we can see, the formation energy converges nicely for both charge states, although the

values are slightly overestimated for the smallest supercell. Note that structural relaxation has a strong effect on the stabilization of the defects, which goes from ≈ 8.5 eV (8.0 eV) in the unrelaxed structures to ≈ 5.0 eV (7.0 eV) in the relaxed system for $V_O^{\bullet\bullet}$ (V_O^\bullet).

4.2.2 The Gaussian Model (q_{model}) vs. The ρ correction scheme

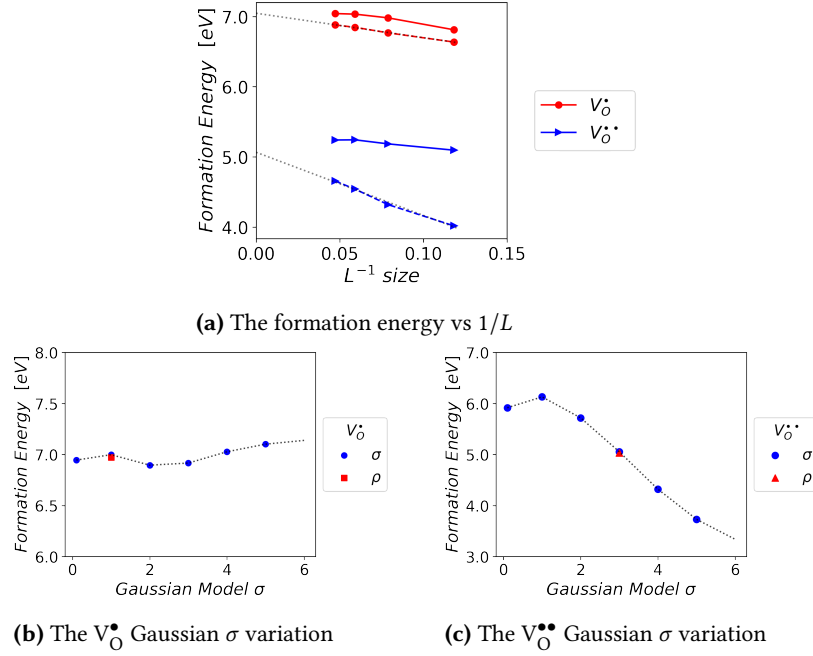


Figure 4.7: Results obtained for the formation energies of oxygen vacancy (V_O) in $q = +1, +2$ using a Gaussian charge model. (a) dependence with supercell size L ; (b) and (c) show the dependence of the formation energies with the width of the Gaussian (σ) for the +1 and +2 charge states computed with a $2 \times 2 \times 2$ supercell. The value obtained with the DFT charge is shown with the red square for reference.

To compare our correction scheme, using the ρ_{defect} charge, to the more conventional approach that uses a Gaussian model charge as originally proposed by FNV,[FNW09] we calculate the formation energies in the relaxed structure and present the results in Figure 4.7. The correction in this scheme also shows rather good convergence. However, now we must provide external parameters

that define a suitable description of the charge distribution around the defect, and as we saw previously, even if such distribution could be described with a Gaussian, the parameters might depend not only on the material and type of defect, but also on the degree of occupation of the defect level (see table 4.1 and figure 4.4). The charge model used here is a simple function determined with a width σ :

$$\rho_{\text{defect}} = qN_{\sigma} \exp^{-r^2/\sigma} \quad (4.1)$$

where $N_{\sigma} = (\pi\sigma^2)^{-3/2}$ is the corresponding normalization factor. In Figure 4.7 (b) and (c) we show the dependence of the results with σ , and as we can see the sensitivity of the formation energy for $V_{\text{O}}^{\bullet\bullet}$ can be of the order of several eV. In principle, we could fit our Gaussian to reproduce the exact charge distribution ρ_{defect} , however this is rarely done in the literature, and a fixed value of σ is used, no matter the system, nor the charge state. In the Figure, as reference, we plot the result obtained with ρ (red square in panels b and c). As expected, the different localization of the charges for V_{O}^{\bullet} and $V_{\text{O}}^{\bullet\bullet}$ result in significant differences in the optimal value of σ , which can mean errors of the order of up to eV in the formation energy!. But things could be worse. As we will see next, sometimes the Gaussian model is not able to describe at all the charge around the defect.

4.3 Charged Defects: When things go wrong.

The Gaussian model works reasonable well when the charge distribution is well localized around the defect. However, often the size of the supercells that can be used in DFT calculations are not large enough to contain the charge distribution. The artificial interactions, or hybridization between defects' images, result in defect states that form *defect bands*, as we will see in the following. This also implies that the defect charges spread over the whole cell, or have long tails which cannot be described with the Gaussian. Several improved models have been proposed. For example, we can have a correction to the Gaussian function which includes an exponential tail: [KRP12]

$$\rho_{\text{defect}} = q(1-w)N_{\sigma} \exp^{-r^2/\sigma} + qwN_{\gamma} \exp^{-r/\gamma} \quad (4.2)$$

where $N_\gamma = (8\pi\gamma^3)^{-1}$ is the normalization factor, and w is a weight factor that determines the charge contained in the tail of the function. For very delocalized charges, another alternative is to take [KRP12]:

$$\rho_{\text{defect}} = q(1 - w)N_\sigma \exp^{-r^2/\sigma} + qw/\Omega \quad (4.3)$$

In the following, we will show some simple examples discussed in the literature that highlight the simplicity of our approach, which does not rely on any parameter fitting but uses the charge density obtained directly from the DFT calculations.

4.3.1 Carbon Vacancies in Diamond Structure

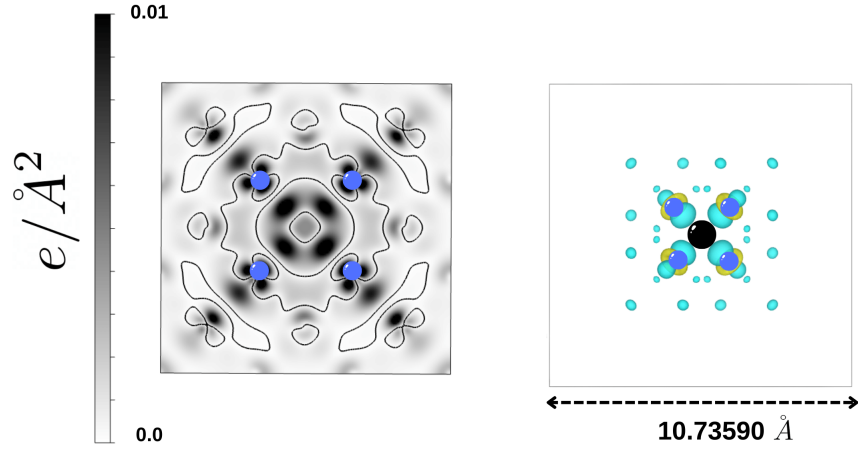


Figure 4.8: The carbon vacancy charge distribution ρ_{defect} as in Eq 3.35 for charge state $q = -4e$ in diamond structure shown from (100) lattice plane. Blue dots correspond to the C positions surrounding the vacancy, which is represented by the black dot. The left panel represents contour plots of the charge distribution, while the right panel plots a 3D isosurface corresponding to density of $0.1 \text{ e}/\text{\AA}^3$.

We shift our focus now to a covalent system where the defect charge is more

delocalized: The carbon vacancy defect in diamond (Figure 4.8). In diamond, due to sp^3 hybridization, we have four bonding orbitals in each C site. Thus, removing one C leaves four C neighbors with one dangling bond each, pointing towards the vacancy. If we call them a, b, c, d , then we can form linear combinations of these orbitals, and form one singlet ($a + b + c + d$) and one triplet state ($a + b - c - d$), ($a - b - c + d$) and ($a - b + c - d$). The singlet is lower in energy (with the valence bands), and the triplet corresponds to the three states that we see in the gap (Figure 4.9). We have $4e$ moving around the vacancy in the neutral configuration, 4.9-(b), the singlet level populated with spin up and down, and the triplet with two unpaired electrons. So total spin moment = $2\mu_B$ for the neutral case. There is an extra available state in the triplet, so that adding one electron, gives a spin moment = $3\mu_B$ Figure 4.9-(c). Adding two-electrons reduces the spin moment to $2\mu_B$, Figure 4.9-(d). Adding three electrons will give a spin moment of = $1\mu_B$ Figure 4.9-(e). Finally adding the fourth electron all the defect states are populated and gives zero spin moment = $0\mu_B$, Figure 4.9-(f). The localized carbon vacancy in $q = -4e$ charge states is shown in Figure 4.8. Similarly, we could remove one electron from the neutral vacancy, thus having spin moment = $1\mu_B$ Figure 4.10-(a). If we remove 2, then spin moment = $0\mu_B$, Figure 4.10-(b).

We used the ρ correction scheme for relaxed structures with carbon vacancies in different charged states in Diamond with static dielectric $\epsilon_0 = 5.76$ ($\epsilon_0 = \epsilon_\infty$ [Dur+18]), and the results are presented in Figure 4.11. As we can notice from Figure 4.11, all charge defects converged very nicely with our approach, and we don't have the difficulties discussed by Komsa and collaborators [KRP12] in building the model charge distribution (Gaussian plus delocalized constant charge). Also, we note that our approach gives results (Figure 4.11) in good agreement with Durrant *et al.* [Dur+18].

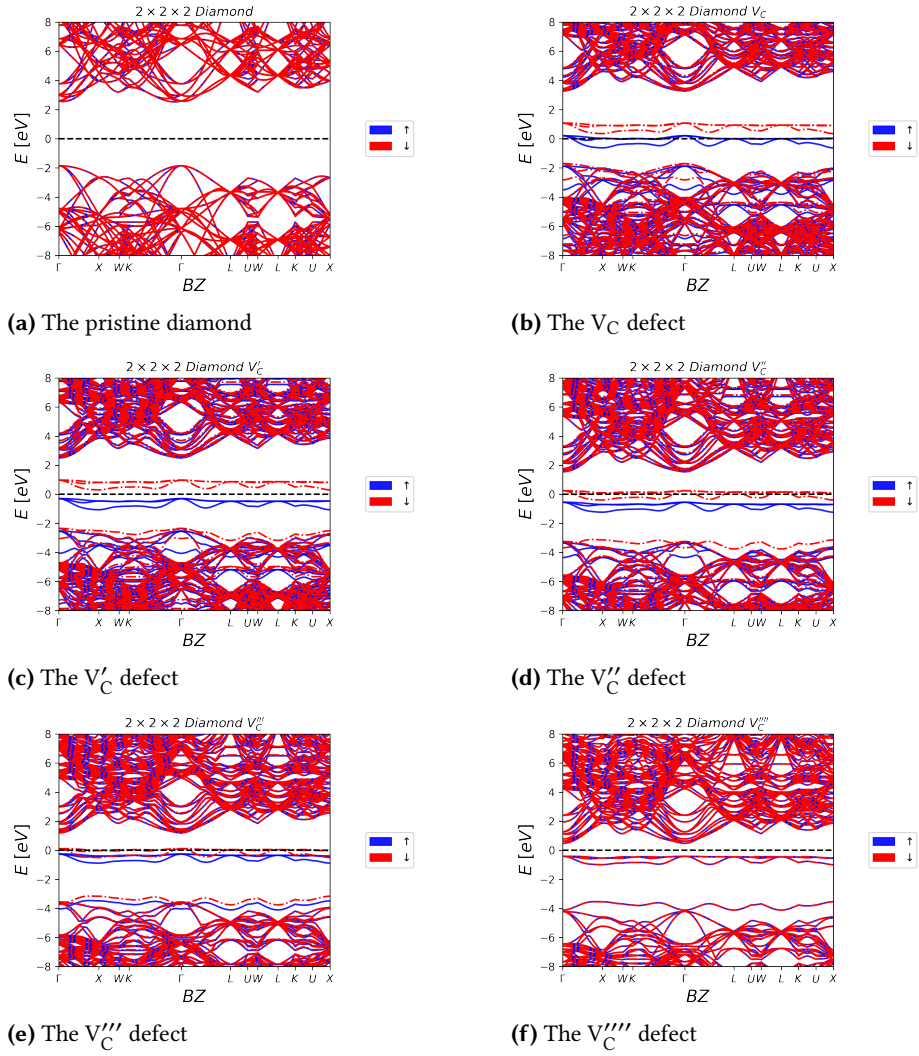


Figure 4.9: Spin polarised electronic band structure for carbon vacancy in Diamond along the high symmetry path in the Brillouin Zone, for different charge configurations. Bands for spin up and down are plotted as blue and red lines. The Fermi level is placed at 0 eV. (a) bands for the pristine system. (b) neutral vacancy, with two electrons populating the up spin triplet state. (c) an additional electron fills the triplet band with spin up. (d) to (f) correspond to adding additional electrons that populate the down spin triplet bands.

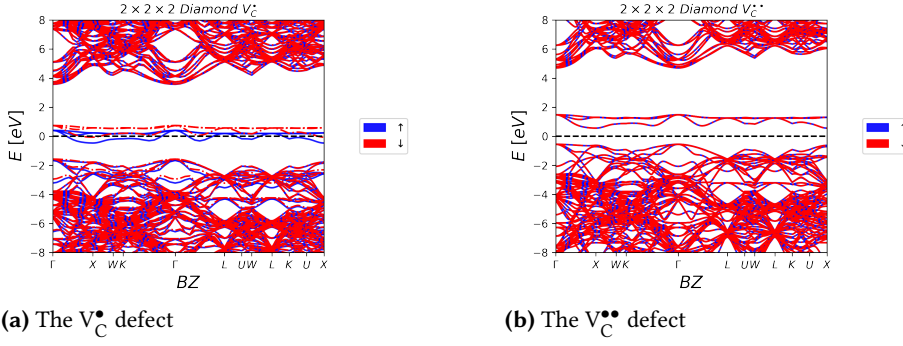


Figure 4.10: Spin polarised electronic band structure for positively charged carbon vacancy in Diamond. Bands for spin up and down are plotted as blue and red lines. The Fermi level is placed at 0 eV. (a) Positively charged V_C^\bullet , where only one electron populates the up spin triplet state. (b) $V_C^{\bullet\bullet}$ defect, where no electrons are placed at the triplet state.

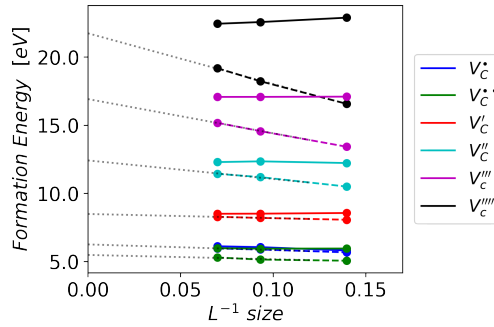


Figure 4.11: The Formation Energies of V_C in different supercell of diamond vs. $1/L$ using ρ_{defect} as in Eq 3.35 for correction scheme with static dielectric $\epsilon_0 = 5.76$

4.3.2 Negatively Charged Ga Vacancy ($V'_{Ga}, V''_{Ga}, V'''_{Ga}$) in GaAs

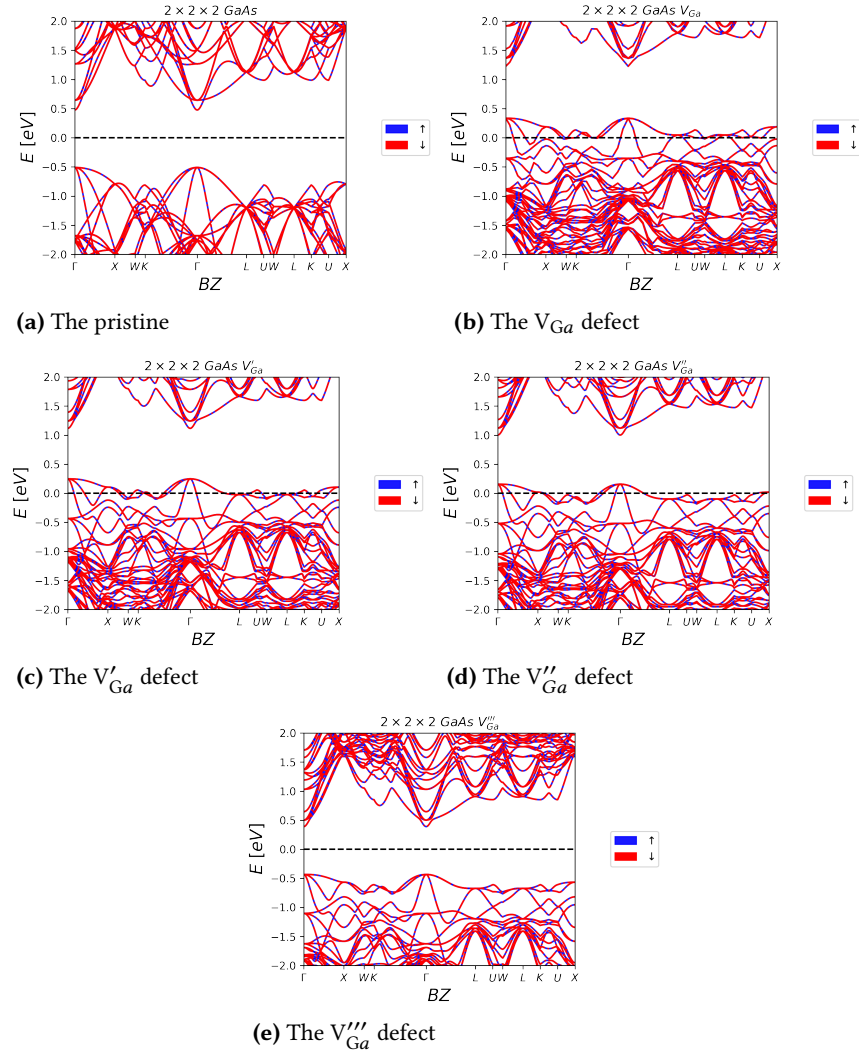


Figure 4.12: Spin polarised electronic band structure of pristine (a) and V_{Ga} in GaAs along a typical high symmetry path in the Brillouin Zone. Different electrons are added to the system to populate the triplet defect state, from zero (neutral defect) to $-3e$ (V'''_{Ga}), panels b to e. The Fermi energy is shifted to Zero for all bands.

We also use the ρ corrections for Ga vacancy (V_{Ga}) in GaAs, that shows a

deep localized defect which is even more spread than the one discussed for the carbon vacancy in Diamond.

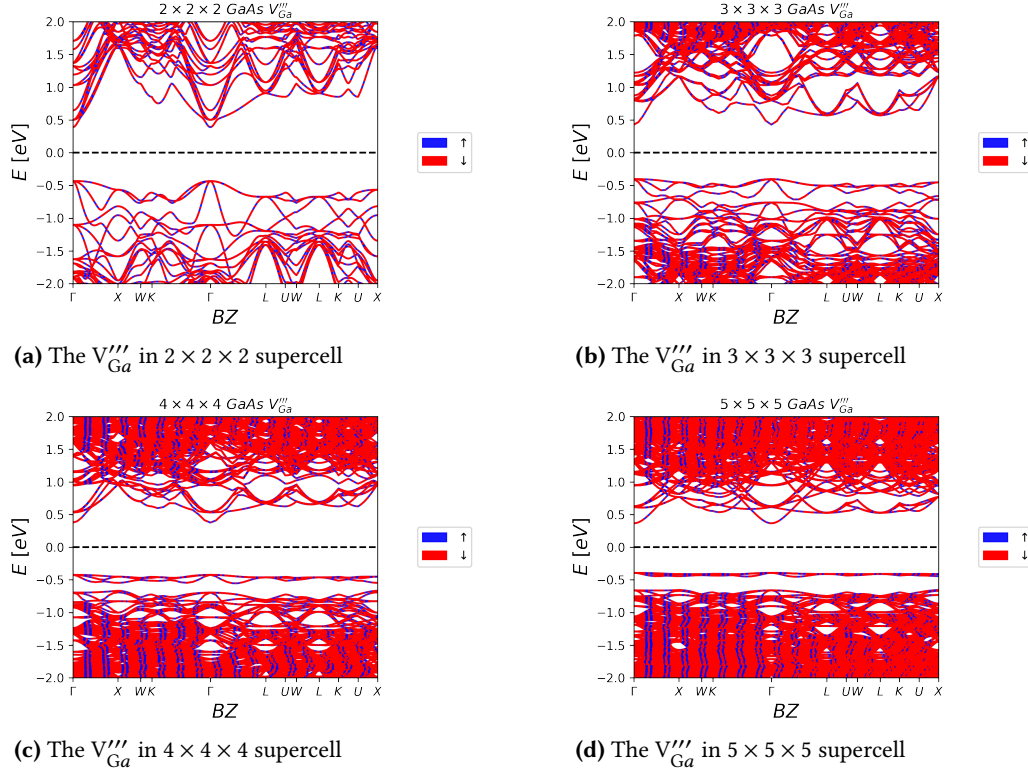


Figure 4.13: Band structure of V'''_{Ga} defect in GaAs using different supercells: (a) $2 \times 2 \times 2$; (b) $3 \times 3 \times 3$; (c) $4 \times 4 \times 4$; and (d) $5 \times 5 \times 5$. The dispersion of the triplet state reduces with the size of the cell.

In GaAs, each Ga is surrounded by four As atoms (and vice versa). Creation of a vacancy, V_{Ga} , breaks those bonds to As and creates dangling bonds. Following similar reasoning as for carbon vacancy in diamond, those dangling bonds have sp^3 hybridization and form bonding and antibonding states. To conserve T_d symmetry of the zincblende structure, antibonding states belonging to the threefold-degenerate T_2 representation form deep localized states in the energy gap. In contrast, the bonding state belongs to A_1 and lies within the valence band [NZ94]. Therefore, creating neutral gallium vacancy three valence electrons

become localized at the defect level and allows to accommodate three more electrons in the system as illustrated in Figure 4.12. As opposed to V_C in diamond, where a clear defect level was observed in the gap, here there seems to be just a reduction of the band gap, and a new dispersive band above the valence band. The reality is that there is a defect level, which contains 3 electrons, but this is very broad and dispersive. This dispersion is due to size of the supercell used in this calculation ($2 \times 2 \times 2$).

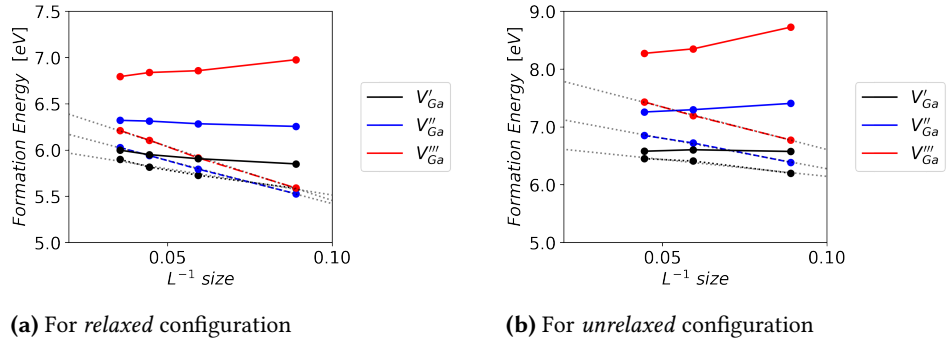


Figure 4.14: The formation energy of $q = -1e, -2e, -3e$ charged gallium vacancy (V_{Ga}) as a function of the size of the supercell. The correction scheme (solid lines) uses ρ_{defect} as in Eq 3.35 and $\epsilon_0 = 12.9$ for *relaxed* and $\epsilon_\infty = 10.89$ for *unrelaxed* structures. The dashed lines correspond to the uncorrected energies.

Using larger supercells clearly illustrates this effect, as shown in Figure 4.13 for V'''_{Ga} . In this charge state, the defect level is completely occupied, and it becomes clear from the figure that at least a $4 \times 4 \times 4$ supercell is required to avoid the artificial interaction between periodic images of the defect level that give rise to the dispersive band in the smaller supercells. Note that the localization of the defect density could be sensitive to the exchange-correlation used. Typically, such large supercells are not used to study defects with DFT, and the defect state would be spread throughout the whole supercell. This poses a problem to correction schemes that assume a nicely localized Gaussian charge distribution, as reported in the literature, and was the motivation for improving the model charges to more the delocalized expressions, as the ones in Eq 4.2 or 4.3. A correction scheme that converges for smaller supercells (even when the defect charge spreads throughout the whole cell) without the need to parametrize

a model potential is an advantage for automatic, unsupervised workflows for high-throughput calculations.

We validate the quality of our approach to correct the defect formation energy based on the use of ρ studying the gallium vacancy in GaAs with different charge states ($q = -1e, -2e, -3e$). The static dielectric $\epsilon_0 = 12.9$ is used for the *relaxed* and $\epsilon_\infty = 10.89$ for the *unrelaxed* structure. The results are presented in Figure 4.14. The good convergence of the energy, even for the smaller supercells indicates that our approach is able to reproduce the correct behaviour even in these critical cases where a simple Gaussian model fails because of the large delocalization of the defect charge. Note that the method seems to overcorrect for small supercells when structural relaxations are not included.

4.3.3 Oxygen Vacancies ($V_O, V_O^\bullet, V_O^{\bullet\bullet}$) in HfO_2

As we just saw, structural relaxations can affect the localization of the defect charge. However, they can also introduce difficulties in determining the potential alignment term. Here we illustrate two different problems which can come up when studying charged defects applying the correction schemes. Our example is on cubic HfO_2 , where neutral oxygen vacancies are linked to a populated defect state in the gap, as shown in Fig. 4.16-(b). As for MgO , removing one electron leaves a single spin state occupied, Figure 4.16-(c), and extracting the second electron completely depopulates the defect state, Figure 4.16-(d). Note that in this case, unlike the $V_O^{\bullet\bullet}$ in MgO , the defect level falls in the conduction band. This could be a shortcoming of the exchange correlation functional, which underestimates the band gap, or fails to localize the electronic state of the defect. If we plot the charge distributions for the charged defects (Figure 4.15) we clearly see a well localized distribution for $q = +1$ but an entirely delocalized distribution for $q = +2$. A similar effect was discussed by Komsa *et al* [KRP12] for charged V_C in diamond, although we saw that our method did have the same problem there. Note however that these problems are linked to a failure of DFT, not failure of the correction schemes for charged defects. In these cases, improvements on the XC-functional, such as a simple Hubbard correction, or more elaborated approximations such as hybrid functionals, could be used to improve the correct description of the electronic structure. In any case, our computed formation energies for V_O, V_O^\bullet , and $V_O^{\bullet\bullet}$ in Oxygen-rich are 8.51, 5.50 and 2.08 eV not far from the values reported in the literature [Ala+21].

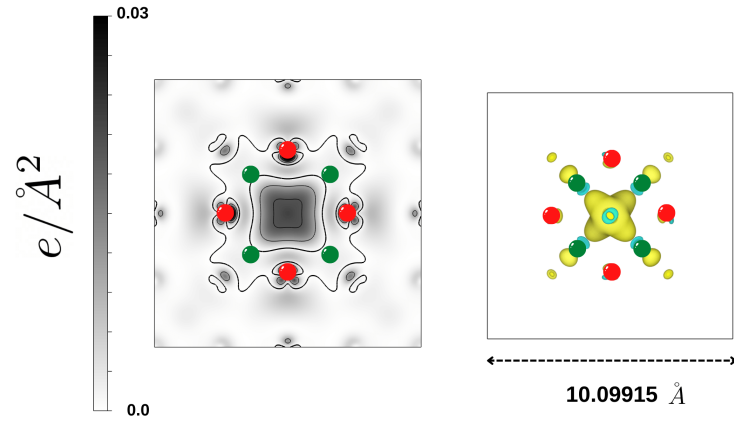
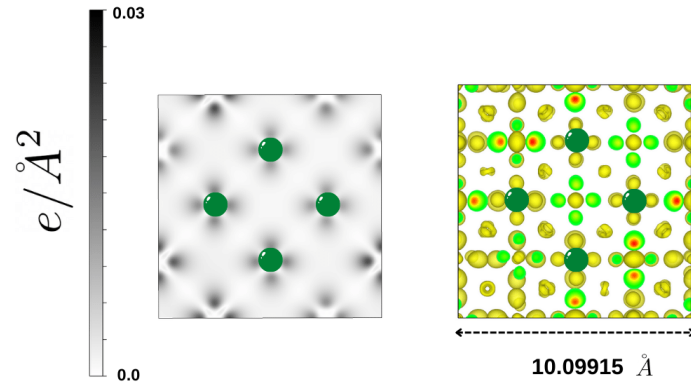
(a) V_O^\bullet defect charge distribution(b) $V_O^{\bullet\bullet}$ defect charge distribution

Figure 4.15: Oxygen vacancy charge distribution ρ_{defect} as in Eq 3.35 shown from (011) lattice plan for charge state in $q = +1, +2$ in cubic HfO_2 structure. Green and red dots denote the Hf and O atoms surrounding the oxygen vacancy, respectively. The left panel represents 2D contour plots of the charge distribution, while the right panel plots a 3D isosurface corresponding to density of $0.015 \text{ e}/\text{\AA}^3$ and $0.005 \text{ e}/\text{\AA}^3$ for V_O^\bullet and $V_O^{\bullet\bullet}$ respectively.

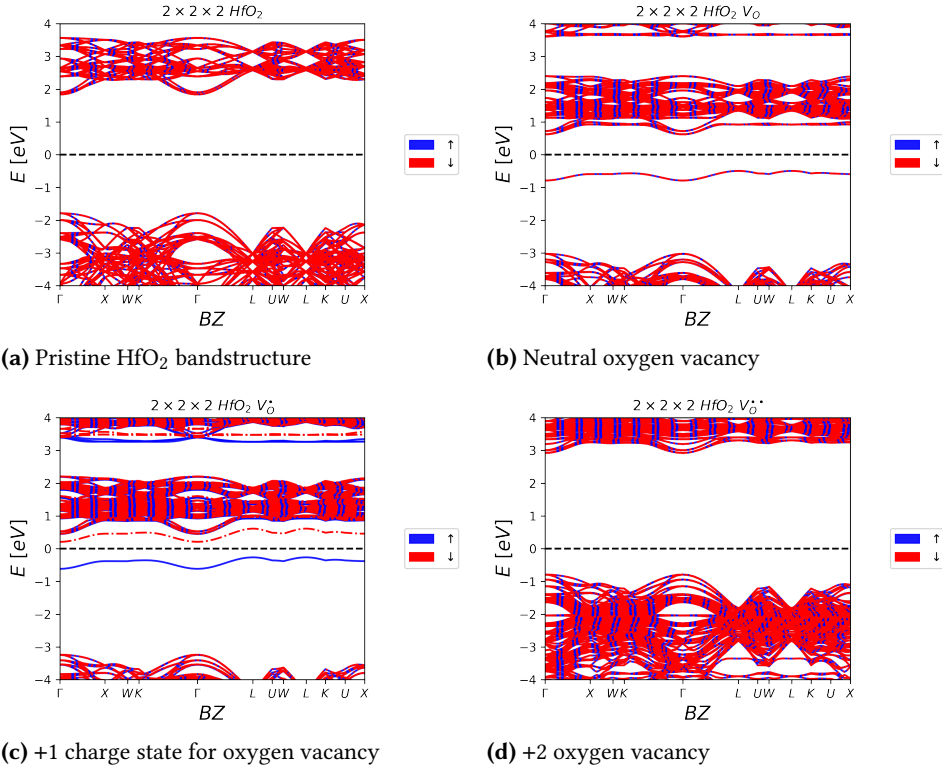


Figure 4.16: Spin polarised electronic band structure of pristine (a), neutral (b) and positively charged (c-d) oxygen vacancy defect in HfO₂ along the high symmetry path in the Brillouin Zone. The Fermi energy is shifted to Zero for all bands. (a) Pristine system with a clear band gap (b) A defect state in the gap, which is partially filled with 2 electrons (c) The defect states in the gap, which is partially filled with 1 electrons. (d) Completely depopulated defect state falls in the conduction band and is not visible in the gap.

4.3.4 Comments on negatively charged oxygen vacancies

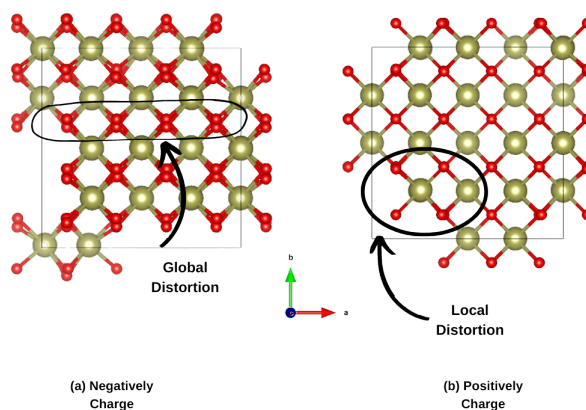


Figure 4.17: *Relaxed* structure obtained for “cubic HfO₂ with V_O' and V_O^\bullet defect. (a) The relaxation of V_O' defect induces a global structural distortion, and the final structure corresponds to the tetragonal phase of HfO₂. (b) The relaxation of V_O^\bullet defect induces a local distortion, but the cubic phase remains far from the defect.

To showcase another potential problem that can arise when studying charged defects, we present results for negatively charged oxygen vacancies in HfO₂. We plot V_O' and V_O'' charge distributions in Figure 4.18, which shows that although there is delocalization of the charge around the vacancy, part of the charge is localized. Although the charge distribution is quite spread, this does not significantly affect the calculation of the defect formation energy. However, the extra electrons added to the vacancy destabilize the cubic structure resulting in strong structural distortions which drive a transition from the cubic phase into the tetragonal phase, as shown in Figure 4.17. Thus, the structural relaxation of the negatively charged vacancy is not a local deformation of the atomic structure around the defect, but a complete crystal deformation in the simulation box. This poses a challenge for a correct alignment of the electronic potential of the defect structure to the reference bulk pristine value: it is impossible to find a region far from the defects structure (which is now tetragonal) where the potential can be aligned to the bulk region (which was cubic). We encountered this problem both in HfO₂ and in ZrO₂. One possible route to partially alleviate this problem is to impose constraints on the relaxations, although this introduces conceptual problems as it hides the physical mechanism behind the distortion.

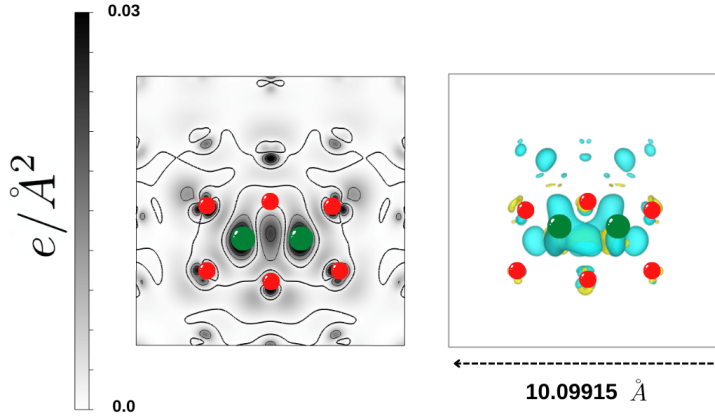
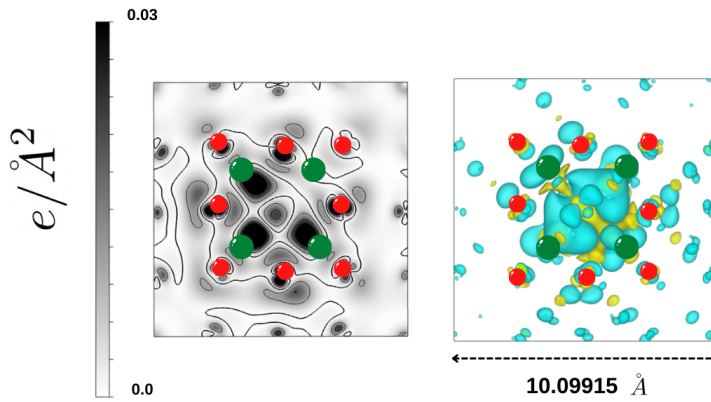
(a) V'_O defect charge distribution(b) V''_O defect charge distribution

Figure 4.18: Oxygen vacancy defect charge distribution ρ_{defect} as in Eq 3.35 shown from (011) lattice plan for $q = -1e, -2e$ in cubic HfO_2 structure (a) delocalized charge (b) delocalized charge with longer tail. Green and red dots denote the Hf and O atoms surrounding the oxygen vacancy, respectively. The left panel represents 2D contour plots of the charge distribution, while the right panel plots a 3D isosurface corresponding to density of $0.02 \text{ e}/\text{\AA}^3$ for both V'_O and V''_O .

4.4 Charged Defect Formation Stability Diagram

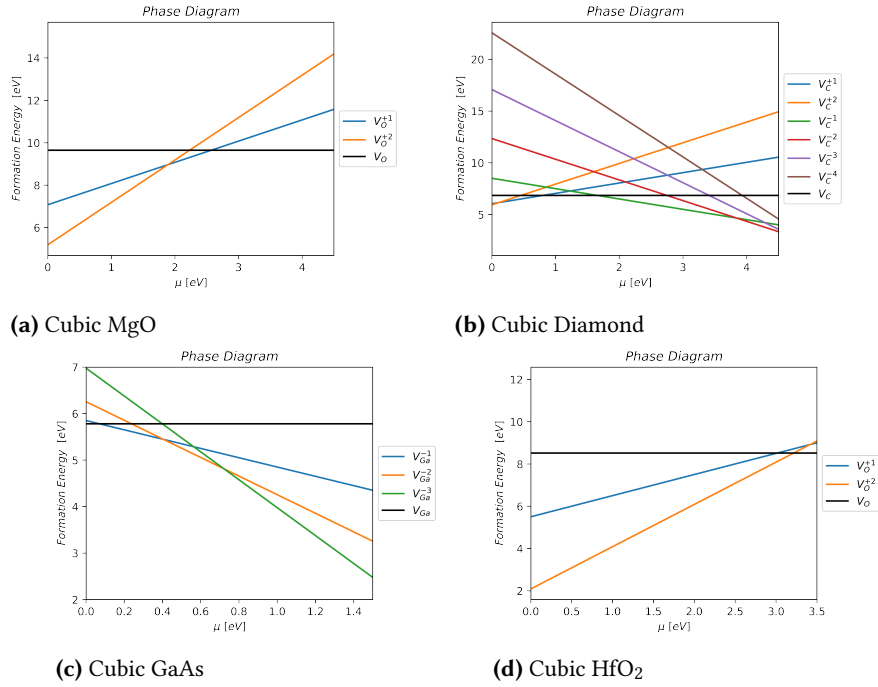


Figure 4.19: The Phase Diagram of MgO, Diamond, GaAs, HfO₂, (a) For Cubic MgO the oxygen vacancies ($V_O^{q_e}$) in $q_e = 0, +1, +2$ charge states phase diagram (b) Cubic Diamond V_C defect formation phase diagram (c) Cubic GaAs V_{Ga} defect formation stability diagram (d) Cubic HfO₂ oxygen vacancy (V_O) defect formation stability diagram

It is common in the literature to plot the defect formation energies for charged defects as a function of the electronic chemical potential, which is the position of the Fermi level within the band gap. In Figure 4.19 we plot such stability diagrams for the charged defects discussed in the chapter. This stability diagram shows which charged defect is more stable depending on the value of μ_e . For example, in MgO the $V_O^{\bullet\bullet}$ is more stable below ~ 2 eV above the valence band. After that, the stable defect is V_O^\bullet until above ~ 2.5 eV, when the defect level becomes fully occupied and the neutral vacancy is the most stable configuration. For cubic HfO₂, on the other hand, $V_O^{\bullet\bullet}$ is the most stable up until very close to the conduction band, where there is a transition to the neutral vacancy. This is

known as negative- U behaviour, as it is energetically favorable for the vacancy to trap to electrons.

4.5 Computational Details

Table 4.3: The DFT exchange-correlation functional, basis sets, k -points, and the mesh cutoff that we used for each system

System	Functional	k -points	Mesh-Cutoff [Ry]
MgO	GGA-PBEsol [CFD11a]	6×6×6	750
Diamond	GGA-PBEsol [CFD11b]	8×8×8	750
GaAs	LDA-PW92 [RRA18]	8×8×8	600
HfO ₂	GGA-PBEsol [CFD11b]	8×8×8	800

As we noted, to calculate the defect charge distribution, we relax the system in the required charge state and re-calculate the electronic structure using this relaxed atomic structure but as a neutral system (which we call *neutralized defect*) without any further relaxation. We use the charge difference between the charged and the neutralized systems to define the defects charge distribution, which we then use to calculate its periodic potential using the dielectric constant of the material, and remove the artificial interaction of the periodic local charges from the formation energy of the defect. The alignment potential term is obtained by taking the value of the planar averaged potential at an intermediate region between the defect and one of its images. In all the calculated formation energies, the electron chemical potential is set to $\mu_e = V_{BM}$ which essentially means the Fermi level is placed at zero ($\mu_F = 0$). Finally the total formation energy is calculated by Eq 3.20. To describe the electronic wavefunctions we used double- ζ with polarization orbitals (DZP) basis set.

For MgO pseudopotentials include s, p, d , shells with cutoff radii of $2s(1.16)$, $2p(1.56)$ for Mg and $2s(1.26)$, $2p(1.36)$, $3d(1.26)$ for O. For diamond, C pseudopotentials include s, p , shells with cutoff radii of $2s(1.20)$, $2p(1.26)$. For GaAs Pseudopotentials include s, p, d , shells with cutoff radii of $4s(1.67)$, $4p(1.75)$, $3d(1.90)$ for Ga and $4s(1.81)$, $4p(1.61)$, $3d(1.81)$ for As. For HfO₂ Pseudopotentials include s, p, d, f , shells with cutoff radii of $5s(1.56)$, $5p(1.62)$, $5d(1.40)$, $4f(1.62)$ for Hf and $2s(1.26)$, $2p(1.36)$, $3d(1.26)$ for O.

The DFT exchange-correlation functional, basis sets, k -points in unit cell, and

the mesh cutoff that we used for each system are presented in Table 4.3. All the Pseudopotentials are in the `PSML` format and obtained from pseudo-dojo vault [Gar+18]. Note that for supercell calculation we reversely scale the k -points from the vales used for unit cell, as an accepted common rule .

4.6 Conclusions

In this chapter we illustrate the use of our new developed tools to investigate the Formation Energy of charged defects with SIESTA. We compare the Gaussian charge model and the scheme based directly on the ρ obtained from *DFT*, highlighting the problems in the Gaussian scheme and the sensitivity of the results on the parameters that define the model. These problems are not present when using ρ , as we showed for different vacancy charged defects in different materials. We demonstrated the need to include *ghost* orbitals in the basis set to correctly describe vacancies' localized electronic states and their charge distribution. Supercell scaling diagrams show very good convergence in the Formation Energy with our scheme, unlike other models based on simple charge models. Finally, we illustrate the problem in convergence due to

- (i) Not using big enough supercells, which results in very large interactions with periodic images, and can give charge delocalization problems (defect band formation),
- (ii) failure of *DFT* functionals when localizing the charge density around the point defect,
- (iii) complex *PES* of materials where a small perturbation in atomic coordinates (such a point defect) can drive a lattice instability (or a phase transition), bringing problems for the potential alignment with respect to the pristine neutral crystal.



Part III

Defects Barriers

5.1 Introduction

One common and significant problem in computational chemistry is estimating the reaction rates for chemical processes, which is given as the energy cost required for a chemical reaction to happen. This problem is similar to the calculation of diffusion rate in condensed matter physics. In this chapter, our focus will be on diffusion barriers. To understand the barriers, first we will discuss the concept of *transition states* and theories to calculate the *transition states* height "barrier," specifically in solid.

5.2 Transition States

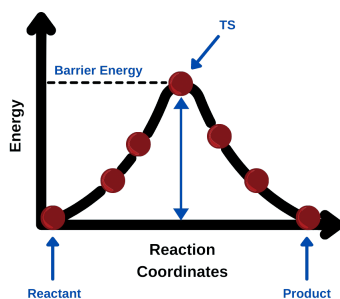


Figure 5.1: Different geometrical configurations (images) energies along the reaction path with the highest energy geometrical configuration known as *transition states*

We start from the definition of *Transition State (TS)* by considering a chemical reaction of



Both reactant and product are in stable configurations corresponding to minima

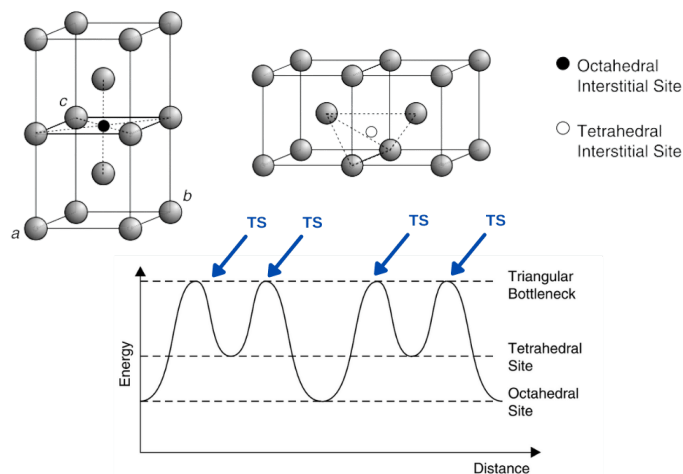


Figure 5.2: Geometrical configuration of the different interstitial sites energies along the reaction path for a BCC crystal [adapted from *Defects in Solids* by Richard J.D. Tilley, Wiley 2008 [Til08]]

on the potential energy surface within the Born–Oppenheimer approximation. Atoms (both nuclei and electrons) moving from one minimum to another describe the chemical reaction. There is a barrier energy for the reaction to be activated (atoms to move). As a first approximation, we could assume that these motions of atoms are along the path of least energy, which forms the basis for *Transition State Theory* (TST). This minimum energy state for activation is called the *Transition State*. We call *Transition Structure* to the geometrical configuration that corresponds to the energy maximum along the reaction path (Figure 5.1) that separates the two local minima of the reactants. The TS is a first-order saddle point in the multidimensional potential energy surface. From Boltzmann distribution, the probability of finding a molecule in a given quantum state is proportional to $\exp(\Delta E/kT)$. This concept could be transformed into diffusion of species in the crystal. Let us consider for example a body-centered cubic (BCC) structure. There are two octahedral and tetrahedral interstitial sites that could be occupied by a defect. The interstitial species could hop and occupy these sites. In each site, the defect is in a local stable configuration Figure 5.2. The probability of a successful jump is estimated with Maxwell-Boltzman statistics.

Thus, the probability of moving from one minimum to adjacent minima site is

$$p = \exp\left(-\frac{E_b}{kT}\right) \quad (5.2)$$

where k is Boltzmann constant and E_b is the height of the barrier (difference between *TS* and minimum energy).

5.3 Methods for Calculating *TS*

As we just mentioned, the *TS* is a first-order saddle point on the potential energy surface. Within the DFT framework, we can calculate the first & second order derivatives of the energy. However, the second derivative is computationally expensive, and one would want to avoid it. Hannes Jónsson *et al.* [HJ00] developed an alternative approach to tackle this problem. Their method is based on the refinement of the earlier "Chain-of-states" method which aims to define the minimum energy path (MEP) between two local minima. First, a guess of the MEP is found by constructing a set of images ⁵ (a chain-of-states) of the system between two local minima, the initial and final configuration Figure 5.3. An optimization of the chain-of-states (also known as *Bands*) takes the forces in configuration space to bring the images or chain-of-states (bands) to the MEP. Hence, as commonly done when optimizing structures from forces, iterative methods can be applied to find the transition state because they generate a series of configurations in the configuration space that move downhill toward minimum, Figure 5.3. The following section explains different flavors of the method for finding the saddle point (*TS*).

5.3.1 Nudged Elastic Band (NEB)

As mentioned, one of the alternative methods to find the *TS* was developed by Hannes Jonsson *et al.* and called *Nudged Elastic Band (NEB)* method. In the NEB method, the elastic band with $N + 1$ images is defined by $\{\mathbb{X}_0, \mathbb{X}_1, \mathbb{X}_2, \dots, \mathbb{X}_N\}$, where the endpoints, \mathbb{X}_0 (initial) and \mathbb{X}_N (final) ⁶, are fixed and given by the

⁵ by image, we mean all the atomic positions of the system in a particular state. This state could be the initial or transition state or anything between these two states. Later we will see we could add also cell parameters to describe the configuration space of our system

⁶ these are $3M$ -Dimensional vectors, for a system with M atoms

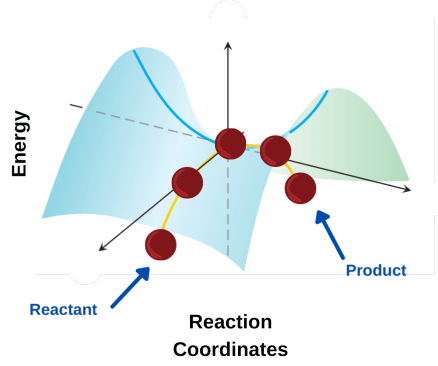


Figure 5.3: The geometrical configuration of the different image energies from reactant to product goes through a saddle point in *MEP*

energy minima corresponding to the initial and final configurations. The optimization algorithm adjusts the $N - 1$ intermediate images. The calculated *DFT* atomic force acting on an image i is

$$\mathbf{F}_i^{\text{DFT}} = \mathbf{F}_i^{\perp} + \mathbf{F}_i^{\parallel} \quad (5.3)$$

where \perp and \parallel are *perpendicular* and *parallel* forces on image i respectively. Here the concept *parallel* refers to the direction that connects two neighbouring images in the *band* as we will soon define. The first contribution is defined as:

$$\mathbf{F}_i^{\perp} = \underbrace{-\nabla E(\mathbb{X}_i)}_{\mathbf{F}_i^{\text{DFT}}} + \underbrace{\nabla E(\mathbb{X}_i) \cdot \hat{\tau}_i \hat{\tau}_i}_{-\mathbf{F}_i^{\parallel}} \quad (5.4)$$

where ∇ is the derivative with respect to the atomic coordinates, E is the *DFT* energy of the system, function of all the atomic coordinates, and $\hat{\tau}_i$ is the normalized local tangent vector at image i , which we define below. In the original formulation of the *NEB* method, the tangent at an image i was estimated from the two adjacent images along the path, \mathbb{X}_{i+1} and \mathbb{X}_{i-1} . The most straightforward estimate is to use the normalized line segment between the two consecutive images

$$\hat{\tau}_i = \frac{\mathbb{X}_{i+1} - \mathbb{X}_{i-1}}{|\mathbb{X}_{i+1} - \mathbb{X}_{i-1}|} \quad (5.5)$$

However, computationally speaking, a slightly better way is to bisect the two-unit vectors ⁷:

$$\tau_i = \frac{\mathbb{X}_i - \mathbb{X}_{i-1}}{|\mathbb{X}_i - \mathbb{X}_{i-1}|} + \frac{\mathbb{X}_{i+1} - \mathbb{X}_i}{|\mathbb{X}_{i+1} - \mathbb{X}_i|} \quad (5.6)$$

$$= \Delta\mathbb{X}_- + \Delta\mathbb{X}_+ \quad (5.7)$$

and then normalize

$$\hat{\tau} = \frac{\tau}{|\tau|} \quad (5.8)$$

In the *NEB* method the force F_i^{\parallel} is replaced by a model *spring constant*, and the force is replaced by:

$$\mathbf{F}_i^{\text{NEB}} = \mathbf{F}_i^{\perp} + \mathbf{F}_i^{\text{S}\parallel} \quad (5.9)$$

where the second term is the *spring force*, defined along the local tangent,

$$\mathbf{F}_i^{\text{S}\parallel} = k(|\mathbb{X}_{i+1} - \mathbb{X}_i| - |\mathbb{X}_i - \mathbb{X}_{i-1}|)\hat{\tau}_i \quad (5.10)$$

which keeps the image distances equivalent to each other. Here k is the spring constant and is an input parameter of the method. The different forces in the *NEB* method are illustrated in Figure 5.4

5.3.2 Climbing Image Nudged Elastic Band

In the *NEB* method, when the parallel force to the MEP is considerable compared to perpendicular force, there are kinks in the elastic band which prevent smooth convergence to the MEP. A slight modification to the *NEB* method is the climbing image *NEB* (*CI-NEB*) method. This method allows the algorithm to identify the image with the highest energy i_{max} . The force on this one image is not given by Eq 5.9 but rather by

$$\mathbf{F}_{i_{\text{max}}}^{\text{CI}} = \mathbf{F}_{i_{\text{max}}} - 2(\mathbf{F}_{i_{\text{max}}} \cdot \hat{\tau}_i)\hat{\tau}_i \quad (5.11)$$

This means that after a couple of iterations, if the force on particular a image is large, the parallel spring force on that image will be ignored and the full inverted

⁷ we used this approach in the flos library for *NEB*

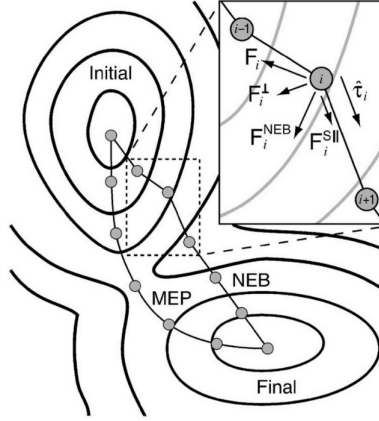


Figure 5.4: The Components of Forces in *PES* [Figure is taken from Optimization methods for finding minimum energy paths [STH08] ©

force due to the potential with the component along the band is applied to the image. This allows that image to move further to reduce the force acting on it. Besides the fact that this minor modification retains the shape of MEP and converges to a saddle point, it does not add any computational cost.

5.3.3 Doubly Climbing Image Nudged Elastic Band

There is a minor addition to the spring force in the *Doubly Nudged Elastic Band* (*DNEB*) modification to the *NEB*. In this modification, proposed by Trygubenko and Wales [TW04], a perpendicular component of the spring force that acts on the path is added to the *NEB* force. Explicitly, taking the component of the spring force, we get

$$\mathbf{F}_i^S = k[(\mathbb{X}_{i+1} - \mathbb{X}_i) - (\mathbb{X}_i - \mathbb{X}_{i-1})] \quad (5.12)$$

which is perpendicular to the tangent $\hat{\tau}_i$

$$\mathbf{F}_i^{S\perp} = \mathbf{F}_i^S - (\mathbf{F}_i^S \cdot \hat{\tau}_i) \hat{\tau}_i \quad (5.13)$$

The perpendicular force \mathbf{F}_i^\perp and the perpendicular spring force $\mathbf{F}_i^{S\perp}$ are both in same plane of the normal to the tangent $\hat{\tau}_i$ at image i . The double nudging force

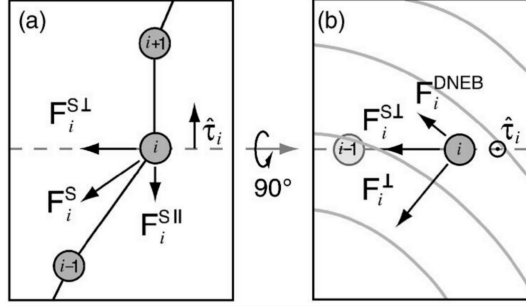


Figure 5.5: (a) DNEB different force components to keep band straight. the (b) is force on image perpendicular to the band [Figure is taken from Optimization methods for finding minimum energy paths [STH08] ©

F_i^{DNEB} is the component of $F_i^{S\perp}$ which is orthogonal to F_i^\perp

$$F_i^{DNEB} = F_i^{S\perp} - (F_i^{S\perp} \cdot F_i^\perp) F_i^\perp \quad (5.14)$$

The addition of this force to all nonclimbing images of the *NEB* is the *DNEB*. This method performs nicely in long pathways with high initial forces [STH08].

5.3.4 Variable Cell Climbing Image Nudged Elastic Band

Up to here, a set of images $\{\mathbb{X}_0, \mathbb{X}_1, \mathbb{X}_2, \dots, \mathbb{X}_N\}$ connecting the two endpoints were used to describe the transition path containing a special configuration space of coordinates, and we fixed out cell shape and vectors. Now we extend the *NEB* to *Variable cell NEB* (*VC-NEB*), which also has the components from the cell in the configuration space [Qia+13]. If the lattice matrix is described by \mathbf{h} the volume will be $\Omega = \det(\mathbf{h})$. The vector describing the full configuration space is

$$\mathbb{Y} = (\epsilon_{1i}, \epsilon_{2i}, \epsilon_{3i}; r_1, r_2, \dots, r_N) \quad i = 1, 2, 3 \quad (5.15)$$

With $9 + 3N$ components. Here, the ϵ_{ij} ($i, j = 1, 2, 3$) is the 9 strain tensor components that is chosen for the variable instead of \mathbf{h} along with $3N$ configurational

components $\{\mathbb{X}\}$. we could write

$$\mathbf{h} = (1 + \bar{\epsilon})\mathbf{h}_0 \quad (5.16)$$

Now under the applied pressure P , the enthalpy $\mathcal{H} = E + P\Omega$ is determined by the $(9 + 3N)$ -dimensional potential energy surface we called the "*enthalpy surface*" and we could rewrite the force vector as follows

$$\mathbb{H} = \mathbb{H}(\epsilon_{1i}, \epsilon_{2i}, \epsilon_{3i}; r_1, r_2, \dots, r_N) \quad i = 1, 2, 3 \quad (5.17)$$

The derivative of the enthalpy can define the expanded "*force vector*" in a $9 + 3N$ configuration space concerning \mathbb{Y} as following

$$\mathbf{F} = -\left.\frac{\partial \mathbb{H}}{\partial \mathbb{Y}}\right|_p \quad (5.18)$$

The strain components of \mathbf{F} on the lattice are the derivatives of \mathbb{H} with respect to

$$f_{(\bar{\epsilon})} = -(\sigma + PV)(1 + \bar{\epsilon}^T)^{-1} \quad (5.19)$$

Where σ is the quantum-mechanical stress tensor at a given configuration \mathbf{X} , the forces on atoms, f_1, f_2, \dots, f_N , can be obtained from the Hellmann–Feynman theorem. Finally, the general force \mathbf{F} can be written as

$$\mathbf{F} = (f_{(\bar{\epsilon})}, gf_1, \dots, gf_N)^T \quad (5.20)$$

To keep the symmetry during structure relaxation, we use the metric tensor $g = \mathbf{h}\mathbf{h}^T$. The τ is tangent vector along the path of *NEB*, the transverse components of the potential forces acting on the lattices and atoms are respectively defined as $f_{(\bar{\epsilon})}^{\nabla\perp}$ and $f_v^{\nabla\perp}$, and finally the nudging spring forces on lattices and atoms to keep the image spacings are $f_{(\bar{\epsilon})}^{S\parallel}$ and $f_v^{S\parallel}$. Now we introduce the *VC-NEB* force \mathbf{F}^{VC-NEB} which consists of two-component. The one component is the cell force $f_{(\bar{\epsilon})}^{VC-NEB}$ acting to reshape the new image of the cell, and the second component is the atom force f_v^{VC-NEB} shifting the atoms component.

$$f_{(\bar{\epsilon})}^{VC-NEB} = f_{(\bar{\epsilon})}^{S\parallel} + f_{(\bar{\epsilon})}^{\nabla\perp} \quad (5.21)$$

$$f_v^{VC-NEB} = f_v^{S\parallel} + f_v^{\nabla\perp} \quad (5.22)$$

$$\mathbf{F}^{VC-NEB} = \left(f_{(\bar{\epsilon})}^{VC-NEB}, g f_1^{VC-NEB}, g f_2^{VC-NEB}, \dots, g f_N^{VC-NEB} \right) \quad (5.23)$$

The basic procedure of the *VC-NEB* technique is similar to the *NEB*. Nonetheless, in each image, we have more degree of freedom (lattice degree of freedom).

5.4 Image Generations

As discussed, finding the *TS* with *NEB* methods involves finding a discrete representation of the *MEP*. As a starting point, one needs some initial guess to define the *MEP* and begin the *NEB* algorithm. We will show two possible methods for generating those images in the following.

5.4.1 Linear Interpolation Method

One of the first methods to generate the *NEB* images is a *Linear Interpolation (LI)* of the coordinates of N atoms between the two endpoint configurations, namely $\{\mathbb{X}_{initial}\}$ and $\{\mathbb{X}_{final}\}$. Here, \mathbb{X} represent the vectors of $3N$ coordinates of the atoms in a given configuration, $\{\mathbb{X}_1, \mathbb{X}_2, \dots, \mathbb{X}_N\}$. Specifically, given that $N - 1$ intermediate discretization points, here referred to as "*images*" of the system and as the initial path (images) for *NEB* calculations, *LI* is simply generated as follows

$$\mathbb{X}_{LI,i}^n = \mathbb{X}_i^{initial} + n \left(\frac{\mathbb{X}_i^{final} - \mathbb{X}_i^{initial}}{N} \right) \quad (5.24)$$

5.4.2 Image Dependent Pair Potential Method

Using *LI* paths can be unrealistic and give atoms becoming too close, which leads to large atomic forces or even convergence problems in the electronic self-consistency. These issues can be solved by preventing the atoms from being too close. A procedure was first proposed by Halgren and Lipscomb [HL77] and then refined by Jonsson et al. [Smi+14] and known as *Image Dependent Pair Potential (IDPP)*. This method generates a path with evenly distributed images, where atom pair distances gradually change from one image to another.

5.5 Defects Diffusion & Barriers

We will use these tools to generate new paths for different kinds of barriers in crystalline solids. But first we review the definition of *barriers* and *diffusion* in the crystal structure. *Diffusion* is a physical phenomenon in which particles (in general, atoms, ions, or molecules) flow through a surrounding medium. Here we talk in particular about the diffusion of atoms in a crystal, so there are two main players for consideration: (i) the structure of the solid that host the moving specie, and (ii) the moving specie itself, which is considered as a defect (a dopant, an impurity, or a vacancy, etc). Diffusion involves the movement of this specie from a stable position in configuration space (minimum in *PES*) to another stable position (minimum in *PES*) through some less stable positions in configuration space. The difference between the minima and the highest energy point in going to another minimum is what we call energy barrier. Any disorder in the solid due to other defects can affect the energy barrier, increasing or decreasing it. Next, we will discuss and categorize the different migration paths that we have considered.

5.5.1 Defects Diffusion Types

Vacancy & Interstitial Diffusion

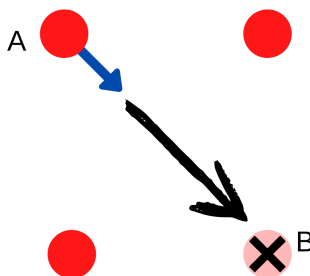


Figure 5.6: vacancy & interstitial Diffusion scheme

In the simplest case, an interstitial can jump to a neighboring interstitial position Figure 5.6. This is called *interstitial diffusion* and is occasionally referred to as *direct diffusion* to distinguish it from vacancy diffusion (*indirect diffusion*). Diffusion parallel to a cubic axis in body center crystal structure is an example.

If interstitials, self-interstitials, or impurities such as dopants are presented in crystal, diffusion is feasible if these species jump between alternating empty sites Figure 5.2.

To explain the vacancy diffusion, we start assuming a metal crystal where all-atom sites are occupied. Naturally, diffusion from one normally occupied site to another would be possible only if some vacant sites are present in the crystal. Atoms can jump from a normal site (occupied by specie) into a neighboring vacancy (vacant site) and gradually move through the crystal. The movement of a diffusing atom into a vacant site corresponds to the movement of the vacancy in the other direction Figure 5.6. We call this *vacancy diffusion*.

Kick Diffusion

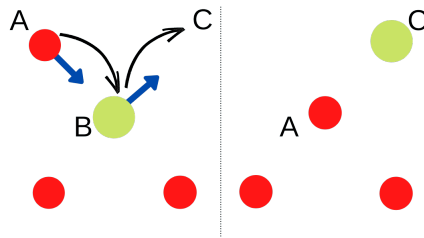


Figure 5.7: kick-in/out scheme

Another diffusion mechanism are, consisting of two subcategories which we name *kick-in* and *kick-out*. *Kick-in* is an alternative mechanism by which interstitial atoms can diffuse. This process involves a jump to a normally occupied site and a simultaneous displace in of the occupant into a neighboring interstitial site. This *knock-on* process is also called *interstitialcy diffusion* Figure 5.7. Finally, an interstitial impurity can move onto a normal lattice site by interstitialcy diffusion, leaving a self-interstitial and a substitutional defect. This process is called the *kick-out* mechanism. An interstitial atom in the lattice can jump to an occupied lattice site, displacing the atom from the lattice (which becomes now an interstitial) and replacing it. This is known as *interstitialcy diffusion*, or *kick diffusion*. The kick mechanism could also be subcategorized into *straight* (co-linear) or *elbow* (non-colinear) interstitialcy diffusion depending on the displacement direction of the species.

Exchange & Vacancy Exchange

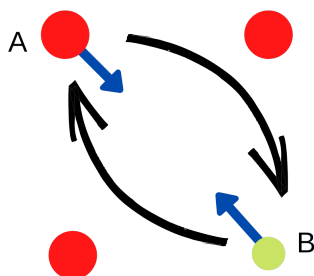


Figure 5.8: exchange & vacancy exchange scheme

Substitutional impurities or vacancies can swap places, as shown in Figure 5.8, and this process is called *Exchange*. The main difference between *vacancy* or *interstitial diffusion* and *exchange* here is that there is no need for a vacant site. Instead, the species swap their place using available space in the host structure.

Ring or n Exchange

As well as *vacancy diffusion*, an impurity can swap places with a neighboring atom in a circular way and we can call this *n-exchange diffusion* as shown in Figure 5.8. In contrast to *exchange*, in a *ring diffusion* or *n-exchange*, cooperation between several atoms is needed to make the *n-exchange* Figure 5.9.

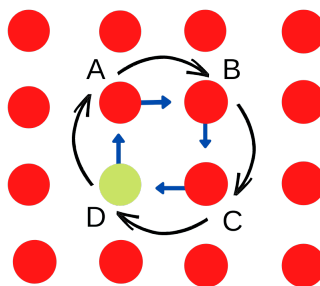


Figure 5.9: ring or n -exchange scheme

Structural transition

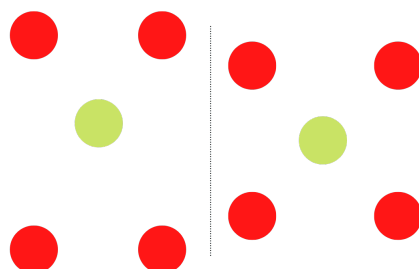


Figure 5.10: Structural Transition scheme

Finally, we consider a barrier path that does not include any diffusion but just atomic displacement and/or structural deformations. Although, it does not fall into the ionic conductivity properties of the material as earlier barrier types, it is of great importance in material science. In materials such as BaTiO_3 , the origin of ferroelectricity is due to ion displacements in the unit cell, which induce an electric dipole moment Figure 5.10. The structural distortion usually comes with a change in the crystal symmetry. For example a structural transition between the cubic and tetragonal/orthorhombic phases of the material.

5.6 Implementation of Sisl ToolBox Siesta Barriers and AiiDA Siesta Barriers

As we discussed, many ionic mobility paths in crystals depend on their symmetry, dopant characteristics, surfaces, the coexistence of phases, etc. Therefore having a workflow for computational screening for general materials investigation seems as a useful tool. I develop all mentioned paths in crystalline solids for calculating the barriers/diffusion in two separate packages:

- **Sisl ToolBox Siesta barriers:** is a python package tool inside the Sisl toolbox to generate different types of paths to calculate corresponding barriers. To see the manual, one could access to web page :

<http://zerothi.github.io/sisl/docs/latest/index.html>

- **AiiDA Siesta Barriers** : is a python package to automate calculations of different types of barriers with siesta through the AiiDA platform. To have access to the workflows and manual one can be found in web page : <https://github.com/siesta-project/aiida-siesta-barrier>

Again the motivation behind two separate packages is to keep the freedom of choice for the users. Since some do not want to do high-throughput calculations, so we provide them with a standalone python package in sisl to allow them to generate and calculate their desired path barriers.

The following chapter will use these implementations to calculate and illustrate their use to compute Barrier energy.

6

Siesta Barriers Applications

As discussed in the previous Chapter, calculating the *minimum energy path* (MEP) for atomic-scale processes in materials can be of great interest. In Solid State physics, one can use *Nudged Elastic Band* (NEB) methods to calculate the (MEP) for migration of defects.

The migration of ions through a crystal often require the presence of vacancies in the material. The same concerns that were taken into account in selecting a good basis to describe the ground state defect structure (in chapter 4 where we discussed the importance of *ghost* orbitals) must be considered for *TS*. Note that *TS* for a vacancy migration can be viewed as a defect structure with two vacancies and one interstitial, as illustrated in Figure 6.1-(b), and the basis should be capable of describing this complex scenario. It must be stressed that a basis that gives a good description for the initial *NEB* image Figure 6.1-(a) might not be appropriate for the final image Figure 6.1-(c), or the *TS*.

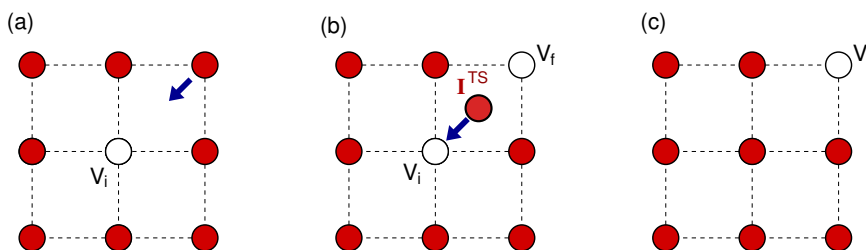


Figure 6.1: Scheme for the migration of a vacancy from the initial configuration (a) to the final (c). The Transition State (TS) is equivalent to an interstitial atom and two vacant sites placed at the initial and final positions.)

In addition, caution must be taken in applying for charged defects energy corrections, as the localization of the model charge used, for example in the FNV method. [FNW09] might be different in the initial, final and *TS* configurations. As we discussed before, *ghost* or *floating orbitals* are atomic orbitals centered at points where there are no real atoms (for example, the original position of the removed atom that forms the vacancy). For structural relaxations it is

commonly advised to keep fixed the position of the floating orbitals, as they are not associated to a mass and their movement tend to be erratic, usually leaving the empty vacancy site where they are more needed. Use of floating orbitals poses a few questions regarding the study of vacancy migration with *NEB*. How can we describe the simple process illustrated in Figure 6.1? If description of V_i requires a floating orbital, so will happen for V_f , which means that either the floating orbital is placed at different positions in each *NEB* image state, or there are more than one such orbitals. How do we determine the positions of the orbitals? What will be the effect of having a floating orbital close to a *real* atom? Would there be problems coming from linear dependencies in the basis functions (basis *over-completeness*)? How important would the *basis set superposition error* (*BSSE*) be?

In this chapter we address the feasibility of using these floating orbitals in *NEB* calculations within the SIESTA package, focusing on a prototypical example in which a well localized defect level exists: V_O in MgO.

6.1 Vacancy Exchange & Importance of ghosts species

Here we take *Density Functional Theory* (*DFT*) as the engine that drives the *NEB* method. Considering that modeling defects typically require cells with up to a few hundred atoms, and that the structural optimizations can be complex and require a number of force calculations, the computational cost and time to solution of a *NEB* calculation can be large, as we have to take *M*-images with a relatively large number of atoms. SIESTA is a very good option for running this kind of simulations efficiently, using relatively small but accurate basis sets at a modest computational cost. One of the key parts of the mentioned computational efficiency is the strict localization of the atomic orbitals basis set, in which the radial part of the orbital is forced to be zero beyond a given confinement radius r_c . Hence choosing good radii is important to acquired fast and accurate results. In analogy with our discussion on the use of *ghost* orbitals to properly describe the properties of vacancies (Chapter 4), here we will address the use of *ghost* orbitals on computing the migration energy barriers of vacancies.

As we anticipated in the introduction to the chapter, we take Magnesium Oxide (MgO), as test bed system which is simple and hosts the electronic characteristics that we want to put at test, in particular the presence of a localized defect level. It is also a well studied system and comparison with literature is possible. [El-+18;

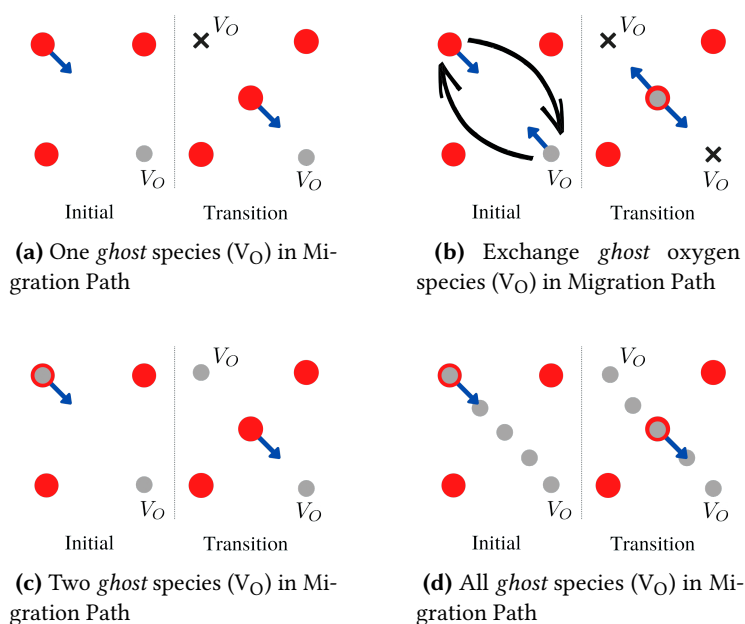


Figure 6.2: Possible approach of vacancy exchange barrier calculation (reds oxygen and gray *ghost* species)

MD11]. Having demonstrated that the use of an appropriate basis set is critical to describe the electronic properties of the ground state for a vacant site in Chapter 4, we move on to address how to define local basis to describe the different structural images of a *NEB* calculation. As discussed in Figure 6.1, we have to keep in mind that the displacements of the vacancy requires a basis that adapts to the different localization of possible defect-related electronic states in each of the image structures of the migration path. Here, we will consider these specific scenarios:

- i) A naïve basis composed by a single *ghost* orbital placed at the initial position of the vacancy (and fixed at that position). As shown in Figure 6.2-(a) this setup will give a good description of that first *NEB* image, but not of the intermediate images. In particular, the final image configuration will have a vacant site with no support orbitals, while the initial position of the vacancy will have, in addition to the *ghost* orbitals, the basis orbitals of the migrating oxygen atom that moved to that site. It is easy to understand

that under these circumstances the total energy profile through the *NEB* path will be asymmetric, with a lower energy for the initial image as compared to the final (because the description of the electronic state will be worse in the latter), even though both structures should be energetically equivalent.

- ii) A possible better description could be obtained if the *ghost* orbital is displaced from the initial to the final position, in the same way as the moving vacancy (or migrating oxygen atom) is displaced through the *NEB* algorithm. In this way (panel b in the Figure 6.2), the initial and final configuration are equivalent, with one *ghost* orbital placed on the corresponding vacant site. However, this approach might pose problems for the *NEB* algorithm, as the positions of the *ghost* orbital must be kept fixed for each image at a position which is somewhat randomly defined. Typically, the center of the *ghost* orbital can be defined from an interpolation between the vacancy position in the initial, although it involves some arbitrariness. A simple linear interpolation, or a more elaborate scheme such as the *IDPP* (*Image Dependent Pair Potential*) method [Smi+14] can be applied. Furthermore, the intermediate images, and in particular the transition state, might be poorly described, as the two empty sites at the initial and final positions for the vacancy would have lower support basis coverage, while the migrating oxygen atom and the ghost orbital might be closely placed and prone to *over-completeness*. This might result in an inaccurate description of the transition state energy, and thus the energy barrier.
- iii) Using two fixed *ghost* orbitals at the initial and final vacancy positions might reduce the problems above (Figure 6.2-(c)). Now, both initial and final *NEB* images will have the same good description of possible localized defect states, and the transition state image will have a good support basis for the vacant sites. The main problem with this approach would be that there will be a large overlap between the (fixed) *ghost* orbitals and the basis of the moving specie (oxygen in our case) at the initial and final images. Note that this situation affects also the final state for the first case discussed above. Such approach can result in strong linear dependencies in the basis set (*over-completeness*), making the electronic structure convergence difficult. We alleviate these issues by defining

different Numerical Pseudo-Atomic Orbitals (NAOs) for the *ghost* orbitals and the orbitals of the *real* oxygen atom, so that Cholesky decomposition of the overlap matrix is stable. Alternative methods, such as the pivoted Cholesky decomposition could also be applied [Leh19].

- iv) A further possible improvement from the previous prescription can be obtained by adding a homogeneous distribution of *ghost* orbitals located along the migration path (Figure 6.2-(d)). Although this approach is also susceptible to over-completeness issues, it guarantees a good description of the whole *empty* space through-out the migration process. We defined the positions of the *ghost* orbitals from the initial *IDPP* images of the migrating oxygen atom, keeping fixed their centers through the *NEB* calculations.

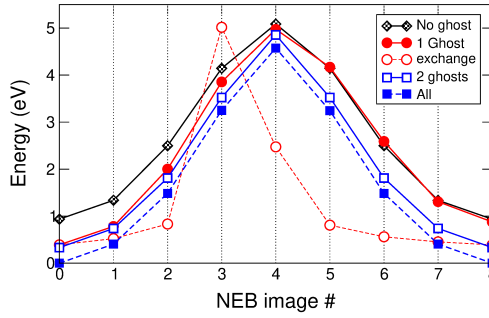


Figure 6.3: *NEB* migration barriers for V_O using different basis set descriptions. Red filled (empty) circles correspond to type *i* (*ii*); empty blue squares to type *iii* basis, and filled blue squares to *iv*. The energy of the initial state for the *iv* is taken as the origin. Calculations without any ghost orbitals are also included for comparison.

Figure 6.3 shows the migration energy profiles obtained with *NEB* using the different approaches to define the basis, and Table 6.1 reports the computed energy barriers. Results obtained with plane-wave codes and extracted from the literature can be used as a reference [El+18; MD11]. Note however that the use of different exchange-correlation functionals (or different pseudopotentials) tends to give rather different barriers.

From our data, it becomes clear that the use of a single *ghost* orbital (cases (*i*) and (*ii*)) gives a poor description of the migration path. As expected, the path is asymmetric, and the initial and final images have slightly different energies in

case (i) (~ 0.5 eV difference). The barrier is slightly overestimated in both cases, because the transition state geometry can be considered as a complex linear defect with an interstitial oxygen and two vacancies, which are not described with an adequate support basis (hence, the energy of that *NEB* image is higher than expected). Although the total energy for (iv) is lower than that with (iii), the results obtained for the barrier with both basis descriptions are very similar, and in excellent agreement with the energy barriers computed with plane-waves combined with Gaussian orbitals and PBE exchange-correlation [EL+18]. Note that when no *ghost* orbitals are included at all: a) the total energy of the system is almost 1 eV higher than the best basis description used, i.e. type (iv); b) the migration barriers is underestimated by ~ 0.5 eV, because the defect is not described correctly in that case. This effect is even stronger when the basis set is made of shorter orbitals (“*bad basis*” in the table). To understand this we need to analyse further the electronic structure of the defect in the transition state.

Table 6.1: Calculated energy barriers (in eV) using different basis set representations and for different defect charge states. Note that two barriers are reported for case (i), which correspond to *forward* and *backward* migrations in the asymmetric path shown in figure 6.3. Ref. [MD11] uses VASP (PW) and PW91 xc-functional while Ref. [EL+18] uses CP2K (Gaussian + plane-waves) and PBE functional.

	V_O	V_O^\bullet	$V_O^{\bullet\bullet}$
Without <i>ghost</i>	4.14	3.12	2.19
(i) With One <i>ghost</i>	4.58, 4.09	-	-
(ii) Exchange <i>ghost</i>	4.62	-	-
(iii) With Two <i>ghost</i>	4.52	3.54	2.29
(iv) All <i>ghost</i>	4.57	-	-
Longer Mg Basis	4.52	3.60	2.29
Without <i>ghost</i> “Short Basis”	2.29	2.30	2.33
Ref. [MD11]	4.81	3.68	2.38
Ref. [EL+18]	4.50	3.54	2.24

Figure 6.4 shows the projected density of states at the geometry of the *NEB* transition state, over the more relevant orbitals: the migrating oxygen atom (O_i , in blue), Mg orbitals closer to O_i (red), and the *ghost* orbitals if present (cyan). As mentioned before, the *TS* can be viewed as an interstitial oxygen in between two

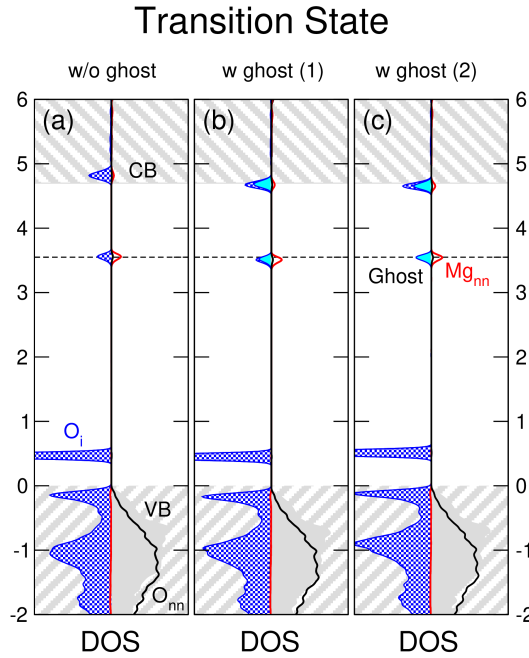


Figure 6.4: Projected Density of States around the electronic gap showing the defect level due to V_O . Panels (a)-(c) correspond to the Transition State geometry obtained with the *NEB* method. The valence and conduction bands are shown as striped grey areas, and the energy is aligned to the top of the valence band. Dashed horizontal lines are guidelines to the defect level position (the position of the Fermi level would depend on the whether the defect state is populated or depopulated). The projection on bulk Mg and O orbitals (far from the defect) are black and dark grey shaded areas, respectively. Black thick line corresponds to oxygen atoms that are close to the defect (O_{nn}), while red line is used for Mg next neighbors to V_O . The projection onto the *ghost* orbitals is plotted as shaded cyan regions in panels (a)-(c) to facilitate visualization. Panel (c) has two *ghost* orbitals placed in the initial and final positions for the migrating oxygen, but only the projection over one of them is plotted (both give similar contribution). For the Transition State panels, the PDOS for the migrating oxygen atom (which resembles an interstitial oxygen, O_i) is plotted as shaded blue also on the left subpanel.

vacant sites where electronic defect levels localize. Thus the oxygen orbitals can hybridize with the defect level and form bonding, non-bonding and anti-bonding

states within the gap of MgO. The sharp peak above the top of the valence band is due to migrating oxygen's $2p_z$ orbitals (perpendicular to the plane defined by the two vacant sites and the two Mg atoms first-neighbours to O_i). The next state, which is doubly occupied in the neutral V_O configuration, has bonding character and involves both defect states coming from the vacant sites. In principle, as we discussed before, *ghost* orbitals are needed to properly describe these states, but there is also some contribution from near Mg atoms. If there are no *ghost* orbitals, then polarization d orbitals from O_i are borrowed to describe this defect level (p orbitals would not be allowed by symmetry). The corresponding anti-bonding state, which is unoccupied and just below the conduction band, has mainly contributions from the *ghost* orbitals (when present), and from $O_i - 2p$ orbitals. Structurally, the geometries obtained with *ghost* and without *ghost* are very similar, because the electronic structure of the defect states at the *TS* can be sufficiently described with the orbitals of the moving O_i . With this in mind, the underestimation of the energy barrier when no *ghost* orbitals are included in the basis should be attributed to the poor description of the initial defect configuration, and not to the *TS* itself.

The barriers reported in table 6.1 for V_O^\bullet and $V_O^{\bullet\bullet}$ using different basis orbitals do not include the charge correction schemes, but highlight that there is a strong dependence of the migration barrier with the population of the defect state. The barrier decreases almost by a factor 2 when going from the neutral vacancy to V_O^\bullet . Note that the dependence of the barrier with the basis is strongly suppressed for $V_O^{\bullet\bullet}$, when the defect level is completely unoccupied. Obviously, in this case the need for a good description of the localized defect level is not critical. Special consideration is needed for a “Bad Basis” which has very short-range orbitals and does not include any ghost orbital. In this case, we found no dependence of the barrier with the defect state population, basically because this basis is not even capable of describing the existence of the defect level!

6.2 Comments on localized charge correction and BSSE

Following the correction scheme described in chapter 3, we calculated the total energies required for the initial and *TS* images for V_O^\bullet and $V_O^{\bullet\bullet}$. We just considered the basis type (iii), as it seems to give a sufficiently good description of the migration. We used both the Gaussian model and the ρ approach and the results

for total correction, in barrier value and corrected barrier are presented in Table 6.2. Although the total correction on the formation energy can be relatively large (of the order of 250 and 780 meV for V_O^\bullet and $V_O^{\bullet\bullet}$ respectively), we see that the effect on the barrier is small. In other words, the correction at the initial image is similar to the correction at the TS image. The effect is similar for the Gaussian model, although of opposite sign, which might be reminiscence of the different localization of the defect state at both images.

Table 6.2: The Correction on calculated energy barriers (in eV) for different defect charge states using Two *ghost* basis system

	V_O^\bullet with ρ	$V_O^{\bullet\bullet}$ with ρ	V_O^\bullet with Gaussian	$V_O^{\bullet\bullet}$ with Gaussian
Correction [eV]	0.03	0.04	-0.02	-0.04
Barrier Corrected [eV]	3.57	2.33	3.52	2.25

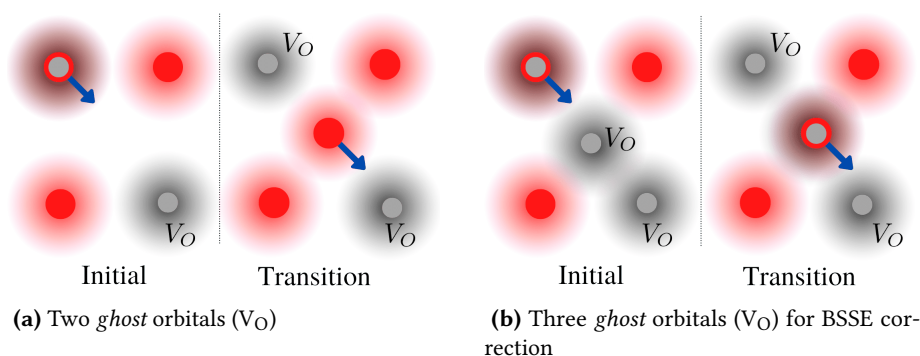


Figure 6.5: Scheme of the BSSE correction we consider for NEB barriers. The V_O and O species are represented by gray and red colors, respectively. The shadows with a gradient represent the basis of each species. (a) two *ghost* orbitals are included at the initial and final positions of the migration. At the transition state the moving oxygen is placed in-between the ghosts. (b) For calculating the BSSE the energy of the initial image is recomputed with an additional *ghost* orbital placed at the position that the moving oxygen occupies at TS.

Finally, to close the chapter we address the last question raised at the beginning of the chapter, regarding the *Basis Set Superposition Error* (BSSE). Figure 6.5-(a)

shows the schematic of the problem, in particular for the basis type (iii). In the initial image, there are two *ghost* orbitals, one placed at the position of the vacancy, and a second placed at the same site than the moving oxygen atom. At the transition state, however the support basis orbitals are placed at different sites, essentially because now the moving oxygen is at the TS. Thus, the basis coverage seems to be better in this configuration than in the initial. To correct for this effect, we can add one extra *ghost* orbital site at the interstitial site also for the initial image, as shown in Figure 6.5-(b). In this case, the basis set used for both initial and TS will be the same, and we avoid the *BSSE*. The difference between the two initial images and the difference between the two TS images in panels (a) and (b) of the figure, gives 0.06 eV and 0.11 eV respectively. The barrier in (b) is reduced to 4.47 eV as compared to (a). The difference in the barrier energy between both approaches gives us an estimate for the *BSSE*, which in this system is of ~ 0.05 eV, and can be considered of the order of the error bar for the energy barrier. In the future it might be interesting to evaluate the *BSSE* for other barriers.

6.3 Computational Details

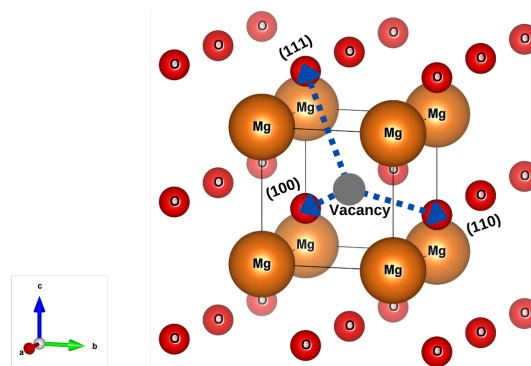


Figure 6.6: V_O Migration Path in $\langle 110|110 \rangle$ MgO FCC Structure

The *NEB* method was implemented in SIESTA within a LUA interface framework [Gar+20b]. For our calculations we used the PBEsol [CFD11a] exchange-correlation functional form of the generalized gradient approximation. Well converged and tested pseudopotential from pseudo-dojo vault [Gar+18] were

used. A mesh cutoff of 750 Ry is used to perform real space integrals in SIESTA, and the reciprocal space sampling density is equivalent to $6 \times 6 \times 6$ Monkhorst-Pack grid in the unit cell. The simulation cell is $3 \times 3 \times 3$ unit cells of MgO (216 ions) and was relaxed until the forces converge with a tolerance below 0.04 eV/Å. The obtained relaxed structure was used to construct the images for calculating the migration pathway for NEB along the $\langle 110|110 \rangle$ direction (an oxygen atom moves along the $\langle 110|110 \rangle$ direction into the vacancy) as shown in Figure 6.6, which is known to give the minimum energy barrier. A total of 8 images were considered, and the spring constant was 5.0.

6.4 Conclusions

In this chapter we used the tools to compute migration barriers for defect in crystals using the SIESTA package, and developed a general framework to set the specific input parameters required. In particular, we focused on the following aspects:

- (i) Basis sets, and the need to include *ghost* orbitals to describe vacancies in crystals. We showed that a scheme in which two *ghosts* placed at the initial and final positions of the vacancy are enough to describe the electronic properties of the migration path.
- (ii) The *ghost* orbitals are more important to describe properly the initial/final configurations than the Transition State itself. The orbitals from the migrating atom (in our case the moving oxygen) are sufficient to describe the electronic properties of this configuration, and the sensitivity of the barrier to the basis used comes from the reference initial state.
- (iii) For charged vacancies we confirmed a strong sensitivity of the barrier with the occupation of the defect level. Although the correction schemes that take into account the long-range electrostatic interactions in periodic boundary conditions can be important for defect formation energies, we observed that the effect on the migration energies is small.
- (iv) We proposed a scheme to estimate the *Basis Set Superposition Error* in NEB calculations with localized atomic orbitals. The estimated value for the system under consideration is sufficiently small that can be safely

neglected. However, further investigation for other systems would be needed



Part IV

Surfaces & Interfaces

Physical phenomena explicitly linked to condensed matter surfaces have been studied for centuries. Surfaces are the first frontier when studying matter and as such they are scenarios for a number of novel physical and chemical effects, including friction, molecular absorption, surface plasmons, heterogeneous catalysis, surface electronic states, electric and magnetic deadlayers, etc. These phenomena has attracted significant interest, both from the fundamental scientific questions they pose and the need to control these properties for applications of the materials. Thus many experimental techniques have been developed over the years to study surfaces, from surface X-ray scattering, to Auger or X-ray photoelectron Spectroscopy, Low-Energy Electron Diffraction, Surface Enhanced Raman Spectroscopy, the scanning probe microscopies in its many different flavors, etc. Similarly to the experimental efforts, from the theoretical perspective we also need adequate tools to explore the phenomena that arise from surfaces. This chapter explores the methodologies and concepts for defining a crystal surface, and studying its electronic and structural properties, in particular, making use of the SIESTA package.

7.1 Surfaces

7.1.1 Types of Surfaces

The use of periodic boundary conditions in most DFT codes, poses a problem when studying surfaces, which can be circumvented as we did for point defects. The problem as in that case, is that the surface breaks the translational symmetry of the crystal along the surface normal direction. For defects, we had to use a supercell, so that the interactions between periodic images is minimized. For surfaces instead we use a slab structure, which keeps periodicity on the plane of the surface, and includes enough vacuum region to avoid interactions with the periodic images. Such slabs are built from the bulk structure, including a specific number of unit repetitions along the desired non-periodic direction. The thickness of the slab is determined by the number of repetitions, and the idea

is that the properties of the bulk crystal are reproduced at the center of the slab. Note that these model slabs include not one but two surfaces. To define them one needs to specify the specific surface orientation relative to the crystal coordinates, and the chemical composition at the termination.

Structural features at the slab termination, and possible atomic relaxations require special attention. Surface formation by cleavage leads to broken bonds on the surface, and a highly unstable atomic arrangement. This induces considerably large elastic and chemical energies, the creation of charged or polar layers, all of which can result on surface *reconstruction*, with strong structural relaxations that are required to facilitate formation of new bonds. When we have surfaces where the relaxation of the atomic positions of the exposed boundary are small, we talk of an *ideal surface*.

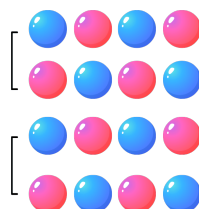


Figure 7.1: The Type-*I* Non-Polar termination of the surface

Among various classifications for surfaces, we follow Tasker's notation [Tas79] which is based on electrostatic arguments according to whether the layers are charged and the structural repetition unit bears a dipole moment or not. There are three types of surfaces that can be distinguished.

- Type-*I* surfaces are usually the most stable, with no net charge nor dipole moment in the unit cell ($Q = 0$ and $\mu = 0$), as shown in Figure 7.1.
- Type-*II* surfaces involve charged layers ($Q \neq 0$) but no dipole moments ($\mu = 0$), as illustrated in Figure 7.2. The unit cell can be of type IIa, as in the figure, where the anions and cations comprising the layers are not coplanar, but which allows for some surface cuts to split the layers in such a way as to produce no dipole; alternatively, in type IIb termination, some ions at the top surface must be moved to the bottom to remove the dipole.

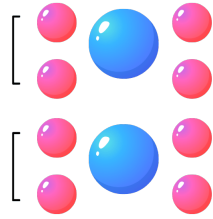


Figure 7.2: Type-II Non-Polar termination of the surface

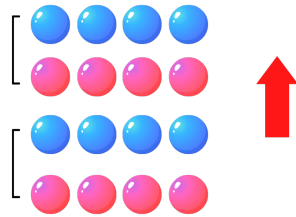


Figure 7.3: The Type-III Polar termination of the surface

- Type-III (polar surfaces) this surface, as opposed to Type-I surfaces, experience a strong electrostatic instability due to the presence of a net dipole moment ($\mu \neq 0$) in the repeat unit and electric charge in layers ($Q \neq 0$), Figure 7.3.

7.1.2 Surface Energy

To describe the stability of a surface we define the surface energy γ , which is a measure of the energetic cost to create the surface. This energy is due to a variety of factors, including bond breaking that yield undercoordinated atoms, or the removal/addition of atoms that change the stoichiometry of the system. Surface energy is a fundamental quantity to understand the surface structure, reconstruction, roughening, and the crystal's equilibrium shape. Typically γ depends on the surface orientation and chemical composition, and should be defined for a given surface orientation. Thus, we label it γ_{hkl}^σ for a specific facet

with Miller index (hkl), and compute it with a slab model using the following expression: [Tra+16]

$$\gamma_{hkl}^{\Lambda} = \frac{E_{slab}^{hkl,\Lambda} - (E_{bulk}^{hkl} \times n_{slab})}{2 \times A_{slab}} \quad (7.1)$$

Here $E_{slab}^{hkl,\Lambda}$ is the total energy of the slab with termination Λ , E_{bulk}^{hkl} is the energy per atom of the bulk unitcell oriented along the slab direction, n_{slab} is the total number of atoms in the slab structure, A_{slab} is the surface area of the slab and the prefactor 2 accounts for the two surfaces in slab (assuming the slab was built with equal termination on both sides).

7.1.3 The Workfunction

The Workfunction is the energy required to remove an electron from the solid and place it at infinity. The final electron position is far from the surface on the atomic scale but still too close to the solid to be influenced by ambient electric fields in the vacuum. In physics, the term work function is frequently used to represent the energy of electrons in metals.

$$\Phi = E_{fermi} - \langle V_{hartree} \rangle \quad (7.2)$$

in *DFT* the $\langle V_{hartree} \rangle$ is chosen as vacuum level. To compute the workfunction we need to calculate the electronic potential in a slab geometry, and determine the value of $\langle V_{hartree} \rangle$ in vacuum, far from the slab. This value, and the value for the Fermi level in slab are then used in Eq 7.2.

7.2 Surfaces Electrostatics

Regarding the electrostatic of the slab model we have to take into account two critical aspects which are intertwined [MV01a]:

- Issue (i): The appropriate boundary conditions for the electrostatic potential in the polarized state.
- Issue (ii): The effect of the periodic boundary conditions on the electrostatic potential.

In an isolated slab with a polarization perpendicular to the surfaces,⁸ the polarized slab exhibits an electric dipole moment

$$m = \int_{-\infty}^{\infty} \bar{\rho}(z) z dz \quad (7.3)$$

normal to the surface, where $\bar{\rho}(z)$ is the planar averaged charge density

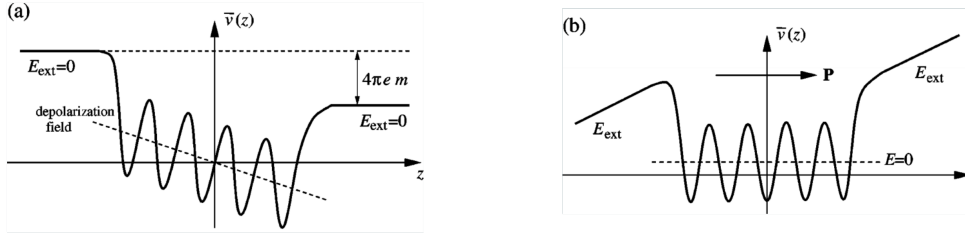
$$\bar{\rho}(z) = \frac{1}{A} \iint_A \rho(r) dx dy \quad (7.4)$$

and A is the area of the surface unit cell. The electrostatic potential $v(r)$ experienced by the electrons can be calculated by solving the Poisson equation

$$\nabla^2 v(r) = 4\pi e \rho(r) \quad (7.5)$$

But the external boundary conditions determine the solution that we obtain.

7.2.1 Issue (i): Isolated Boundary Conditions



(a) Vanishing external electric field equivalent to $D = 0$.

(b) Vanishing internal electric field $E = 0$.

Figure 7.4: Schematic illustration of the planar-averaged potential $\bar{V}(z)$ for an isolated slab with a dipole moment m perpendicular to the surface. (Figure is taken from [MV01b]).

We can distinguish two cases depending on whether there is a vanishing

- 8 We choose the surface normal \hat{n} to be parallel to the z axis, and we assume the charge density $\rho(r)$ of the slab to be periodic in the x and y directions.

external electric field, $E_{ext} = 0$ as in Figure 7.4, or a net electric field is present, $E_{ext} \neq 0$. In general, when determining the properties of free surfaces, we are mainly considering the case where $E_{ext} = 0$. The dielectric displacement field \mathbf{D} inside the slab must be oriented parallel to the z axis and be equal to E_{ext} (easily derived from the interfacial boundary conditions when there is no unbound charges at the surface, $(\mathbf{D}_{in} - \mathbf{D}_{ext}) \cdot \hat{n} = 0$). The polarization of slab \mathbf{P} leads to surface bound charges $\sigma = \mathbf{P} \cdot \mathbf{n}$, which create an internal depolarization field $\mathbf{E} = \mathbf{D} - 4\pi\mathbf{P} = -4\pi\mathbf{P}$ inside the slab⁹. The main consequence is that, although the potential in vacuum is flat, there is a jump between both sides of the slab, which depends on the dipole m . This comes with a problem when using periodic boundary conditions, as we will discuss next.

7.2.2 Issue (ii): Periodic Boundary Conditions

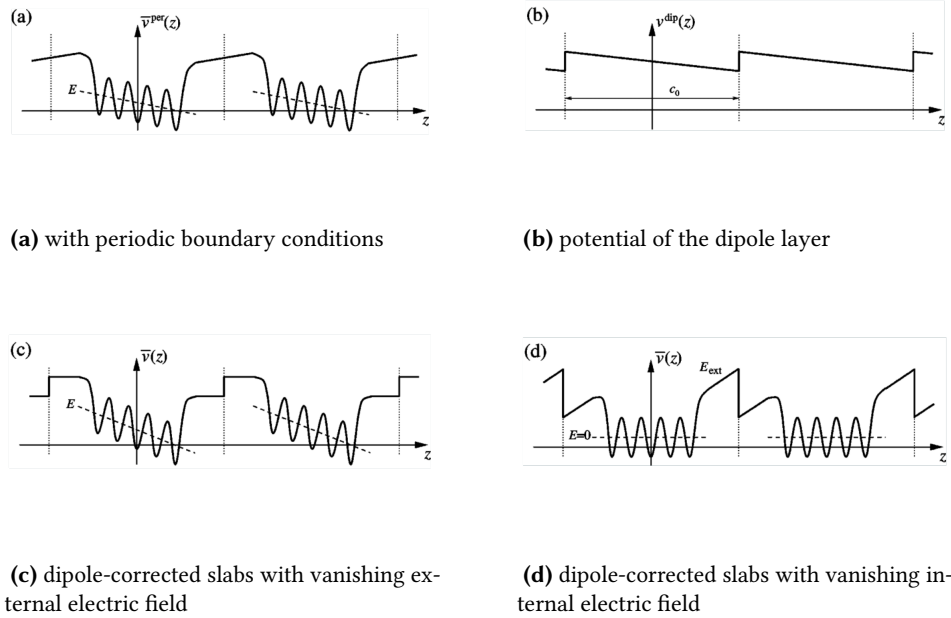


Figure 7.5: Schematic illustration of the planar-averaged potential $\bar{V}(z)$ for repeated slab with a dipole moment m perpendicular to the surface. (Figure is taken from [MV01b]).

In supercell calculations, with periodic boundary conditions, if the slabs have

⁹ E does not depend on the thickness of the slab

a non-vanishing dipole moment perpendicular to the surface, the electrostatic potentials typically look like Figure 7.5-(a). This potential profile does not correspond to the scenario in Figure 7.4 because there is an artificial external electric field in vacuum. The strength of this field depends on the thickness of the vacuum region included in the supercell, decreasing for larger supercells. The way to remove this external field is to introduce an external dipole layer in the vacuum region of the supercell, [Ben99; NS93] which gives rise to a compensating electric field of opposite direction, as shown in Figure 7.5-(b). The sum of both potentials (a+b) results in a potential profile like the one shown in Figure 7.5-(c) which has the flat behaviour in the vacuum region. This approach also allows to play with different electrostatic boundary conditions, and by properly setting the strength of the external dipole we can, for example, completely cancel the internal electric field in the slab, Figure 7.5-(d), while keeping a polarized solution (i.e. we can define a non-zero displacement field $D = E_{ext}$). This method is particularly useful when studying ferroelectric slabs.

The external dipole field correction is available in SIESTA. It calculates the electric field required to compensate the dipole of the system at every iteration of the self-consistent cycle. The potential added to the grid corresponds to the dipole layer in the middle of the vacuum layer. For slabs, this exactly compensates the electric field at the vacuum created by the system's dipole moment, thus allowing the treatment of asymmetric slabs (including systems with an adsorbate on one surface) and computing properties such as the work function for each of the two surfaces in the slab.

7.3 Heterostructures

Generally, a heterostructure is a composite structure in which more than one material combine to form a new system (Figure 7.6). The interface can be thought as the superposition of the surfaces of the different materials combined, and has unique properties which might be very different from those of the constituents. Physical phenomena such as one-way injection, superinjection, electron confinement, optical confinement,... happen at interfaces. Historically the idea of using heterostructures emerged at the very beginning of electronics. We can think of the **p – n** junction in transistors as a major breakthrough that comes from specific properties of heterostructures: The idea proposed by Shockley is used to achieve one-way injection in a wide-gap emitter [Bon].

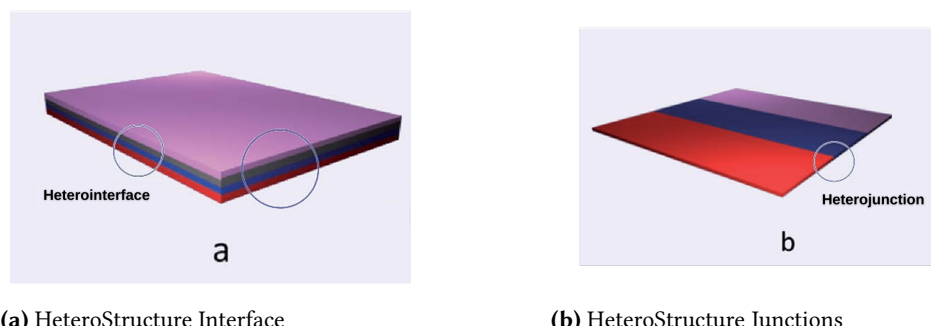


Figure 7.6: Schematic view of different Heterostructure. (Figure is adapted from [Das+18]).

This was the beginning of the classical era semiconductors technology, which has evolved into a new quantum era with the miniaturization of electronic devices and confinement of electrons. New quantum phenomena arise, which require investigations, and quickly open new research topics that need new code developments. Two-dimensional electron gas, the quantum Hall effect, and the existence of excitons at room temperature are just a few of many examples that emerged in the last few decades [Alf96].

To study heterostructures we must consider that the lattice parameters of the two materials might be different. Commensurability can be imposed by choosing appropriate supercells for each material component so that the heterostructure satisfies lateral periodicity under a moderate level of strain. Once the geometry is defined under periodic boundary conditions, and the structure is relaxed, we can determine the electronic structure, and extract the relevant band characteristics, and in particular the electronic Levels Alignment or the Band Offsets between the two materials.

7.4 Implementation of Sisl ToolBox Siesta Surfaces and AiiDA Siesta Surfaces

I develop surface generation in two separate packages:

- **Sisl ToolBox Siesta surfaces:** is a python package tool inside the Sisl toolbox to generate different slab surfaces and thicknesses to found most stable

face and other properties such as workfunction. To see the manual one could access to web page : <http://zerothi.github.io/sisl/docs/latest/index.html>

- **AiiDA Siesta Surfaces** : is a python package to automate to generate and calculate different slab surfaces and thicknesses to found most stable face and other properties such as workfunction with siesta through the AiiDA platform. To have access to the workflows and manual one could reach to web page : <https://github.com/siesta-project/aiida-siesta-surfaces>

In the following chapter, we will show how these packages can be combined with the tools developed to study defects, and illustrate their usage to address the simulation of the electronic properties of defects at the interface of an hybrid nanostructure: carbon nanotubes functionalized with HfO_2 nanoparticles.

7.4.1 The problem of localized basis set

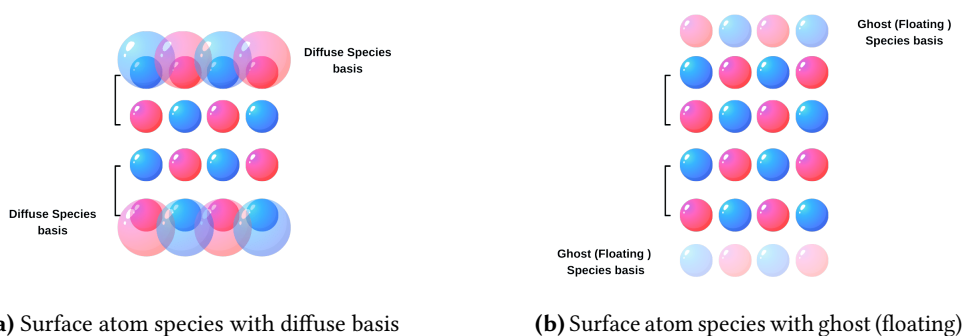


Figure 7.7: Schematic view of different schemes for basis sets for the surface

One particularity of SIESTA is the short localization of the atomic orbitals. We addressed this issue when studying vacancy defects in previous chapters, but in surfaces the problem is enhanced, as in vacuum there are no support basis functions that can describe dispersive surface electronic states. In a previous study, Gil et al. [Gar+09a] explored methodologies to enhance the NAO basis sets for the surface atoms to accurately describe surface electronic states and extract properties such as surface energies and work functions. They showed that augmentation of the local orbitals with either a shell of diffuse orbitals in the surface atomic layer ,Figure 7.7 (a), or with one or two shells of floating

orbitals in the vacuum region, Figure 7.7 (b), gives a dramatic improvement both in the estimate of surface energies and in the description of the wavefunction's decay into vacuum.

We have considered these methodologies in the implementation of Sisl ToolBox Siesta Surfaces and AiiDA Siesta Surfaces Package when constructing the models to simulate slabs.

High permittivity (high- k) materials have attracted a great deal of interest in the semiconductor industry as they are needed as ultrathin dielectric gates in MOSFET technologies. Among the many possible candidate materials, HfO_2 with its relatively high-dielectric constant, wide bandgap, high thermal stability, and low leakage current has been a strong player [Lia+10a; Lia+10b; Mer+08; Rob+10; Rot+22; ZHZ11]. More recently, the fast implantation of graphene applications has triggered substantial research for good dielectrics that are compatible with carbon-based electronic devices. [KJ13]. These new hybrid materials, made of an organic component, which is abundant and more bio-compatible, and non-carbon-based material (inorganic) are versatile for many applications and their combination can produce novel distinct properties. In this line, the combination of HfO_2 nanoparticles and carbon nanotubes (CNT) has recently shown unusual visible photoluminescence, and optoelectronic properties [Rau+17b] that make these hybrid materials of interest for energy generation and storage. Experiments suggest that the properties of these materials are strongly affected by defects that are present close to the surface of the material [Rau+; Rau+12; Rau+17a; Rau+19a; RGR15; RR14].

Motivated by these experimental observations, in this chapter we exploit the tools developed to study surfaces and interfaces to explore the effect of defects on HfO_2/CNT nanocomposites. In particular, we focus our study on a model system of the $\text{HfO}_2(111)/\text{Graphene}$ hybrid nanostructure and the effects of oxygen and carbon vacancies on its electronic properties. The structure of the chapter is the following. First, we calculate the stability of low index surfaces for cubic HfO_2 and explore the properties of an isolated oxygen vacancy on the system. Next, we build a heterostructure between HfO_2 and Graphene, and analyse the electronic structure, paying attention to the possible charge transfer effects. Finally, we explore the effects of defects (vacancies of oxygen and/or carbon) and their role in bonding, Fermi level pinning and charge transfers.

8.1 (100),(110),(111) surfaces in cubic HfO_2

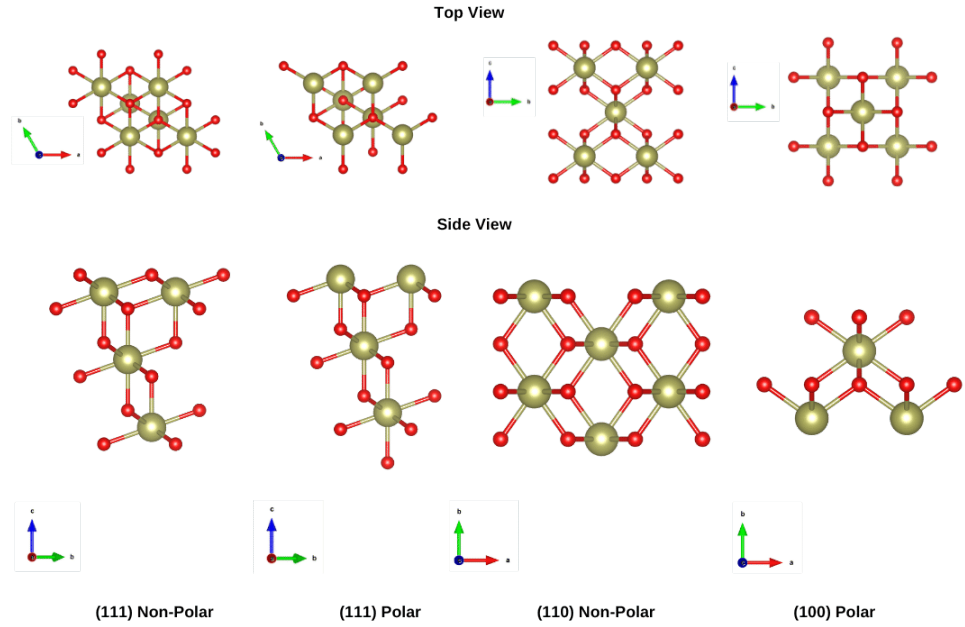


Figure 8.1: classifying the low-index surfaces of cubic HfO_2

HfO_2 has various crystalline phases [Ala+21], from monoclinic (the most stable at low temperatures) to tetragonal, to cubic, including several orthorhombic phases. Usually, dopants are introduced to increase the stability of the cubic phase at room temperature, as this phase has a larger permittivity than the monoclinic phase. The introduction of divalent or trivalent dopants has been linked to an increased number of oxygen vacancies. However, it has been shown that synthesized nanoparticles with diameters of around 2.6 nm can also be stabilized in the cubic phase without introducing dopants, [Rau+12] which is advantageous as these impurities also modify the electronic properties of HfO_2 . The stabilization of the cubic phase in the nanoparticles has also been rationalized in terms of an increased number of oxygen vacancies at the nanoscale. These vacancies have also been linked [RR14] to the nanoparticles photoluminescence at photon energies well below the bulk band gap ($E_g \sim 5.7$ eV). Thus, we focus here on the cubic phase and its heterostructure with graphene, as a simplified

model for a wide diameter carbon nanotube (i.e. the hybrid structure described in the experiments from P. Rauwel and coworkers[Rau+19b]).

We first analyze the stability of HfO_2 surfaces, calculating the surface energy for different low-index orientations and terminations. In particular, we addressed polar and non-polar slabs cut along (111), (110) and (100) directions, illustrated in Figure 8.1. The computed surface formation energies (σ) as a function of the thickness of the slab (i.e. number of layers used to build the surface model), are plotted in Figure 8.2, and show a fast convergence for relatively thin slabs. We note that $\text{HfO}_2(111)$ has the lowest formation energy and $\text{HfO}_2(100)$ the highest, thus justifying that we focus on the following in the (111) orientation as the most representative case.

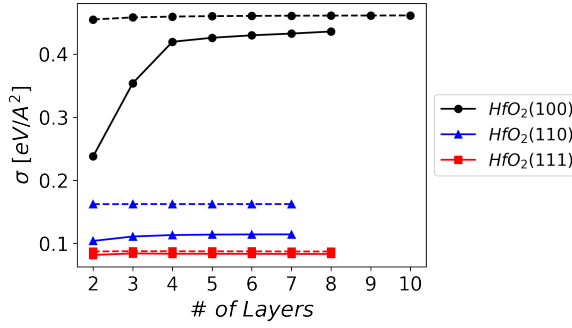


Figure 8.2: Surface Formation Energy of all low-index surfaces of cubic HfO_2 . The solid and dashed lines correspond to relaxed and unrelaxed structures.

8.2 Oxygen Vacancy in $\text{HfO}_2(111)$

We take the $\text{HfO}_2(111)$ slab model with eight layers ($\approx 21.87 \text{ \AA}$) and create $2 \times 2 \times 1$ lateral supercell to study the properties of oxygen vacancies. This thickness is sufficiently large to recover bulk-like properties at the center of the slab, and the lateral dimensions of the 2×2 supercell are similar to the ones used to study defects in bulk in chapter 4. We calculate the pristine slab, the slab with neutral oxygen vacancy in the center of the slab ($V_{\text{O}}^{\text{center}}$), and the slab with a neutral oxygen vacancy at the surface ($V_{\text{O}}^{\text{surface}}$). We also checked that the formation energy for the neutral vacancy at the center of the slab is in good agreement with that of a bulk structure, which proves that the model

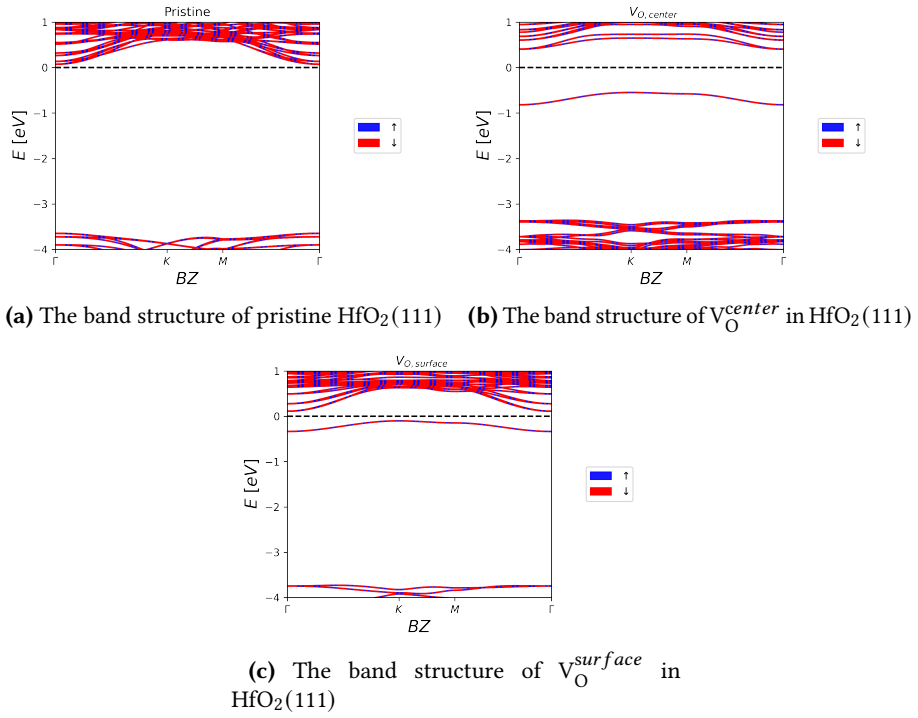


Figure 8.3: The Band Structure of $\text{HfO}_2(111)$ with neutral oxygen vacancy in center and surface of the slab

thickness is appropriate. Although the energy of the unrelaxed structure for the vacancy in the center of the slab (bulk-like) is about 0.5 eV lower than the vacancy at the surface, upon structural relaxation there is an energy gain that favors energetically the vacancy at the surface (formation energies of 6.78 eV and 6.58 eV for $V_{\text{O}}^{\text{center}}$ and $V_{\text{O}}^{\text{surface}}$, respectively). This goes in the line of an increased stability of oxygen vacancies in nanoparticles, where the surface to bulk ratio is larger, which can explain the formation of the nanoparticles with the cubic phase.

Figure 8.3 shows the band structure of the pristine slab, together with those of the slab holding a vacancy in the center and at the surface. An occupied defect state is clearly visible in the gap. However, the position of the defect level depends on the position of the vacancy within the slab, being pinned

near the bottom of the conduction band when the defect is at the surface layer (note however that the DFT gap is substantially underestimated with respect to the experimental one). Therefore, the $V_{\text{O}}^{\text{surface}}$ has an electronic level almost 3 eV above the top of the valence band, which is in reasonable agreement with the PL emission at 3.1 eV reported for cubic nanoparticles [RR14]. Figure 8.4 plots the $p\text{DOS}$ of the defective slab structures, showing that the new electronic state is localized mostly at the ghost orbitals, with some additional weight on neighbouring Hf atoms.

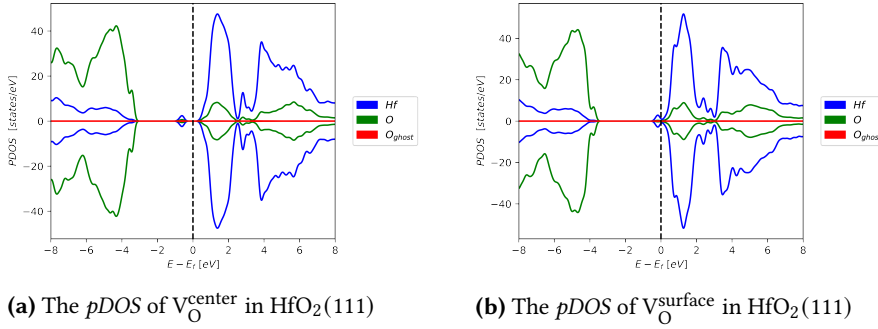


Figure 8.4: The $p\text{DOS}$ of $\text{HfO}_2(111)$ with neutral oxygen vacancy in center and surface of the slab

8.3 Graphene on cubic $\text{HfO}_2(111)$ surface

Multiwall carbon nanotubes (CNT) functionalized with cubic- HfO_2 nanoparticles, as synthesized by Rauwel and collaborators, [Rau+16] have been shown to be promising nanocomposite material for light harvesting applications. The optical properties of the oxide nanoparticles combine with the conducting and flexible properties of the nanotubes, showing photocurrent generation under UV-vis illumination. The attachment of the nanoparticle to the sidewalls of the nanotube seems to be related to the presence of defects in the graphitic structure, most likely C dangling bonds. On the other hand, the optical properties are closely linked to the presence of defects on the surface of HfO_2 . Upon illumination, the photocurrent presents a rapid response, with an initial spike due to filling and discharging of the defect states, followed by a stable photoresponse that suggests that photogenerated electrons are easily transferred to the CNT. Using

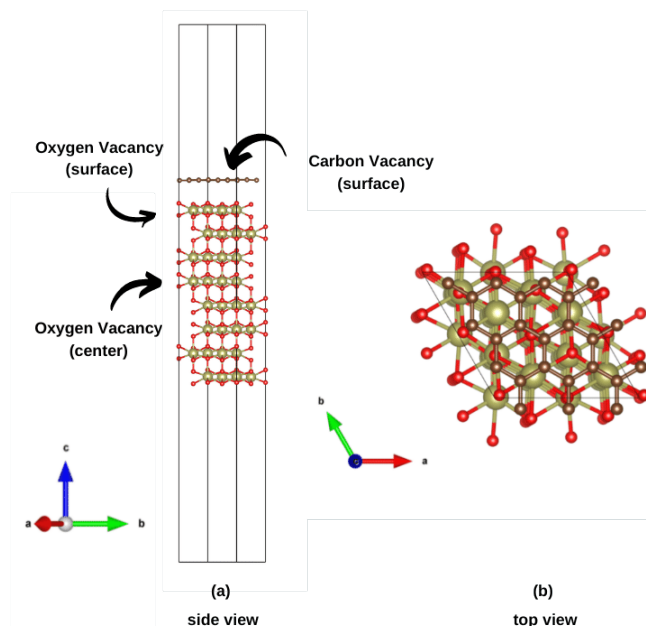


Figure 8.5: The Structure of HfO₂/Graphene from (a) side and (b) top view. The vacancy position is either on the surface of HfO₂ or in the center where the region is bulk-like. The carbon vacancy is located on top of oxygen, where we created the vacancy in the surface of HfO₂.

our simulation tools for this heterostructure and studying the effect of point defects on the electronic properties is the objective of this section.

Modeling the nanoparticle+CNT is beyond reach of DFT calculations (the average diameter of the CNT is around 10 nm), thus we introduce a simplified system to study the heterostructure: a slab of HfO₂ interfaced to a graphene monolayer, which can be a good approximation for large diameter nanotubes. The lattice mismatch between HfO₂ and graphene can be handled using the $2 \times 2 \times 1$ HfO₂ supercell and a 3×3 graphene cell (mismatch $\sim 4.0\%$), with a modest strain applied to the later so that the cubic phase of HfO₂ remains stable. The effect of this strain on the graphene bandstructure in this case is sufficiently small. Indeed, Kamiya et al. [KUO11] investigated the hybrid structure of graphene absorbed on pure cubic HfO₂(111) surface (HfO₂(111)/G) using LDA for the exchange-correlation and a similar in-plane superlattice. They found a slight

modification of the graphenes linear bands close to the Dirac point due to the interaction with HfO_2 and ascribed the origin of this change to the hybridization of the π states from graphene with the mixture of $\text{O} - p$ and $\text{Hf} - d$ states from the substrate. To our knowledge, there is no bibliography on the effect of defects over the electronic properties of this hybrid structure.

To explore the binding of Graphene with $\text{HfO}_2(111)$ we monitor the energy of the hybrid system as a function of the interlayer spacing between them in the pristine and defective systems. Upon structural relaxation, and in agreement with the results reported by Kamiya, the optimal interlayer distance is close to 3 \AA and the binding energy is of about 100 meV per C atom. Table 8.1 collects the effect of different defect types on the binding energy between both systems. We considered four different scenarios: (i) an oxygen defect in the center of the slab; (ii) the oxygen vacancy on the surface at the interface with graphene; (iii) a carbon vacancy in graphene; and (iv) both oxygen vacancy on the surface and carbon vacancy in graphene. It can be seen that while oxygen vacancies reduce the binding energy, the presence of carbon vacancy in graphene increases the binding energy. Thus, an enhanced adhesion of HfO_2 nanoparticles to defective carbon nanotubes can be confirmed, in agreement with experimental suggestions. Having both carbon vacancy and surface oxygen vacancies increases this effect dramatically, as the interaction between the electronic states linked to both defects is strong, as we will discuss in the following.

Defect	Binding Energy [meV/C atom]
Pristine	102
$V_{\text{O}}^{\text{surface}}$	65
$V_{\text{O}}^{\text{center}}$	89
V_{C}	145
$V_{\text{O}}^{\text{surface}} \& V_{\text{C}}$	340

Table 8.1: Binding energy per carbon atom for (i) the oxygen defects on the center of the slab, (ii) the oxygen defects on the surface of the slab, (iii) the carbon defect in graphene and (iv) the oxygen defects on the surface of the slab and carbon defect in graphene.

The band structures for the different systems modeled are plotted in Figure 8.6. These fatbands contain information on the weights that the different orbitals

in the basis set have on the eigenenergies of the heterostructure, $\epsilon_{i,k}$, and can be used to quickly distinguish the character of the different bands. In particular, here we are interested in highlighting graphenes bands over HfO_2 band structure. For the pristine hybrid heterostructure our results are in good agreement with the work by Kamiya et al. [KUO11]. The linear dispersive bands of graphene appear within the large band gap of HfO_2 , and the Dirac point is clearly distinguished (note that is bandfolding due to the use of a supercell).

The Fermi level is pinned at the Dirac point, and evidences that there is no charge transfer between graphene and HfO_2 . When there is an oxygen vacancy in the center of the slab, the bandstructure resembles the combination of the features obtained for the defective slab (with a localized defect level below the Fermi level) and the pristine heterostructure with graphene, with its clearly identifiable Dirac cone. However, there is a slight shift in the position of the Dirac cone, due to a small charge transfer from the defect level towards the carbon monolayer. This effect is further enhanced when the oxygen vacancy is at the surface (interface with graphene), where there is a clear transfer of charge from the vacancy level towards graphene, leaving a spin-polarized defect with magnetic moment of $0.45 \mu_B$. Thus we can confirm that the presence of oxygen vacancies on HfO_2 nanoparticles favors the extraction of possible photogenerated carriers through the carbon nanotubes, as reported in the experiments.

Introducing carbon vacancies in this relatively small supercell (which is equivalent to modeling a high concentration of impurities in the system) induces a strong structural deformation on the graphene monolayer, and enhances the hybridization with the substrate. This results in a strong modification in graphene's bands, as shown in Figure 8.6-(d). There is also an opening of a gap in the Dirac cone ($\delta \sim 0.2 \text{ eV}$), and a defect level above the Fermi level (flat band at around 0.8 eV). Previous calculations of vacancies in free-standing graphene show both localized σ and semilocalized π defect levels [RPP16], which are spin polarized and give a net magnetization induced by the defect [Ma+04]. We expect that the interaction with the substrate can shift the energy of these states, and in our calculations the spin magnetization is lost. However our supercell is too small to describe isolated vacancies, and we can not clearly identify σ states due to the strong modification of the graphene structure. Nevertheless, we believe that the increased binding between the oxide and the carbon nanostructure can be understood in terms of the electronic structure, with π defect levels from the vacancy interacting strongly with the surface, proving that defects on carbon

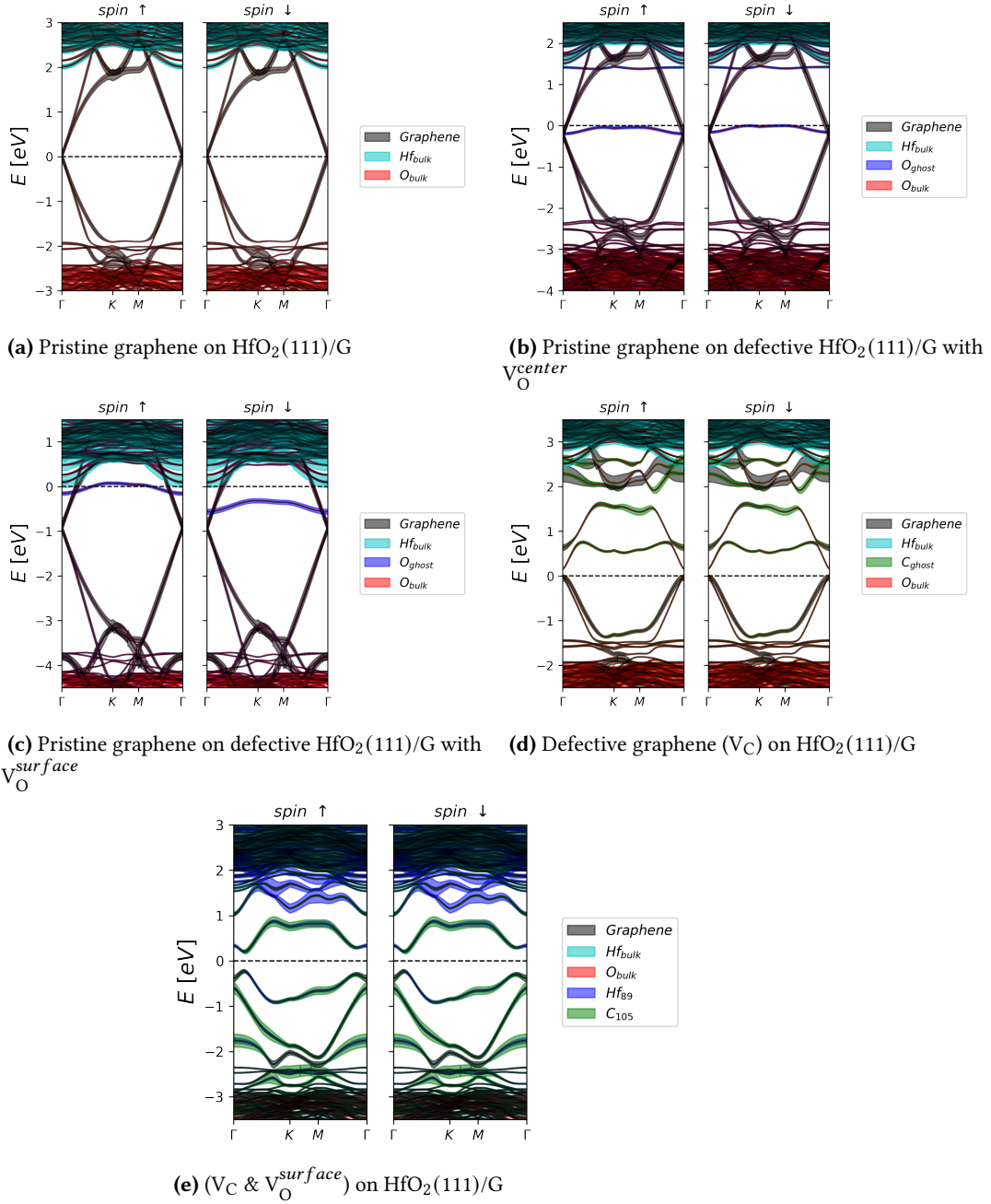


Figure 8.6: The *fatBands* of hybrid HfO₂(111)/Graphene heterostructures with different types of vacancies. The weights on the different chemical species on the character of each electronic state (band) is plotted with a color code, highlighting that graphenes bands (dark grey) are clearly distinguishable from HfO₂'s valence band (mostly Oxygen bands in red) and the conduction band (with more weight on Hfs 3d orbitals).

nanotubes act as anchoring sites for the adhesion to the nanoparticles. The effect is even stronger when both O and C vacancies are considered, and are placed close together. In the atomic structure we observe how one of the C atoms displaces significantly from the graphene layer, approaching the HfO_2 surface. This obviously affects the defect levels from the vacancy (both σ and π). Figure 8.6-(d) shows the strong modification of graphene's bands, and the presence of defect levels formed from the interaction between V_O and V_C states.

It is worth mentioning that we have only considered neutral defect calculations to avoid problems with defining a common reference energy for the different structural models that we studied. However, from the stability diagram discussed in Section 4.4 we know that the most stable defect configuration for the oxygen vacancy in HfO_2 is V_O^{+2} for almost all values of the electronic chemical potential within the gap. The essential difference will be that in this case the defect level will be depopulated, but the physical picture will not be affected. Once an electron from the valence band of HfO_2 is photoexcited to the defect level, it will be easily transferred to the carbon bands, and generate the photocurrent.

8.4 Computational Details

For our calculations we used the PBEsol [CFD11a] exchange-correlation functional form of the generalized gradient approximation from well converged and tested pseudopotential pseudo-dojo vault [Gar+18]. A mesh cutoff of 800 Ry is used to perform real space integrals in SIESTA, and the reciprocal space sampling density is equivalent to $9 \times 9 \times 1$ Monkhorst-Pack grid in the supercell for converging the charge density and relaxation of structure. The structure was relaxed until the forces converge with a tolerance below 0.04 eV/\AA . For Post-Processing reciprocal space sampling density equivalent to $35 \times 35 \times 1$ is used.

8.5 Conclusions

We have built model structures of the heterostructure between HfO_2 and a graphene monolayer to gain a better understanding of the physical properties of hybrid HfO_2/CNT nanocomposites and validate the experimental hypothesis suggested by the Rauwell and collaborators. As modelization of a HfO_2 nanoparticle is too complex, we decided to take a first approach by considering surfaces with different crystallographic orientations. In agreement with literature we

found that the (111) orientation gives the most stable termination. These will give a reasonable description of the facets of large nanoparticles. Over the slab we considered a graphene monolayer, which gives a reasonable description of nanotubes with large diameter. A commensurate supercell can be built with a 2×2 HfO₂ slab and a 3×3 graphene layer. Then, we addressed the effect of candidate vacancy defects on the properties of the heterointerface. In particular we show:

- (i) The lower energy formation of vacancies at the surface as compared to the bulk, which confirms the possibility of a larger concentration of defects in systems with larger surface/bulk ratio, as is the case of HfO₂ nanoparticles. The shift of the defect level within the gap is also in agreement with features reported for the photoluminescence spectra.
- (ii) a larger absorption of graphene to the oxide interface can be linked to the presence of C dangling bonds (in our case vacancies that induce a substantial deformation of the graphene monolayer).
- (iii) The presence of oxygen vacancies in the interface between the nanoparticle and graphene seems to favor charge transfer towards graphene. The effect of these vacancies on the electronic properties of graphene are negligible.

In this *Thesis*, we have developed a set of computational tools to enable studies of the physical properties of defects from DFT simulations. We have categorized these properties in three different groups: (i) **Static**, where we include energetics of neutral and charged point defects, (ii) **Dynamic** which are related to the energy barriers required to activate the movement of the defects in the material, and (iii) **Surface & Interface Properties** where we focused on utilities that facilitate building models to study materials boundaries. Through the different chapters of this report we have described the theoretical methods required to tackle each one of the properties, and the use of their implementations in a set of examples and case studies. It is worth mentioning that each implementation is not a monolithic unit but might include several intermediate steps, and the tools here developed can be combined to have greater flexibility. For example, we can include the corrections taken for charged defects also in the study of migration barriers at an heterostructure between complex transition metal oxides. On the following, I will highlight the main results and conclusions of the work.

- We investigated the need to include *ghost* orbitals in the basis set to correctly describe localized electronic states created at vacancies and their charge distribution. This is a critical aspect of the use of strictly localized atomic orbitals, which is one of the foundations of the SIESTA method. We showed that the computational cost of these *ghost* orbitals is negligible, and although support basis orbitals from neighbour atoms might be capable of describing the defect level in bulk (as long as their cutoff radii are not too short), it is highly advisable to include *ghost* orbitals when dealing with vacancies, as the description of the charge localization is improved. For the computation of migration barriers, we suggest the use of *two* fixed ghost orbitals placed at the initial and final images of the NEB path. Indeed, we show that the *ghost* orbitals seem to be more important to describe the initial and final positions of the vacancy than the Transition State itself.
- We used the Freysoldt, Neugebauer, and Van de Walle (FNV) correction scheme for charged point defects in periodic boundary conditions. In

agreement with previous reports in the literature, we showed that the use of a Gaussian charge model does not work well if the defect charge density is not well localized. This delocalization could be an artifact of the calculation, either because of limitations with the DFT functionals, or because the supercell used is simply too small and the defect states interact with periodic images forming a defect electronic band. Furthermore, we highlighted the strong sensitivity of the corrected defect energetics to the parameters used to define the Gaussian distribution, even in cases where the charge is reasonably localized such as V_O in MgO .

- Based on the FNV method, we developed an alternative approach for taking care of the image-charge correction for charged point defects in periodic boundary conditions. Our method makes use of the DFT charge density, and unlike previous approaches does not rely on parametrized models. We validated our methodology in systems that had been reported to be problematic for the conventional FNV scheme, such as carbon vacancy in diamond, or Ga vacancies in GaAs. Our method shows very good convergence of the formation energy even for relatively small supercells.
- We attribute possible problems in the correction scheme to three main reasons: (i) Not using big enough supercells, which results in very large interactions with periodic images, and thus dispersive defect bands that give rather delocalized charge densities. This problem is easily solved by increasing the simulation box. With our scheme, issues with delocalization of the charge seem to be minimized. (ii) Failures of *DFT* functionals when localizing the charge density around the point defect. These problems require a higher level of theory, but are beyond the scope of the methodology for computing the formation energy of the defect that are discussed here. (iii) Materials where complex *PES* can give strong lattice deformations due to the presence of the defect, bringing problems for the correct potential alignment with respect to the pristine neutral crystal. These lattice instabilities (or phase transitions) are the harder to control from the automatic computational perspective, as they really hide a physical effect that requires attention (although it might also be linked to issues with the DFT functional).
- The Nudged Elastic Band method implemented in *SIESTA* adds a powerful functionality to the code, which is very well suited to treat defect

structures at a low computational footprint. Based on our experience we can compute larger supercells (thus more realistic defect concentrations) at a fraction of the cost of alternative planewave codes, with equivalent accuracy. We tested our NEB implementation in a simple system (V_O in MgO) that allowed us to quantify, for the first time to our knowledge, the effect of the Basis Set Superposition Error (BSSE), and the image charge interaction correction schemes for the migration of ions. Both effects seem to give minor contributions for V_O in MgO, although this could be system-dependent and further investigations might be needed. On the other hand, we confirm a strong sensitivity of the migration barrier with the charge state of the migrating vacancy.

- We combined the tools to generate slabs, with the methodologies for studying point defects to investigate the physical properties of hybrid HfO_2 /CNT nanocomposites and validate the experimental hypothesis suggested by Rauwel and collaborators. In particular, (i) we proved the lower formation energy of vacancies at surfaces as compared to the bulk, which confirms the possibility of a larger concentration of defects in systems with a larger surface/bulk ratio, as is the case of HfO_2 nanoparticles. (ii) the shift in the defect level for vacancies close to the surface agrees with features reported for the photoluminescence spectra. (iii) The presence of both oxygen and carbon vacancies at the HfO_2 /graphene interface increases the binding energy, and agrees with experimental suggestions for defects acting as anchoring sites for nanoparticle's adhesion to carbon nanotubes. Furthermore, we show that oxygen vacancies favor charge transfer towards graphene, facilitating the extraction of photogenerated charges from the nanoparticle.

We have paid special attention to the limits of the approximations that are more commonly used in simulations of point defects, and in particular to the more technical aspects which are specific of the SIESTA methodology, such as the use of strictly localized atomic orbitals. This is particularly critical for the development of *ab initio* high-throughput workflows that require unsupervised calculations for many different defect configurations and systems, as described for example in [Ang+14; Goy+17; MM16].

In addition to the SISL TOOLBOX implementations, and in view of the increased demand for *high-throughput* calculations with defects, all tools have been ex-

tended to *AiiDA Workflows* adapted to the SIESTA package. This scheme allows not only to handle a large number of calculations, but also offers integration with a searchable database, and interoperability with other workflows implemented by the electronic structure community, as well as possible combinations with different DFT codes in a standardized way. I believe the tools developed in my thesis will ease the future screening of defects properties in materials research. The technical documentation of these computational tools will be submitted soon for publication.

Part V

Appendix

A.1 Introduction

Development of new methods, testing algorithms and improving the efficiency of computational tools usually require multiple modifications of code lines. A faster development can be fostered by a direct access to code variables and functions through external scripts that can be embedded into the main code. There is an ongoing trend in many areas of computational science to move away from rigid and monolithic codes and favor a more flexible approach, in which the internal functionality of a program is somehow exposed to the outside world. If this is done in a proper and well-documented way, it can enhance the interoperability of codes with different functionalities, play to the relative strengths of each, and/or implement new functionalities by combining the available basic blocks. Here I review the implementation of this strategy in SIESTA, which is based on handing control to the LUA interpreter at specific relevant points in the program flow (e.g., at the beginning of a geometry step, at the end of an SCF step, etc.). Although the presented library is implemented in SIESTA, however, it is independent of it and could be easily interfaced with any other simulation code.

A.1.1 LUA

LUA is a powerful open-source, fast, lightweight, and embeddable programming language, which started as an in-house project in 1993 by Roberto Ierusalimsky, Luiz Henrique de Figueiredo, and Waldemar Celes.

LUA can run on many systems and many devices where most other scripting languages would not be able to run [Ier06]. Moreover is an easy-to-learn and fast scripting language, It is very lightweight (its memory footprint is less than 300 kB), and provides very simple ways to interface to the data structures and routines of a host program. A LUA script, interpreted by the LUA interpreter embedded in the program, can then control the flow of execution and the data. Different

user-level scripts can implement new functionalities, without recompilation of the host code.

One of particular feature which is interested to us is that, the LUA scripts implement handlers appropriate to the point they want to hook into, and can request access to specific data structures. Hence we could implement algorithms without recompiling our original code. For example, a script intended to implement a better scf mixing algorithm would be executed after every scf step, inspecting the convergence data, and changing mixing parameters or schemes, as appropriate. As another example, convergence checks over mesh-cutoffs and k-point sampling can be performed automatically. The code in the library can be re-used, or taken as starting point for other implementations by users. These user-level scripts can in turn be shared, opening the way to the development of new functionality with faster turnaround than the traditional approach that needs a careful integration into the program's code base LUA [Gar+20a].

A.2 Fortran LUA Hook (FLOOK) Library

A.2.1 Concepts & Implementations

Here we going to review the development of an internal scripting framework based on the LUA language, which enables new functionality without code recompilation.

The fortran-Lua-hook library allows abstraction of input files to be pure LUA files to enable configuration of internal variables through an embedded LUA interpreter. Any valid LUA script can be executed from within any fortran application at points where the application creates LUA channels. Its main usage is the ability to change run-time variables at run-time in order to optimize, or even change, the execution path of the parent program.

Assuming we have a program which has 3 distinct places where interaction might occur figure :

```
1 program main
2 call initialize()
3 call calculate()
4 call finalize()
5 end program
```

At each intermediate point one wishes to communicate with a scripting lan-

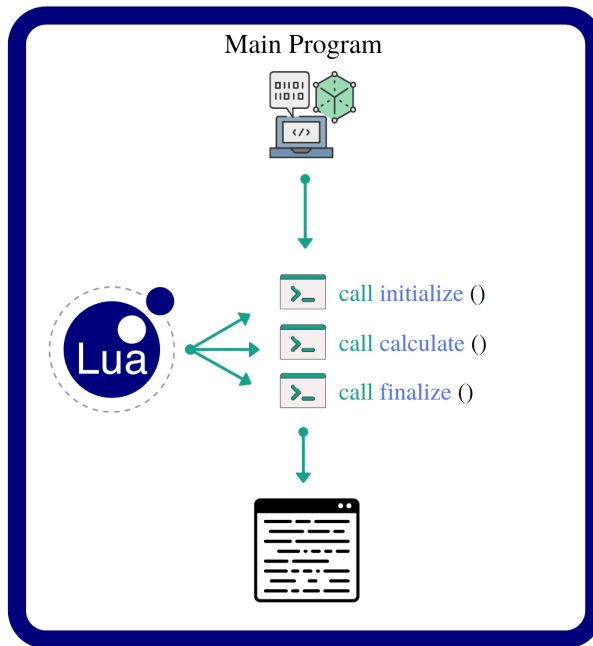


Figure A.1: FLOOK Library Scheme can create main points in the Fortran program to communicate with particular variables.

guage. FLOOK enable to communicate between fortran and LUA. To do so we will use flook lib in out main program ... TODO: Write Details of how it works!!!!...

```

1  ! Our calculating program
2  program main
3    use flook
4    ! Global variables in the scope that
5    ! we will communicate with
6    real :: matrix(3,3), vector(3)
7    real :: control
8    type(luaState) :: lua
9    ! Initialize the @lua environment
10   call lua_init(lua)
11   ! Register a couple of functions to pass information back and
12   ! forth between @lua.
13   call lua_register(lua, 'fortran_get', script_set )
14   call lua_register(lua, 'fortran_set', script_get )
15   ! Call pre-initialize script (this should define
16   ! all functions that are directly called in the program.
17   ! Needless to say you can create a single @lua function
  
```

```

18 ! which will determine the path via a control parameter.
19 call lua_run(lua, 'tst_exp_flook.lua' )
20 call lua_run(lua, code = 'pre_init()' )
21 call initialize()
22 call lua_run(lua, code = 'post_init()' )
23 call lua_run(lua, code = 'pre_calc()' )
24 call calculate()
25 call lua_run(lua, code = 'post_calc()' )
26 call lua_run(lua, code = 'pre_finalize()' )
27 call finalize()
28 call lua_run(lua, code = 'post_finalize()' )
29 ! Close @lua
30 call lua_close(lua)
31 contains
32 function script_set(state) result(nret)
33     use, intrinsic :: iso_c_binding, only: c_ptr, c_int
34     type(c_ptr), value :: state
35     ! Define the in/out
36     integer(c_int) :: nret
37     type(luaState) :: lua
38     type(luaTbl) :: tbl
39     call lua_init(lua,state)
40     ! open global table in variable struct
41     tbl = lua_table(lua,'struct')
42     ! Set the variables to the struct table:
43     ! struct.control = `control`
44     call lua_set(tbl,'control',control)
45     ! struct.matrix = `matrix`
46     call lua_set(tbl,'matrix',matrix)
47     ! struct.vector = `vector`
48     call lua_set(tbl,'vector',vector)
49     call lua_close_tree(tbl)
50     ! this function returns nothing
51     nret = 0
52 end function script_set
53 function script_get(state) result(nret)
54     use, intrinsic :: iso_c_binding, only: c_ptr, c_int
55     ! Define the state
56     type(c_ptr), value :: state
57     ! Define the in/out
58     integer(c_int) :: nret
59     type(luaState) :: lua
60     type(luaTbl) :: tbl
61     call lua_init(lua,state)
62     ! open global table in variable struct
63     tbl = lua_table(lua,'struct')
64     ! Get the variables from the struct table:
65     call lua_get(tbl,'control',control)
66     call lua_get(tbl,'matrix',matrix)
67     call lua_get(tbl,'vector',vector)
68     call lua_close_tree(tbl)
69     ! this function returns nothing

```

```

70     nret = 0
71     end function script_get
72
73     subroutine initialize()
74         control = 0.
75         matrix = 0.5
76         matrix(1,1) = 1.
77         matrix(2,2) = 2.
78         matrix(3,3) = 3.
79         vector = (/1.,2.,3./)
80     end subroutine initialize
81
82     subroutine calculate
83         integer :: i
84         do i = 1 , 3
85             vector(i) = sum(matrix(:,i) * vector) * control
86             matrix(i,:) = vector
87         end do
88     end subroutine calculate
89
90     subroutine finalize
91         matrix(1,1) = vector(1)
92         matrix(2,2) = vector(2)
93         matrix(3,3) = vector(3)
94     end subroutine finalize
95
96 end program main

```

Now with the script of Lua we could communicate with our fortran program:

```

1  --[[
2      LUA function called by fortran
3  --]]
4  print("LUA called from FORTRAN")
5  -- Define the handle for retaining data
6  struct = {}
7
8  function pre_init()
9      -- Communicate data from fortran
10     fortran_get()
11     struct:print("pre_init")
12     struct.control = 2.
13     -- Communicate data to fortran
14     fortran_set()
15 end
16
17 function post_init()
18     fortran_get()
19     struct:print("post_init")

```



```

20     struct.control = 1.
21     fortran_set()
22 end
23
24 function pre_calc()
25     fortran_get()
26     struct:print("pre_calc")
27     struct.control = 2.
28     struct.vector[2] = 0.
29     fortran_set()
30 end
31
32 function post_calc()
33     fortran_get()
34     struct:print("post_calc")
35     fortran_set()
36 end
37
38 function pre_finalize()
39     fortran_get()
40     struct:print("pre_finalize")
41     struct.control = 3.
42     fortran_set()
43 end
44
45 function post_finalize()
46     fortran_get()
47     struct:print("post_finalize")
48
49     fortran_set()
50     print("Fully ran everything in the LUA file")
51 end
52
53 --[[
54     To ease the printing of the data structures
55     we add a few helper functions to print matrices in a stringent
56     way
57 --]]
58 function mat_print(name,mat)
59     print("Printing matrix: "..name)
60     a = ""
61     is_matrix = false
62     for ia,xyz in pairs(mat) do
63         if type(xyz) == "table" then
64             is_matrix = true

```

```

65  a = ""
66  for _,x in pairs(xyz) do a = a .. " " .. x end
67  print(a)
68  else
69  a = a .. " " .. xyz
70  end
71  end
72  if not is_matrix then print(a) end
73 end
74
75 struct.print = function(self,msg)
76   if msg then print(msg) end
77   print("Control: " .. self.control)
78   mat_print("matrix",self.matrix)
79   mat_print("vector",self.vector)
80   print("") -- new line
81 end

```

The integration of LUA functionality in SIESTA has been made possible by the development of an intermediate layer, FLOOK, (for “fortran-Lua-hook”), which provides wrappers for access to Fortran data structures and subroutines.

A.3 Flook SIESTA (FLOS) Library

After retrieving variables or arrays one have to do process or manipulate on those data, so to do so, we developed a library which allows to easily use and developed new schemes and functionality for SIESTA, we called this Library FLOS (FLOOK SIESTA). The mentioned scenario open an important area of usefulness of the approach. The prototyping in LUA, followed eventually by a full implementation, of new ideas and algorithms. We have implemented a number of custom molecular dynamics modes, geometry relaxation algorithms, and advanced optimization schemes For SIESTA Package, in a pure LUA library FLOS [citation] figure A.2.

First and foremost in SIESTA with FLOOK enabled, We put 7 intermediate point to communicate:

- (1) Right after reading initial options (siesta.INITIALIZE)
- (2) Right before SCF step starts, but at each MD step (siesta.INIT_MD)
- (3) At the start of each SCF step (siesta.SCF_LOOP)

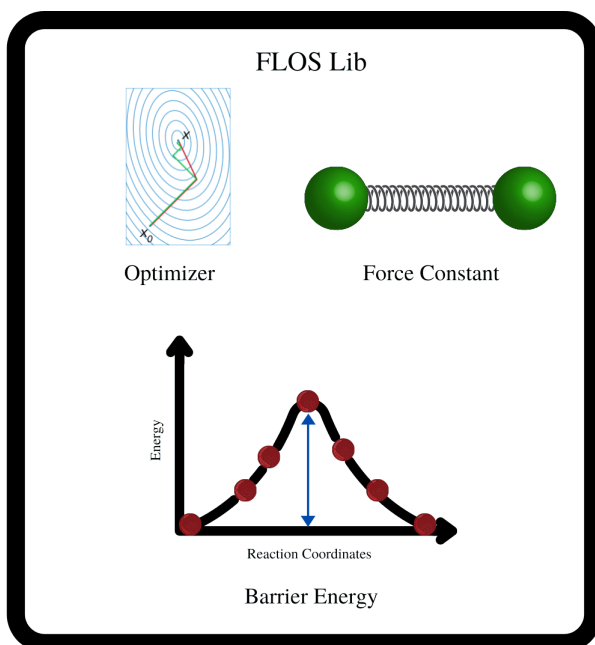


Figure A.2: FLOS Lib contains different schemes & functionality for SIESTA such as a new optimizer, nudged elastic band, grid convergence test algorithm etc.

- (4) After each SCF has finished (siesta.FORCES)
- (5) When moving the atoms, right after the FORCES step (siesta.MOVE)
- (6) When SIESTA is complete (siesta.ANALYSIS)
- (7) When SIESTA is In Analysis Mode, just before it exists (siesta.ANALYSIS_AFTER)

We call above intermediate points state in LUA script which one could communicate with SIESTA via state definition. In each intermediate points states we could send or receive data via special name we call them SIESTA LUA dictionary. All available dictionary are implemented in module called *siesta_dicts* in SIESTA. The Table (A.1) presented all variables which could access via LUA script.

Our Approach on implementation of FLOS library was based on object oriented methodologies. Hence each functionally has it own class which could be access easily or inherited by another class. FLOS library contains (4) Main Classes which has its own particular functionality Figure (A.3):

- MD Class : This class retains information on a single MD step, such a step may be represented by numerous quantities. Such as atomic coordinates, velocities, forces and an energy associated with the current step. Of course one may always add new information.
- NUM Class : This Class is Implementation of ND Arrays in LUA. This module tries to be as similar to the Python numpy package as possible.
- Optima Class : This Class contains of different classes which inherited by it base class that is the basic class used for optimization routines. Here we already implemented CG, FIRE LBFGS Method for Optimizing.
- Special Class : In this Class we developed different flavor of Barrier energy calculator such is NEB, DNEB, VC-NEB, ... and Force Constant calculator.

Each Main Classes have couple of sub-classes which inherinted by Main/Other classes.

Now using those intermediate points along with FLOS we could write different LUA script for particular applications. In Following chapters we show some applications of FLOS mostly the implementation of NEB algorithms which use SIESTA as engine to calculate the NEB forces.

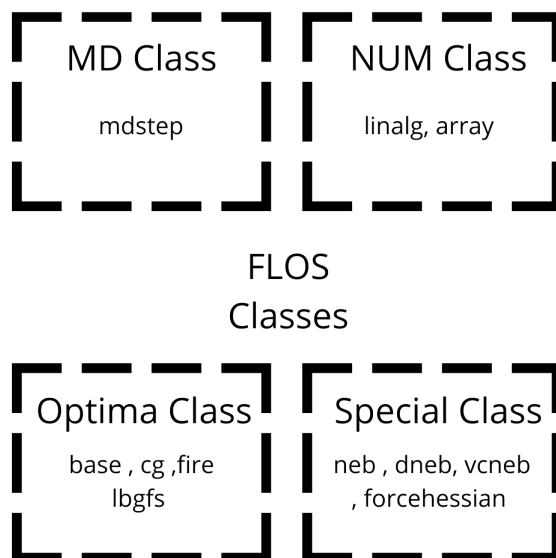


Figure A.3: Flos Library contains four main Class: i) Molecular Dynamic (MD) class, ii) Numerical (Num) Class, iii) Optimizer (Optima) Class and iv) Special Class

SIESTA FDF flags	SIESTA LUA Dictionary (variables)	SIESTA FDF flags	SIESTA LUA Dictionary (variables)
SystemLabel	slabel	DM.HistoryDepth	DM_history_depth
Write.DenChar	dumpcharge	Write.MullikenPop	mullipop
Write.HirshfeldPop	hirshpop	Write.VoronoiPop	voropop
SCF.MinIterations	min_nscf	SCF.MaxIterations	nscf
SCF.MixHamiltonian	mixH	SCF.MixCharge	mix_charge
SCF.NumberPulay	maxsav	SCF.NumberBroyden	broyden_maxit
SCF.MixingWeight	wmix	SCF.NumberKick	nkick
SCF.KickMixingWeight	wmixkick	SCF.Mixer.Weight	scf_mixs(1)%w
SCF.Mixer.Restart	scf_mixs(1)%restart	SCF.Mixer.Iterations	scf_mixs(1)%n_itt
SCF.MonitorForces	monitor_forces_in_scf	electronicTemperature	temp
SCF.Harris.Converge	converge_Eharr	SCF.Harris.Tolerance	tolerance_Eharr
SCF.DM.Converge	converge_DM	SCF.DM.Tolerance	dDtol
SCF.EDM.Converge	converge_EDM	SCF.EDM.Tolerance	tolerance_EDM
SCF.H.Converge	converge_H	SCF.H.Tolerance	dHtol
SCF.FreeE.Converge	converge_FreeE	SCF.FreeE.Tolerance	tolerance_FreeE MD.MaxDispl
dxmax	MD.MaxForceTol	ftol	
MD.MaxStressTol	strtol	MD.FinalTimeStep	ifinal
MD.FC.Displ	dx	MD.FC.First	ia1
MD.FC.Last	ia2	MD.Temperature.Target	tt
MD.Relax.CellOnly	RelaxCellOnly	MD.Relax.Cell	varcel
MD.Steps.First	inicoor	MD.Steps.Last	fincoor
MD.DM.History.Depth	DM_history_depth	Write.HS	saveHS
Write.DM	writeDM	Write.EndOfCycle.DM	write_DM _{at_end_of_cycle}
Write.H	writeH	Write.EndOfCycle.H	write_H_at_end_of_cycle
Write.Forces	writeF	Use.DM	UseSaveDM
Write.Hirshfeld	hirshpop	Write.Voronoi	voropop

Table A.1: Available variables for SIESTA and it corresponding dictionary name.

Bibliography

- [Ala+21] Md Nur K Alam, Sergiu Clima, BJ O'sullivan, Ben Kaczer, Geoffrey Pourtois, Marc Heyns, and Jan Van Houdt. **First principles investigation of charge transition levels in monoclinic, orthorhombic, tetragonal, and cubic crystallographic phases of HfO₂**. *Journal of Applied Physics* 129:8 (2021), 084102 (see pages 83, 132).
- [Alf96] Zh I. Alferov. **The history and future of semiconductor heterostructures from the point of view of a Russian scientist**. *Physica Scripta T* 68:January (1996), 32–45. ISSN: 02811847. DOI: [10.1088/0031-8949/1996/t68/005](https://doi.org/10.1088/0031-8949/1996/t68/005) (see page 128).
- [And+21] Oxana Andriuc, Martin Siron, Joseph H Montoya, Matthew Horton, and Kristin A Persson. **Automated adsorption workflow for semiconductor surfaces and the application to zinc telluride**. *Journal of Chemical Information and Modeling* 61:8 (2021), 3908–3916 (see page 10).
- [Ang+02] Eduardo Anglada, José M. Soler, Javier Junquera, and Emilio Artacho. **Systematic generation of finite-range atomic basis sets for linear-scaling calculations**. *Phys. Rev. B* 66 (20 Nov. 2002), 205101. DOI: [10.1103/PhysRevB.66.205101](https://doi.org/10.1103/PhysRevB.66.205101). URL: <https://link.aps.org/doi/10.1103/PhysRevB.66.205101> (see pages 8, 9).
- [Ang+14] Thomas Angsten, Tam Mayeshiba, Henry Wu, and Dane Morgan. **Elemental vacancy diffusion database from high-throughput first-principles calculations for fcc and hcp structures**. *New Journal of Physics* 16:1 (2014), 015018 (see page 145).
- [Bag+21] Tommaso Bagni, Gianmarco Bovone, A Rack, Diego Mauro, Christian Barth, Davide Matera, Florin Buta, and Carmine Senatore. **Machine learning applied to X-ray tomography as a new tool to analyze the voids in RRP Nb₃Sn wires**. *Scientific Reports* 11:1 (2021), 1–14 (see page 31).
- [Ben99] Lennart Bengtsson. **Dipole correction for surface supercell calculations**. *Physical Review B* 59:19 (1999), 12301 (see page 127).
- [Blo28] Felix Bloch. **Quantum mechanics of electrons in crystal lattices**. *Z. Phys* 52 (1928), 555–600 (see page 42).
- [Blo29] Felix Bloch. **Über die quantenmechanik der elektronen in kristallgittern**. *Zeitschrift für physik* 52:7 (1929), 555–600 (see pages 20, 42).

- [Bon] Probir K Bondyopadhyay. **Semiconductor Amplifier Patent** () (see page 127).
- [Bou+20] Laure Bourgeois, Yong Zhang, Zezhong Zhang, Yiqiang Chen, and Nikhil V Medhekar. **Transforming solid-state precipitates via excess vacancies**. *Nature communications* 11:1 (2020), 1–10 (see page 31).
- [BS17] Subodh Barthwal and Nakshatra B Singh. **ZnO-CNT nanocomposite: a device as electrochemical sensor**. *Materials today: proceedings* 4:4 (2017), 5552–5560 (see page 6).
- [Byr+08] Kullaiah Byrappa, Alaloor S Dayananda, C Ponnappa Sajan, B Basavalingu, MB Shayan, Kohei Soga, and Masahiro Yoshimura. **Hydrothermal preparation of ZnO: CNT and TiO₂: CNT composites and their photocatalytic applications**. *Journal of Materials Science* 43:7 (2008), 2348–2355 (see page 6).
- [CFD11a] Lucian A. Constantin, E. Fabiano, and F. Della Sala. **Improving atomization energies of molecules and solids with a spin-dependent gradient correction from one-electron density analysis**. *Phys. Rev. B* 84 (23 Dec. 2011), 233103. DOI: [10.1103/PhysRevB.84.233103](https://doi.org/10.1103/PhysRevB.84.233103). URL: <https://link.aps.org/doi/10.1103/PhysRevB.84.233103> (see pages 89, 116, 140).
- [CFD11b] Lucian A. Constantin, E. Fabiano, and F. Della Sala. **Improving atomization energies of molecules and solids with a spin-dependent gradient correction from one-electron density analysis**. *Phys. Rev. B* 84 (23 Dec. 2011), 233103. DOI: [10.1103/PhysRevB.84.233103](https://doi.org/10.1103/PhysRevB.84.233103). URL: <https://link.aps.org/doi/10.1103/PhysRevB.84.233103> (see page 89).
- [Cha+21] Mauricio Chagas Da Silva, Michael Lorke, Bálint Aradi, Meisam Farzalipour Tabriz, Thomas Frauenheim, Angel Rubio, Dario Rocca, and Peter Deák. **Self-Consistent Potential Correction for Charged Periodic Systems**. *Physical Review Letters* 126:7 (Feb. 2021). ISSN: 10797114. DOI: [10.1103/PhysRevLett.126.076401](https://doi.org/10.1103/PhysRevLett.126.076401). arXiv: [2005.03378](https://arxiv.org/abs/2005.03378) (see page 49).
- [Cho+20] Myung-Soo Choi, Taehyun Park, Woo-Jae Kim, and Jaehyun Hur. **High-performance ultraviolet photodetector based on a zinc oxide nanoparticle@ single-walled carbon nanotube heterojunction hybrid film**. *Nanomaterials* 10:2 (2020), 395 (see page 6).
- [Dab+08] Ismaila Dabo, Boris Kozinsky, Nicholas E. Singh-Miller, and Nicola Marzari. **Electrostatics in periodic boundary conditions and real-space corrections**. *Physical Review B - Condensed Matter and Materials Physics* 77 (11 Mar. 2008). ISSN: 10980121. DOI: [10.1103/PhysRevB.77.115139](https://doi.org/10.1103/PhysRevB.77.115139) (see pages 50, 56).

- [Das+18] Pratteek Das, Qiang Fu, Xinhe Bao, and Zhong-Shuai Wu. **Recent advances in the preparation, characterization, and applications of two-dimensional heterostructures for energy storage and conversion.** *Journal of Materials Chemistry A* 6:44 (2018), 21747–21784 (see page 128).
- [Dir30] Paul AM Dirac. **Note on exchange phenomena in the Thomas atom.** In: *Mathematical proceedings of the Cambridge philosophical society*. Vol. 26. 3. Cambridge University Press. 1930, 376–385 (see pages 20, 22).
- [Dur+18] T. R. Durrant, S. T. Murphy, M. B. Watkins, and A. L. Shluger. **Relation between image charge and potential alignment corrections for charged defects in periodic boundary conditions.** *Journal of Chemical Physics* 149 (2 July 2018). ISSN: 00219606. DOI: [10.1063/1.5029818](https://doi.org/10.1063/1.5029818) (see pages 45, 50, 57, 58, 71, 77).
- [El-+18] Al Moatasem El-Sayed, Matthew B. Watkins, Tibor Grassner, and Alexander L. Shluger. **Effect of electric field on migration of defects in oxides: Vacancies and interstitials in bulk MgO.** *Physical Review B* 98:6 (2018), 1–12. ISSN: 24699969. DOI: [10.1103/PhysRevB.98.064102](https://doi.org/10.1103/PhysRevB.98.064102) (see pages 108, 111, 112).
- [FGC05] Yuwei Fan, Brett R Goldsmith, and Philip G Collins. **Identifying and counting point defects in carbon nanotubes.** *Nature materials* 4:12 (2005), 906–911 (see page 31).
- [FNV11] Christoph Freysoldt, Jörg Neugebauer, and Chris G Van de Walle. **Electrostatic interactions between charged defects in supercells.** *physica status solidi (b)* 248:5 (2011), 1067–1076 (see pages 52, 54).
- [FNW09] Christoph Freysoldt, Jörg Neugebauer, and Chris G. Van De Walle. **Fully Ab initio finite-size corrections for charged-defect supercell calculations.** *Physical Review Letters* 102 (1 Jan. 2009). ISSN: 00319007. DOI: [10.1103/PhysRevLett.102.016402](https://doi.org/10.1103/PhysRevLett.102.016402) (see pages 50, 51, 53, 74, 107).
- [Fre65] Smith Freeman Jr. **Scattering from planar defects in metals.** *Journal of Physics and Chemistry of Solids* 26:3 (1965), 473–482 (see page 31).
- [Gar+09a] Sandra García-Gil, Alberto García, Nicolás Lorente, and Pablo Ordejón. **Optimal strictly localized basis sets for noble metal surfaces.** *Physical Review B - Condensed Matter and Materials Physics* 79:7 (Feb. 2009). ISSN: 10980121. DOI: [10.1103/PhysRevB.79.075441](https://doi.org/10.1103/PhysRevB.79.075441) (see page 129).
- [Gar+09b] Sandra García-Gil, Alberto García, Nicolás Lorente, and Pablo Ordejón. **Optimal strictly localized basis sets for noble metal surfaces.** *Phys. Rev. B* 79 (7 Feb. 2009), 075441. DOI: [10.1103/PhysRevB.79.075441](https://doi.org/10.1103/PhysRevB.79.075441). URL: <https://link.aps.org/doi/10.1103/PhysRevB.79.075441> (see page 65).

- [Gar+18] Alberto García, Matthieu J Verstraete, Yann Pouillon, and Javier Junquera. **The psml format and library for norm-conserving pseudopotential data curation and interoperability 2729**. *Computer Physics Communications* 227 (2018), 51–71. DOI: [10.17632/3pgbsjy4vf.1](https://doi.org/10.17632/3pgbsjy4vf.1) (see pages 90, 116, 140).
- [Gar+20a] Alberto Garcia, Nick Papior, Arsalan Akhtar, Emilio Artacho, Volker Blum, Emanuele Bosoni, Pedro Brandimarte, Mads Brandbyge, Jorge I Cerdá, Fabiano Corsetti, et al. **Siesta: Recent developments and applications**. *The Journal of chemical physics* 152:20 (2020), 204108 (see page 150).
- [Gar+20b] Alberto García, Nick Papior, Emilio Artacho, Volker Blum, Emanuele Bosoni, Pedro Brandimarte, Mads Brandbyge, J. I. Cerdá, Fabiano Corsetti, Ramón Cuadrado, Vladimir Dikan, Jaime Ferrer, Julian Gale, Pablo García-Fernández, V. M. García-Suárez, Sandra García, Georg Huhs, Sergio Illera, Richard Korytár, Peter Koval, Irina Lebedeva, Lin Lin, Pablo López-Tarifa, Sara G. Mayo, Stephan Mohr, Pablo Ordejón, Andrei Postnikov, Yann Pouillon, Miguel Pruneda, Roberto Robles, Daniel Sánchez-Portal, Jose M. Soler, Rafi Ullah, Victor Wen-zhe Yu, and Javier Junquera. **Siesta: Recent developments and applications**. *The Journal of Chemical Physics* 152:20 (2020), 204108. DOI: <https://doi.org/10.1063/5.0005077>. URL: <https://doi.org/10.1063/5.0005077> (see page 116).
- [Goy+17] Anuj Goyal, Prashun Gorai, Haowei Peng, Stephan Lany, and Vladan Stevanović. **A computational framework for automation of point defect calculations**. *Computational Materials Science* 130 (2017), 1–9 (see page 145).
- [Han+19] Tae-Hee Han, Shaun Tan, Jingjing Xue, Lei Meng, Jin-Wook Lee, and Yang Yang. **Interface and defect engineering for metal halide perovskite optoelectronic devices**. *Advanced Materials* 31:47 (2019), 1803515 (see page 31).
- [Har28] D. R. Hartree. **The Wave Mechanics of an Atom with a Non-Coulomb Central Field. Part II. Some Results and Discussion**. *Mathematical Proceedings of the Cambridge Philosophical Society* 24:1 (1928), 111–132. DOI: [10.1017/S0305004100011920](https://doi.org/10.1017/S0305004100011920) (see page 18).
- [HH35] Douglas Rayner Hartree and William Hartree. **Self-consistent field, with exchange, for beryllium**. *Proceedings of the Royal Society of London. Series A-Mathematical and Physical Sciences* 150:869 (1935), 9–33 (see page 18).

- [HJ00] Graeme Henkelman and Hannes Jónsson. **Improved tangent estimate in the nudged elastic band method for finding minimum energy paths and saddle points**. *Journal of Chemical Physics* 113:22 (Dec. 2000), 9978–9985. ISSN: 00219606. DOI: [10.1063/1.1323224](https://doi.org/10.1063/1.1323224) (see page 95).
- [HK64] Pierre Hohenberg and Walter Kohn. **Inhomogeneous electron gas**. *Physical review* 136:3B (1964), B864 (see page 18).
- [HL77] Thomas A Halgren and William N Lipschultz. **THE SYNCHRONOUS-TRANSIT METHOD FOR DETERMINING REACTION PATHWAYS AND LOCATING MOLECULAR TRANSITION STATES**. Tech. rep. 2. 1977 (see page 101).
- [Hua+10] Cheng Huang, Qing Liao, Yueming Zhou, and Peixiang Lu. **Role of Coulomb focusing on the electron transverse momentum of above-threshold ionization**. *Optics Express* 18:13 (2010), 14293–14300 (see page 53).
- [Hub+20] Sebastiaan P Huber, Spyros Zoupanos, Martin Uhrin, Leopold Talirz, Leonid Kahle, Rico Häuselmann, Dominik Gresch, Tiziano Müller, Aliaksandr V Yakutovich, Casper W Andersen, et al. **AiiDA 1.0, a scalable computational infrastructure for automated reproducible workflows and data provenance**. *Scientific data* 7:1 (2020), 1–18 (see page 10).
- [Hub+21] Sebastiaan P Huber, Emanuele Bosoni, Marnik Bercx, Jens Bröder, Augustin Degomme, Vladimir Dikan, Kristjan Eimre, Espen Flage-Larsen, Alberto Garcia, Luigi Genovese, et al. **Common workflows for computing material properties using different quantum engines**. *npj Computational Materials* 7:1 (2021), 1–12 (see page 10).
- [Ier06] Roberto Ierusalimsky. **Programming in lua**. Roberto Ierusalimsky, 2006 (see page 149).
- [IZC79] J Ihm, Alex Zunger, and Marvin L Cohen. **Momentum-space formalism for the total energy of solids**. *Journal of Physics C: Solid State Physics* 12:21 (1979), 4409 (see page 46).
- [Joh+02] Gisli Holmar Johannesson, Thomas Bligaard, Andrei V Ruban, Hans Lomholt Skriver, Karsten Wedel Jacobsen, and Jens Kehlet Nørskov. **Combined electronic structure and evolutionary search approach to materials design**. *Physical Review Letters* 88:25 (2002), 255506 (see page 10).
- [Jor+94] JD Jorgensen, Paolo G Radaelli, H Shaked, JL Wagner, BA Hunter, JF Mitchell, RL Hitterman, and DG Hinks. **Roles of oxygen defects in copper oxide superconductors**. *Journal of superconductivity* 7:1 (1994), 145–149 (see page 4).

- [Jun+01] Javier Junquera, Óscar Paz, Daniel Sánchez-Portal, and Emilio Artacho. **Numerical atomic orbitals for linear-scaling calculations**. *Phys. Rev. B* 64 (23 Nov. 2001), 235111. DOI: [10.1103/PhysRevB.64.235111](https://doi.org/10.1103/PhysRevB.64.235111). URL: <https://link.aps.org/doi/10.1103/PhysRevB.64.235111> (see page 8).
- [Kah16] Antoine Kahn. **Fermi level, work function and vacuum level**. *Materials Horizons* 3:1 (2016), 7–10 (see page 46).
- [KDT18] Valentin V. Karasiev, James W. Dufty, and S. B. Trickey. **Nonempirical Semilocal Free-Energy Density Functional for Matter under Extreme Conditions**. *Phys. Rev. Lett.* 120 (7 Feb. 2018), 076401. DOI: [10.1103/PhysRevLett.120.076401](https://doi.org/10.1103/PhysRevLett.120.076401). URL: <https://link.aps.org/doi/10.1103/PhysRevLett.120.076401> (see page 22).
- [Ken+17] J Kennedy, F Fang, J Futter, J Leveneur, PP Murmu, GN Panin, TW Kang, and E Manikandan. **Synthesis and enhanced field emission of zinc oxide incorporated carbon nanotubes**. *Diamond and Related Materials* 71 (2017), 79–84 (see page 6).
- [KJ13] J Kim and S Jandhyala. **Atomic layer deposition of dielectrics for carbon-based electronics**. *Thin Solid Films* 546 (2013), 85–93 (see page 131).
- [KKH70] Lawrence A. Kappers, Roger L. Kroes, and Eugene B. Hensley. **F^+ and F' Centers in Magnesium Oxide**. *Phys. Rev. B* 1 (10 May 1970), 4151–4157. DOI: [10.1103/PhysRevB.1.4151](https://doi.org/10.1103/PhysRevB.1.4151). URL: <https://link.aps.org/doi/10.1103/PhysRevB.1.4151> (see page 71).
- [KO14] Yu Kumagai and Fumiyasu Oba. **Electrostatics-based finite-size corrections for first-principles point defect calculations**. *Physical Review B - Condensed Matter and Materials Physics* 89 (19 May 2014). ISSN: 1550235X. DOI: [10.1103/PhysRevB.89.195205](https://doi.org/10.1103/PhysRevB.89.195205) (see pages 50, 55, 56).
- [KP13] Hannu Pekka Komsa and Alfredo Pasquarello. **Finite-size supercell correction for charged defects at surfaces and interfaces**. *Physical Review Letters* 110:9 (Feb. 2013). ISSN: 00319007. DOI: [10.1103/PhysRevLett.110.095505](https://doi.org/10.1103/PhysRevLett.110.095505) (see page 55).
- [Kre81] Henry Kressel. “The effect of crystal defects on optoelectronic devices.” In: *Semiconductors and Semimetals*. Vol. 16. Elsevier, 1981, 1–52 (see pages 31, 33).
- [KRP12] Hannu Pekka Komsa, Tapio T. Rantala, and Alfredo Pasquarello. **Finite-size supercell correction schemes for charged defect calculations**. *Physical Review B - Condensed Matter and Materials Physics* 86:4 (July 2012). ISSN: 10980121. DOI: [10.1103/PhysRevB.86.045112](https://doi.org/10.1103/PhysRevB.86.045112) (see pages 75–77, 83).

- [KUO11] Katsumasa Kamiya, Naoto Umezawa, and Susumu Okada. **Energetics and electronic structure of graphene adsorbed on HfO 2(111): Density functional theory calculations**. *Physical Review B - Condensed Matter and Materials Physics* 83:15 (Apr. 2011). ISSN: 10980121. DOI: [10.1103/PhysRevB.83.153413](https://doi.org/10.1103/PhysRevB.83.153413) (see pages 136, 138).
- [KV56] F. A. Kröger and H. J. Vink. **Relations between the Concentrations of Imperfections in Crystalline Solids**. *Solid State Physics - Advances in Research and Applications* 3:C (1956), 307–435. ISSN: 00811947. DOI: [10.1016/S0081-1947\(08\)60135-6](https://doi.org/10.1016/S0081-1947(08)60135-6) (see page 37).
- [Leh19] Susi Lehtola. **Curing basis set overcompleteness with pivoted Cholesky decompositions**. *The Journal of Chemical Physics* 151:24 (2019), 241102. DOI: [10.1063/1.5139948](https://doi.org/10.1063/1.5139948). eprint: <https://doi.org/10.1063/1.5139948>. URL: <https://doi.org/10.1063/1.5139948> (see page 111).
- [LG85] M Leslie and N J J Gillan. **C: Solid State Phys. 18 973**. *J. Phys. C: Solid State Phys* 18 (1985), 973–982 (see page 50).
- [Li+15] Shuang Li, Yifeng Wu, Yi Tu, Yonghui Wang, Tong Jiang, Wei Liu, and Yonghao Zhao. **Defects in silicene: Vacancy clusters, extended line defects and di-adatoms**. *Scientific reports* 5:1 (2015), 1–7 (see page 31).
- [Li+19] Bo Li, Lin Fu, Shuang Li, Hui Li, Lu Pan, Lian Wang, Bohong Chang, and Longwei Yin. **Pathways toward high-performance inorganic perovskite solar cells: challenges and strategies**. *Journal of Materials Chemistry A* 7:36 (2019), 20494–20518 (see page 31).
- [Li+21] Wei Li, Mathias Uller Rothmann, Ye Zhu, Weijian Chen, Chenquan Yang, Yongbo Yuan, Yen Yee Choo, Xiaoming Wen, Yi-Bing Cheng, Udo Bach, et al. **The critical role of composition-dependent intragrain planar defects in the performance of MA1-xFAxPbI3 perovskite solar cells**. *Nature Energy* 6:6 (2021), 624–632 (see page 31).
- [Lia+10a] Lei Liao, Jingwei Bai, Rui Cheng, Yung-Chen Lin, Shan Jiang, Yu Huang, and Xiangfeng Duan. **Top-gated graphene nanoribbon transistors with ultrathin high-k dielectrics**. *Nano letters* 10:5 (2010), 1917–1921 (see page 131).
- [Lia+10b] Lei Liao, Jingwei Bai, Yongquan Qu, Yung-chen Lin, Yujing Li, Yu Huang, and Xiangfeng Duan. **High- κ oxide nanoribbons as gate dielectrics for high mobility top-gated graphene transistors**. *Proceedings of the national academy of sciences* 107:15 (2010), 6711–6715 (see page 131).

- [LZ08] Stephan Lany and Alex Zunger. **Assessment of correction methods for the band-gap problem and for finite-size effects in supercell defect calculations: Case studies for ZnO and GaAs**. *Physical Review B - Condensed Matter and Materials Physics* 78 (23 Dec. 2008). ISSN: 10980121. DOI: [10.1103/PhysRevB.78.235104](https://doi.org/10.1103/PhysRevB.78.235104) (see pages 50, 51).
- [LZ09] Stephan Lany and Alex Zunger. **Accurate prediction of defect properties in density functional supercell calculations**. *Modelling and Simulation in Materials Science and Engineering* 17 (8 2009). ISSN: 09650393. DOI: [10.1088/0965-0393/17/8/084002](https://doi.org/10.1088/0965-0393/17/8/084002) (see pages 51, 52).
- [Ma+04] Yuchen Ma, P O Lehtinen, A S Foster, and R M Nieminen. **Magnetic properties of vacancies in graphene and single-walled carbon nanotubes**. *New Journal of Physics* 6 (June 2004), 68–68. DOI: [10.1088/1367-2630/6/1/068](https://doi.org/10.1088/1367-2630/6/1/068). URL: <https://doi.org/10.1088/1367-2630/6/1/068> (see page 138).
- [Ma+13] Jie Ma, Darius Kuciauskas, David Albin, Raghu Bhattacharya, Matthew Reese, Teresa Barnes, Jian V Li, Timothy Gessert, and Su-Huai Wei. **Dependence of the minority-carrier lifetime on the stoichiometry of CdTe using time-resolved photoluminescence and first-principles calculations**. *Physical review letters* 111:6 (2013), 067402 (see page 5).
- [Mar+13] Dominik Martin, Ekaterina Yurchuk, Stefan Müller, Johannes Müller, Jan Paul, Jonas Sundquist, Stefan Slesazeck, Till Schloesser, Ralf van Bentum, Martin Trentzsch, et al. **Downscaling ferroelectric field effect transistors by using ferroelectric Si-doped HfO₂**. *Solid-state electronics* 88 (2013), 65–68 (see page 12).
- [Mat+17] Kiran Mathew, Joseph H Montoya, Alireza Faghaninia, Shyam Dwarakanath, Muratahan Aykol, Hanmei Tang, Iek-heng Chu, Tess Smidt, Brandon Bocklund, Matthew Horton, et al. **Atomate: A high-level interface to generate, execute, and analyze computational materials science workflows**. *Computational Materials Science* 139 (2017), 140–152 (see page 10).
- [MD11] J. Mulroue and D. M. Duffy. **An ab initio study of the effect of charge localization on oxygen defect formation and migration energies in magnesium oxide**. *Proceedings of the Royal Society A: Mathematical, Physical and Engineering Sciences* 467 (2131 July 2011), 2054–2065. ISSN: 13645021. DOI: [10.1098/rspa.2010.0517](https://doi.org/10.1098/rspa.2010.0517) (see pages 66, 109, 111, 112).
- [Mer+08] Inanc Meric, Melinda Y Han, Andrea F Young, Barbaros Ozyilmaz, Philip Kim, and Kenneth L Shepard. **Current saturation in zero-bandgap, top-gated graphene field-effect transistors**. *Nature nanotechnology* 3:11 (2008), 654–659 (see page 131).

- [MH13] Samuel T. Murphy and Nicholas D.M. Hine. **Anisotropic charge screening and supercell size convergence of defect formation energies.** *Physical Review B - Condensed Matter and Materials Physics* 87 (9 Mar. 2013). ISSN: 10980121. DOI: [10.1103/PhysRevB.87.094111](https://doi.org/10.1103/PhysRevB.87.094111) (see page 50).
- [MM16] Tam T Mayeshiba and Dane D Morgan. **Factors controlling oxygen migration barriers in perovskites.** *Solid State Ionics* 296 (2016), 71–77 (see page 145).
- [MP94] G Makov and M C Payne. **Periodic boundary conditions in ab initio calculations.** *PHYSICAL REVIEW* 8 (1994), 15–1995 (see pages 50, 66).
- [Mül+12] Johannes Müller, Tim S. Böske, Uwe Schröder, Stefan Mueller, Dennis Bräuhäus, Ulrich Böttger, Lothar Frey, and Thomas Mikolajick. **Ferroelectricity in simple binary ZrO₂ and HfO₂.** *Nano Letters* 12:8 (Aug. 2012), 4318–4323. ISSN: 15306984. DOI: [10.1021/nl302049k](https://doi.org/10.1021/nl302049k) (see page 12).
- [MV01a] B. Meyer and David Vanderbilt. **Ab initio study of BaTiO₃ and PbTiO₃ surfaces in external electric fields.** *Physical Review B - Condensed Matter and Materials Physics* 63:20 (May 2001). ISSN: 1550235X. DOI: [10.1103/PhysRevB.63.205426](https://doi.org/10.1103/PhysRevB.63.205426). arXiv: 0009288 [cond-mat] (see page 124).
- [MV01b] B Meyer and David Vanderbilt. **Ab initio study of BaTiO₃ and PbTiO₃ surfaces in external electric fields.** *Physical Review B* 63:20 (2001), 205426 (see pages 125, 126).
- [NS93] Jörg Neugebauer and Matthias Scheffler. **Theory of adsorption and desorption in high electric fields.** *Surface science* 287 (1993), 572–576 (see page 127).
- [NZ94] John E Northrup and SB Zhang. **Energetics of the As vacancy in GaAs: The stability of the 3+ charge state.** *Physical Review B* 50:7 (1994), 4962 (see page 81).
- [PBE96] John P. Perdew, Kieron Burke, and Matthias Ernzerhof. **Generalized Gradient Approximation Made Simple.** *Phys. Rev. Lett.* 77 (18 Oct. 1996), 3865–3868. DOI: [10.1103/PhysRevLett.77.3865](https://doi.org/10.1103/PhysRevLett.77.3865). URL: <https://link.aps.org/doi/10.1103/PhysRevLett.77.3865> (see page 22).
- [PFL00] L Polenta, ZQ Fang, and David C Look. **On the main irradiation-induced defect in GaN.** *Applied Physics Letters* 76:15 (2000), 2086–2088 (see page 33).
- [Piz+16] Giovanni Pizzi, Andrea Cepellotti, Riccardo Sabatini, Nicola Marzari, and Boris Kozinsky. **AiiDA: automated interactive infrastructure and database for computational science.** *Computational Materials Science* 111 (2016), 218–230 (see page 10).

- [Qi+20] Wenjing Qi, Xin Zhou, Jiale Li, Jian Cheng, Yuelong Li, Min Jae Ko, Ying Zhao, and Xiaodan Zhang. **Inorganic material passivation of defects toward efficient perovskite solar cells**. *Science Bulletin* 65:23 (2020), 2022–2032 (see page 31).
- [Qia+13] Guang Rui Qian, Xiao Dong, Xiang Feng Zhou, Yongjun Tian, Artem R. Oganov, and Hui Tian Wang. **Variable cell nudged elastic band method for studying solid-solid structural phase transitions**. *Computer Physics Communications* 184:9 (Sept. 2013), 2111–2118. ISSN: 00104655. DOI: [10.1016/j.cpc.2013.04.004](https://doi.org/10.1016/j.cpc.2013.04.004) (see page 99).
- [RAC84] B Roebuck, EA Almond, and AM Cottenden. **The influence of composition, phase transformation and varying the relative FCC and HCP phase contents on the properties of dilute Coe5f8 We5f8 C alloys**. *Materials Science and Engineering* 66:2 (1984), 179–194 (see page 31).
- [Raj78] A K Rajagopal. **Inhomogeneous relativistic electron gas**. *Journal of Physics C: Solid State Physics* 11:24 (Dec. 1978), L943–L948. DOI: [10.1088/0022-3719/11/24/002](https://doi.org/10.1088/0022-3719/11/24/002). URL: <https://doi.org/10.1088/0022-3719/11/24/002> (see page 22).
- [Rau+] P Rauwel, Augustinas Galeckas, F Ducroquet, and E Rauwel. **Selective photocurrent generation in HfO₂ and carbon nanotube hybrid nanocomposites under Ultra-Violet and visible photoexcitations**. *Selective photocurrent generation in HfO₂-CNT hybrid nanocomposites under UV and visible photoexcitations* (). DOI: [10.1016/j.matlet.2019.03.030](https://doi.org/10.1016/j.matlet.2019.03.030). URL: <https://hal.archives-ouvertes.fr/hal-02068477> (see page 131).
- [Rau+12] P. Rauwel, E. Rauwel, C. Persson, M. F. Sunding, and A. Galeckas. **One step synthesis of pure cubic and monoclinic HfO₂ nanoparticles: Correlating the structure to the electronic properties of the two polymorphs**. *Journal of Applied Physics* 112:10 (Nov. 2012). ISSN: 00218979. DOI: [10.1063/1.4766272](https://doi.org/10.1063/1.4766272) (see pages 131, 132).
- [Rau+16] Protima Rauwel, Augustinas Galeckas, Martin Salumaa, Frédérique Ducroquet, and Erwan Rauwel. **Photocurrent generation in carbon nanotube/cubic-phase HfO₂ nanoparticle hybrid nanocomposites**. *Beilstein Journal of Nanotechnology* 7:1 (2016), 1075–1085 (see page 135).
- [Rau+17a] P. Rauwel, A. Galeckas, M. Salumaa, A. Aasna, F. Ducroquet, and E. Rauwel. **Investigations on new carbon-based nanohybrids combining carbon nanotubes, HfO₂ and ZnO nanoparticles**. In: *IOP Conference Series: Materials Science and Engineering*. Vol. 175. 1. Institute of Physics Publishing, Feb. 2017. DOI: [10.1088/1757-899X/175/1/012064](https://doi.org/10.1088/1757-899X/175/1/012064) (see page 131).

- [Rau+17b] P Rauwel, A Galeckas, M Salumaa, A Aasna, F Ducroquet, and E Rauwel. **Investigations on new carbon-based nanohybrids combining carbon nanotubes, HfO₂ and ZnO nanoparticles**. In: *IOP Conference Series: Materials Science and Engineering*. Vol. 175. 1. IOP Publishing. 2017, 012064 (see page 131).
- [Rau+19a] P. Rauwel, Augustinas Galeckas, F. Ducroquet, and E. Rauwel. **Selective photocurrent generation in HfO₂ and carbon nanotube hybrid nanocomposites under Ultra-Violet and visible photoexcitations**. *Materials Letters* 246 (July 2019), 45–48. ISSN: 18734979. DOI: [10.1016/j.matlet.2019.03.030](https://doi.org/10.1016/j.matlet.2019.03.030) (see page 131).
- [Rau+19b] P. Rauwel, Augustinas Galeckas, F. Ducroquet, and E. Rauwel. **Selective photocurrent generation in HfO₂ and carbon nanotube hybrid nanocomposites under Ultra-Violet and visible photoexcitations**. *Materials Letters* 246 (2019), 45–48. ISSN: 0167-577X. DOI: <https://doi.org/10.1016/j.matlet.2019.03.030>. URL: <https://www.sciencedirect.com/science/article/pii/S0167577X19304021> (see page 133).
- [RGR15] P. Rauwel, A. Galeckas, and E. Rauwel. **One Step Synthesis of Pure Cubic and Monoclinic HfO₂ Nanoparticles: Effects of Temperature and Ambient on the Photoluminescent Properties**. *ECS Transactions* 64:44 (Apr. 2015), 19–28. ISSN: 1938-6737. DOI: [10.1149/06444.0019ecst](https://doi.org/10.1149/06444.0019ecst) (see page 131).
- [Rho+19] Daniel Rhodes, Sang Hoon Chae, Rebeca Ribeiro-Palau, and James Hone. **Disorder in van der Waals heterostructures of 2D materials**. *Nature materials* 18:6 (2019), 541–549 (see page 31).
- [Ric13] Norina Richter. **Charged point defects in oxides—a case study of MgO bulk and surface F centers**. PhD thesis. Technische Universität Berlin, 2013 (see page 71).
- [Rob+10] Joshua A Robinson, Michael LaBella III, Kathleen A Trumbull, Xiaojun Weng, Randall Cavelero, Tad Daniels, Zachary Hughes, Mathew Hollander, Mark Fanton, and David Snyder. **Epitaxial graphene materials integration: effects of dielectric overlayers on structural and electronic properties**. *Acs Nano* 4:5 (2010), 2667–2672 (see page 131).
- [Rot+22] D Rothhardt, A Kimouche, T Klamroth, and R Hoffmann-Vogel. **Local work function on Graphene Nanoribbons and on the Au (111) herringbone reconstruction**. *arXiv preprint arXiv:2203.06945* (2022) (see page 131).

- [RPP16] Lucía Rodrigo, Pablo Pou, and Rubén Pérez. **Graphene monovacancies: Electronic and mechanical properties from large scale ab initio simulations**. *Carbon* 103 (2016), 200–208. ISSN: 0008-6223. DOI: <https://doi.org/10.1016/j.carbon.2016.02.064>. URL: <https://www.sciencedirect.com/science/article/pii/S0008622316301579> (see page 138).
- [RR14] P Rauwel and E Rauwel. **Probing the Electronic Structure of HfO 2 polymorphs via Electron Energy Loss Spectroscopy**. Tech. rep. 2014 (see pages 131, 132, 135).
- [RRA18] Michele Ruggeri, Pablo López Ríos, and Ali Alavi. **Correlation energies of the high-density spin-polarized electron gas to meV accuracy**. *Phys. Rev. B* 98 (16 Oct. 2018), 161105. DOI: [10.1103/PhysRevB.98.161105](https://doi.org/10.1103/PhysRevB.98.161105). URL: <https://link.aps.org/doi/10.1103/PhysRevB.98.161105> (see page 89).
- [Sak+95] SA Sakharov, Yu Pisarevsky, AV Medvedev, PA Senushencov, and V Lider. **Surface and volume defects in langasite crystals**. In: *Proceedings of the 1995 IEEE International Frequency Control Symposium (49th Annual Symposium)*. IEEE. 1995, 642–646 (see page 31).
- [SC03] David P Stucke and Vincent H Crespi. **Predictions of new crystalline states for assemblies of nanoparticles: perovskite analogues and 3-D arrays of self-assembled nanowires**. *Nano Letters* 3:9 (2003), 1183–1186 (see page 9).
- [SH17] Mingzi Sun and Bolong Huang. **“Energy selection channels” for high-performance electrolyte: anion-frenkel defect pair as dominant source for O ion conductions in pyrochlore-type lanthanide hafnium oxides SOFC**. *Inorganic chemistry* 56:14 (2017), 7975–7984 (see page 31).
- [Sha77] Isaiah Shavitt. “The method of configuration interaction.” In: *Methods of electronic structure theory*. Springer, 1977, 189–275 (see page 18).
- [Sil+09] V. M. Silkin, J. Zhao, F. Guinea, E. V. Chulkov, P. M. Echenique, and H. Petek. **Image potential states in graphene**. *Phys. Rev. B* 80 (12 Sept. 2009), 121408. DOI: [10.1103/PhysRevB.80.121408](https://doi.org/10.1103/PhysRevB.80.121408). URL: <https://link.aps.org/doi/10.1103/PhysRevB.80.121408> (see page 65).
- [SL20] Christopher Sutton and Sergey V. Levchenko. *First-Principles Atomistic Thermodynamics and Configurational Entropy*. Dec. 2020. DOI: [10.3389/fchem.2020.00757](https://doi.org/10.3389/fchem.2020.00757) (see page 41).
- [Smi+14] Søren Smidstrup, Andreas Pedersen, Kurt Stokbro, and Hannes Jónsson. **Improved initial guess for minimum energy path calculations**. *Journal of Chemical Physics* 140:21 (June 2014). ISSN: 00219606. DOI: [10.1063/1.4878664](https://doi.org/10.1063/1.4878664). arXiv: [1406.1512](https://arxiv.org/abs/1406.1512) (see pages 101, 110).

- [Sno20] David W Snoke. **Solid state physics: Essential concepts**. Cambridge University Press, 2020 (see page 6).
- [SSN13] LT Singh, RP Sugavaneshwar, and KK Nanda. **Carbon nanotube-ZnO nanowire hybrid architectures as multifunctional devices**. *AIP advances* 3:8 (2013), 082106 (see page 6).
- [STH08] Daniel Sheppard, Rye Terrell, and Graeme Henkelman. **Optimization methods for finding minimum energy paths**. *Journal of Chemical Physics* 128:13 (2008). ISSN: 00219606. DOI: [10.1063/1.2841941](https://doi.org/10.1063/1.2841941) (see pages 98, 99).
- [Sun+18] Yingjun Sun, Yanxia Liang, Mingchuan Luo, Fan Lv, Yingnan Qin, Lei Wang, Chuan Xu, Engang Fu, and Shaojun Guo. **Defects and interfaces on PtPb nanoplates boost fuel cell electrocatalysis**. *Small* 14:3 (2018), 1702259 (see page 31).
- [Tas79] PW Tasker. **The stability of ionic crystal surfaces**. *Journal of Physics C: Solid State Physics* 12:22 (1979), 4977 (see page 122).
- [Thi88] Walter Thiel. **Semiempirical methods: current status and perspectives**. *Tetrahedron* 44:24 (1988), 7393–7408 (see page 18).
- [Til08] Richard JD Tilley. **Defects in solids**. John Wiley & Sons, 2008 (see pages 40, 94).
- [Tra+16] Richard Tran, Zihan Xu, Balachandran Radhakrishnan, Donald Winston, Wenhao Sun, Kristin A. Persson, and Shyue Ping Ong. **Data Descriptor: Surface energies of elemental crystals**. *Scientific Data* 3 (Sept. 2016). ISSN: 20524463. DOI: [10.1038/sdata.2016.80](https://doi.org/10.1038/sdata.2016.80) (see page 124).
- [TW04] Semen A. Trygubenko and David J. Wales. **A doubly nudged elastic band method for finding transition states**. *Journal of Chemical Physics* 120:5 (Feb. 2004), 2082–2094. ISSN: 00219606. DOI: [10.1063/1.1636455](https://doi.org/10.1063/1.1636455). arXiv: [0402209](https://arxiv.org/abs/0402209) [cond-mat] (see page 98).
- [Uhr+21] Martin Uhrin, Sebastiaan P Huber, Jusong Yu, Nicola Marzari, and Giovanni Pizzi. **Workflows in AiiDA: Engineering a high-throughput, event-based engine for robust and modular computational workflows**. *Computational Materials Science* 187 (2021), 110086 (see page 10).
- [Wal+04] Andrew M Walker, Ben Slater, Julian D Gale, and Kate Wright. **Predicting the structure of screw dislocations in nanoporous materials**. *Nature materials* 3:10 (2004), 715–720 (see page 31).
- [Wat96] GD Watkins. **Intrinsic defects in II–VI semiconductors**. *Journal of crystal growth* 159:1-4 (1996), 338–344 (see page 33).

- [WN04] Chris G. Van De Walle and Jörg Neugebauer. **First-principles calculations for defects and impurities: Applications to III-nitrides**. *Journal of Applied Physics* 95 (8 Apr. 2004), 3851–3879. ISSN: 00218979. DOI: [10.1063/1.1682673](https://doi.org/10.1063/1.1682673) (see page 50).
- [Wol89] D Wolf. **Structure-energy correlation for grain boundaries in FCC metals—I. Boundaries on the (111) and (100) planes**. *Acta metallurgica* 37:7 (1989), 1983–1993 (see page 31).
- [WW69] RC Whited and WC Walker. **Exciton spectra of CaO and MgO**. *Physical Review Letters* 22:26 (1969), 1428 (see page 11).
- [Xia+95] X-D Xiang, Xiaodong Sun, Gabriel Briceno, Yulin Lou, Kai-An Wang, Hauyee Chang, William G Wallace-Freedman, Sung-Wei Chen, and Peter G Schultz. **A combinatorial approach to materials discovery**. *Science* 268:5218 (1995), 1738–1740 (see page 10).
- [Yan+16] Ji-Hui Yang, Wan-Jian Yin, Ji-Sang Park, Jie Ma, and Su-Huai Wei. **Review on first-principles study of defect properties of CdTe as a solar cell absorber**. *Semiconductor Science and Technology* 31:8 (2016), 083002 (see page 5).
- [ZHZ11] K Zou, X Hong, and Jun Zhu. **Effective mass of electrons and holes in bilayer graphene: Electron-hole asymmetry and electron-electron interaction**. *Physical Review B* 84:8 (2011), 085408 (see page 131).
- [ZJY09] Wei-De Zhang, Liao-Chuan Jiang, and Jian-Shan Ye. **Photoelectrochemical study on charge transfer properties of ZnO nanowires promoted by carbon nanotubes**. *The Journal of Physical Chemistry C* 113:36 (2009), 16247–16253 (see page 6).

List of Publications

Articles in Refereed Journals

- [1] **Siesta: Recent developments and applications.** *The Journal of Chemical Physics* 152:20 (2020), 204108. DOI: <https://doi.org/10.1063/5.0005077>. URL: <https://doi.org/10.1063/5.0005077>. Joint work with Alberto García, Nick Papior, Emilio Artacho, Volker Blum, Emanuele Bosoni, Pedro Brandimarte, Mads Brandbyge, J. I. Cerdá, Fabiano Corsetti, Ramón Cuadrado, Vladimir Dikan, Jaime Ferrer, Julian Gale, Pablo García-Fernández, V. M. García-Suárez, Sandra García, Georg Huhs, Sergio Illera, Richard Korytár, Peter Koval, Irina Lebedeva, Lin Lin, Pablo López-Tarifa, Sara G. Mayo, Stephan Mohr, Pablo Ordejón, Andrei Postnikov, Yann Pouillon, Miguel Pruneda, Roberto Robles, Daniel Sánchez-Portal, Jose M. Soler, Rafi Ullah, Victor Wen-zhe Yu, and Javier Junquera.
- [2] **Dynamic control of octahedral rotation in perovskites by defect engineering.** *Phys. Rev. B* 105 (22 June 2022), 224112. DOI: [10.1103/PhysRevB.105.224112](https://doi.org/10.1103/PhysRevB.105.224112). URL: <https://link.aps.org/doi/10.1103/PhysRevB.105.224112>. Joint work with Jiahui Jia, Xu He, Gervasi Herranz, and Miguel Pruneda.

Manuscripts in Preparation

- [1] **Addressing energetics of vacancies with localized basis sets**
Joint work with Alberto Garcia, Pablo Ordejón and Miguel Pruneda
- [2] **Rule of defects at the interface of hybrid HfO₂-Graphene nanostructures**
Joint work with Protima Rauwel, Erwan Rauwel, Pablo Ordejón and Miguel Pruneda